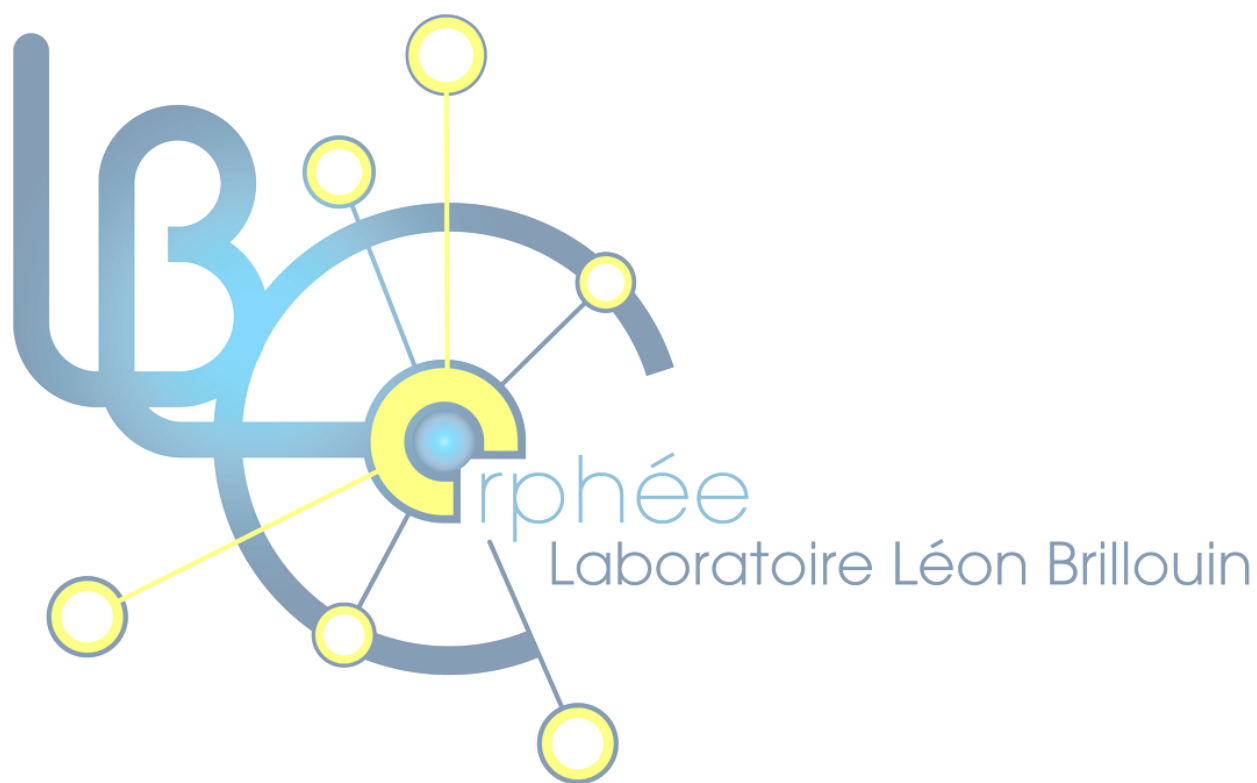


Annual Report 2011



Laboratoire Léon Brillouin
UMR 12 CEA-CNRS





**Laboratoire
Léon Brillouin**

**ANNUAL REPORT
2011**

Fan du LLB
 École de Formation à la Diffusion Neutronique

CEA SACLAY du
5 au 8 décembre 2011

Date limite pour les inscriptions :
 1^{er} octobre 2011

LLB & Orphée
 information : <http://www.llb.cea.fr/fan>
 contact : exco@llb.cea.fr

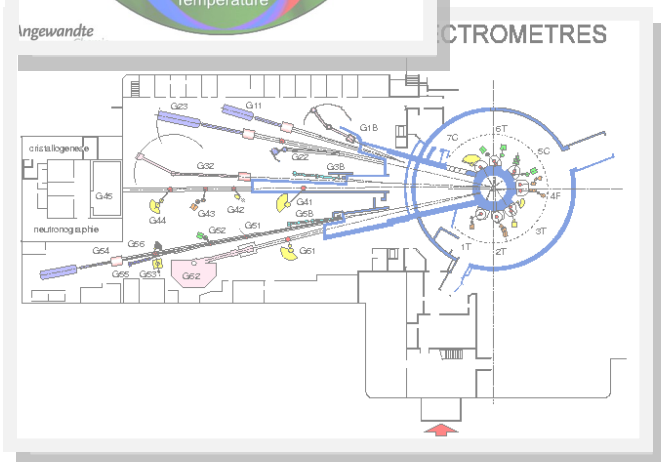
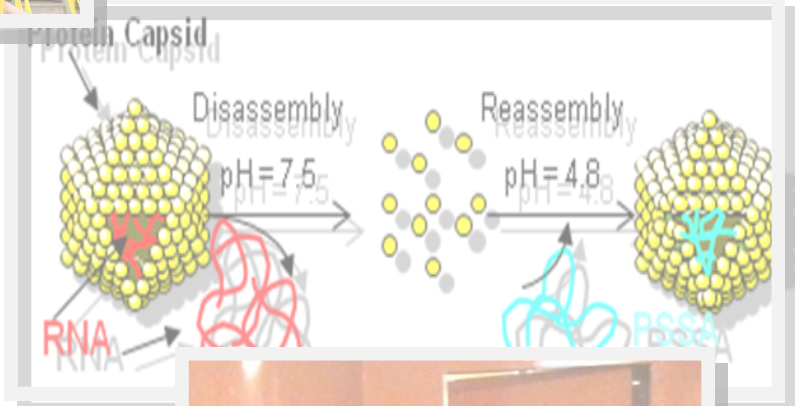
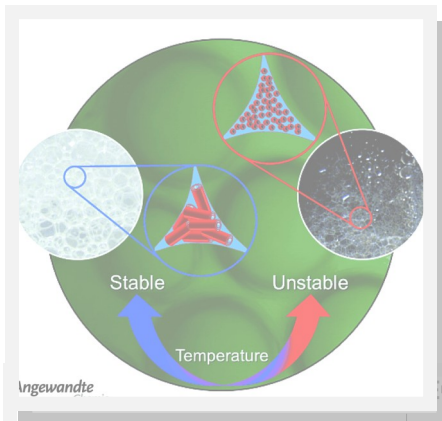
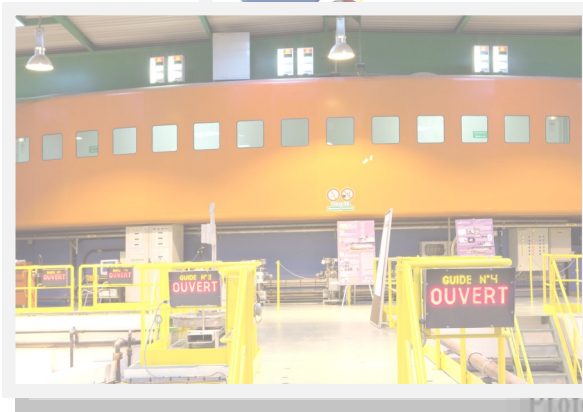



Table of contents

Foreword	p.6
Instruments	p.9
Highlights	p.15
Publications	p.56
Teaching and Education	p.65
Beamtime access	p.71

Director's words

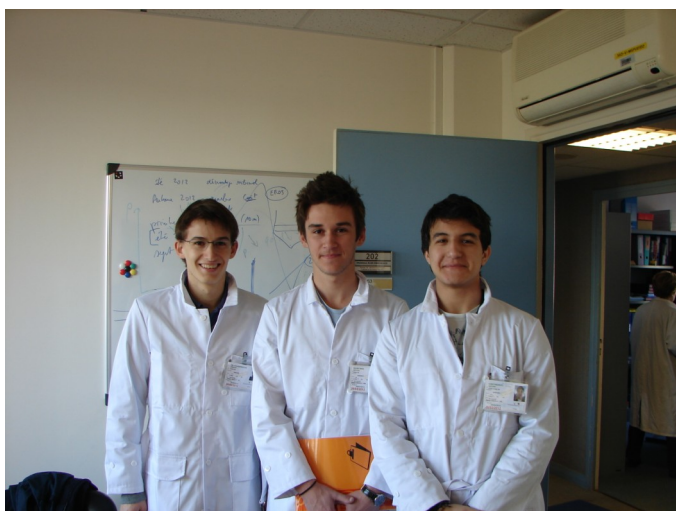


The **Laboratoire Léon Brillouin LLB**, associated to the ORPHEE reactor, is the French source of neutron scattering. It has three major missions: to conduct its own internal research, to develop and implement high performance instruments available to French and European community, and to provide training to neutron scattering and to prepare a new generation users for future sources like the ESS spallation source.

LLB's own research is based on the use of central neutron scattering and its applications to explore multidisciplinary condensed matter. It is structured along three main lines, covering most areas of current interest: - strongly correlated quantum systems and magnetism - Nanoscience and Materials: Fundamental Studies and Applications - Soft Matter and Biophysics.

Internationally, the LLB is very well integrated into the network of European sources of neutrons and muons and 2012 will see the restart of the European NMI3 contract for a period of 4 years, enabling to finance access to the installation for European users.

The highlight of 2011 was the evaluation of LLB by a committee of the Agency for the Evaluation of Research and Higher Education (AERES). This is the first such assessment by AERES because it was explicitly asked the committee to consider the whole activity of TGIR, not only the purely scientific research, but also instrumentation aspects and service and training. The visit took place on 16 and 17 May 2011 and the committee evaluated very positively the LLB.



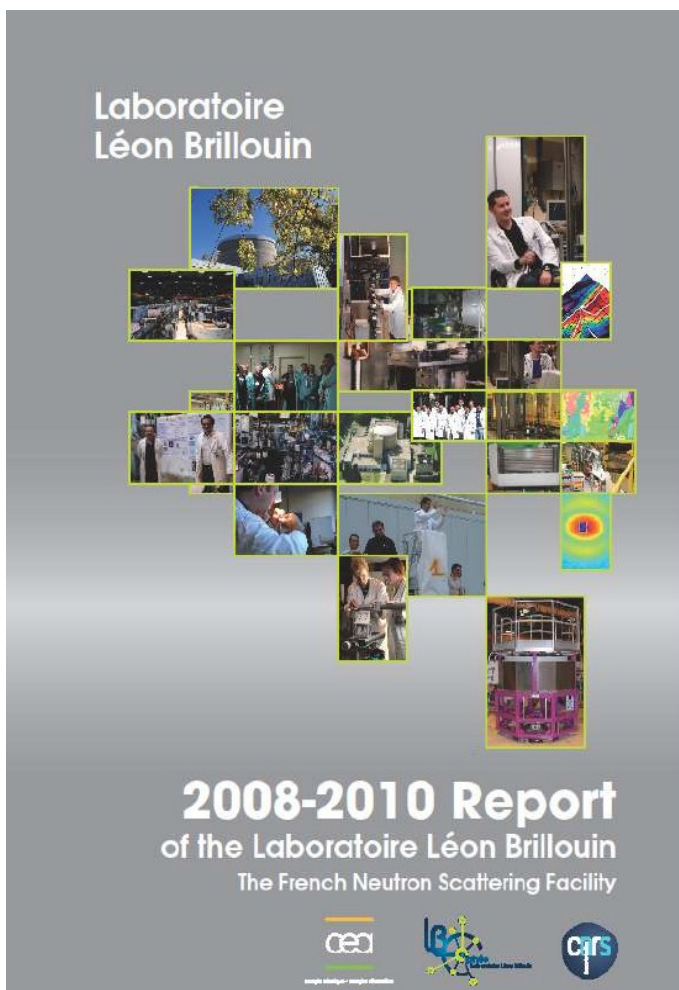
Visit from highschool students at LLB

As a national source of neutrons, it is important to maintain the instrumentation of the large scale infrastructure (LSI) at a high level of performance. The CAP2015 project of renovation of instrumental responds to this objective. This is a major program for which the LLB devotes important resources in manpower and budget.

The LLB / ORPHEE also plays a role in the existence of a "school" of French neutrons. Numerous actions are taken in this direction with operations such as training FAN of LLB or Hercules, a large number of courses in different locations, thematic schools with SFN, M2 undergraduate courses and practicals ...



Visit from A. de la Bourdonnaye (Direction générale de la recherche et de l'innovation (DGRI) from the Ministère de l'Enseignement supérieur et de la Recherche)



Le Laboratoire Léon Brillouin LLB, associé au réacteur ORPHEE, est la source française de diffusion neutronique. Il a trois missions confiées par ses tutelles, le CEA et le CNRS : mener une recherche interne propre, développer et mettre des instruments performants à disposition à la communauté française et européenne, enfin assurer la formation à la diffusion neutronique et préparer une nouvelle génération d'utilisateurs aux futures évolutions comme la source à spallation ESS.

La recherche propre du LLB s'appuie sur l'utilisation centrale de la diffusion de neutrons et de ses applications pluridisciplinaires pour explorer la matière condensée. Elle est structurée selon trois axes principaux, couvrant la plupart des domaines d'intérêts actuels : - Systèmes quantiques fortement corrélés et magnétisme, - Matériaux et Nanosciences : Études fondamentales et applications - Matière Molle et biophysique.

En tant que source nationale de neutrons, il est important de maintenir l'instrumentation de la TGIR à haut niveau de performances. Le projet CAP2015 de rénovation du parc instrumental répond à cet objectif. C'est un important programme pour lequel le LLB mobilise des ressources importantes en personnels et en budget.

Le LLB/ORPHEE joue aussi un rôle capital dans l'existence d'une « école » de neutrons française. De très nombreuses actions sont menées dans ce sens : avec des opérations de formations telles que les FAN du LLB ou Hercules, le nombre important de cours dispensés dans des sites divers, écoles thématiques comme avec la SFN, Magistère M2, accueil et encadrement de travaux pratiques ou bien les rencontres en région.

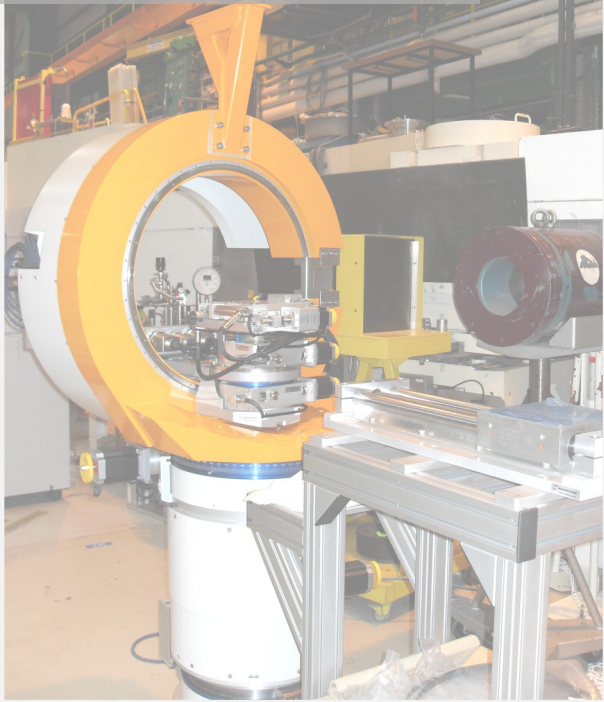
A l'échelle internationale, le LLB est très bien intégré dans le réseau des sources européennes de neutrons et de muons et 2012 va voir le redémarrage du nouveau contrat européen NMI3 pour une durée de 4 ans qui permet notamment de financer l'accès à l'installation pour des utilisateurs européens.

Le fait marquant de l'année 2011 a été l'évaluation du LLB par un comité de l'Agence d'Évaluation de la Recherche et de l'Enseignement Supérieur (AERES). Il s'agit de la première évaluation de ce type par l'AERES, car il a été explicitement demandé au comité de considérer l'ensemble de l'activité de la TGIR, non seulement l'aspect purement recherche scientifique, mais également les aspects instrumentation et service ainsi que la formation. La visite a eu lieu les 16 et 17 mai 2011 et le comité a évalué très favorablement le LLB.



The AERES committee visits our installation

“The excellent scientific output of LLB and its remarkable impact in the wider French and international user community underpins the importance of research with neutrons in addressing the “Grand Challenges” of modern society and provides an essential cornerstone for the European leadership in this field of science. However, without appropriate funding for a substantial instrument renewal and upgrade program - as proposed by the program CAP2015 - and a continuous renewal of the staff, this success story is not sustainable in the long term.”



New Spectrometers

The new 7C2 liquids and amorphous diffractometer

B. BEUNEU, J.-P. AMBROISE, B. HOMATTER



Figure 2: Pre-assembling the polyethylene protection in the guide hall

During the first months of 2012, we have installed the new detection device for 7C2, the instrument dedicated to the structure of liquids and amorphous solids. Since the determination of pair correlation functions requires a large q range, 7C2 uses a hot neutron channel of Orphée (3 short wavelengths available: 0.58, 0.7 and 1.1 Å).

The detection device consists in 16 moduli of 16 vertical Position Sensitive Detector tubes, paired at bottom, with their electronics (Fig1). The detector tubes are distant by 1.5m of the sample. Their diameter is 12.2mm (step 0.52° between two tubes) and the detection height is 470mm. The detectors are very efficient even at short wavelengths, due to their high ^3He pressure (30 bar): the average efficiency is 76% at 0.72 Å, and still 69% at 0.58 Å.

The new system keeps one of the main assets of 7C2, which is to measure the signal in one run (useful for unstable samples or environments).

To switch from the previous micro strip project to the tube solution was decided at the very end of 2007. For more than one year after we have ordered the 256 tubes (September 2008), we weren't sure that Reuter-Stokes would obtain the necessary ^3He gas. The tubes were finally delivered at the very beginning of 2010. We have selected the Mesytec electronics, which has been adapted to the electronics standards of the LLB.

The tubes were extensively tested in the guide hall, where the frame and protection were also pre-assembled (Fig2). Finally we removed he



Figure 1 : A 7C2 detection modulus

previous BF_3 banana detector after more than 20 years of excellent and loyal service, and the final assembling could take place at the beginning of 2012.

The first neutrons have been measured at the reactor start, end of March, and a number of trials and adjustments have been carried out. Although measurements are still under analysis, we can confirm the increase by a factor 25 of the counting rate (factor 4.5 for the efficiency, and 5.5 for the detection solid angle) without any loss of the signal to noise ratio (although we have not yet any collimation between the sample and detectors). The stability of the detection over one week is also at least better than with the previous detector. The counting rate of the different tubes is so similar that even before any calibration of the detector device the signal can be used (Fig3)!

The only problem is that several preamplifiers are no more

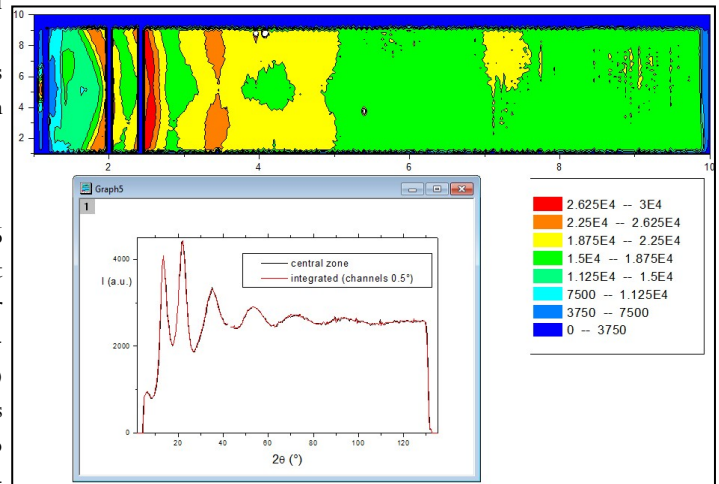


Figure 3: First sample: intensity map (blue lines for not working preamplifiers), and $I(2\theta)$ signal deduced from the map. The detection device is still not calibrated.

working, and that might be due to some of the tubes or connections. This problem has to be solved but however, because of the ring shape of the signal, the intensity for a given scattering angle is obtained from several tubes (except close to 90°). The calibration of the instrument is still in process, and 7C2 will open to users as soon as we will be able to give them all the reliable tools to reduce their data and fully use the possibilities of the new 7C2 (some first measurements on real samples have already been carried out).

The huge leap in the counting rate will open new possibilities to 7C2 users, for much smaller samples, isotopic substitution, kinetics, measurements at the shortest wavelength 0.58 Å (where the weak beam was discouraging), but also complex sample environments.

Super-6T1 : The new versatile diffractometer for Texture and Stresses analysis

M-H. MATHON, S. GAUTROT

So far, two distinct diffractometers were dedicated to the analysis of residual stresses (DIANE) and crystallographic textures (6T1) respectively. 6T1 is located on a thermal monochromatic beam and DIANE on a cold neutron beam. In both cases, the experiments suffered from lack of flexibility on the Bragg peaks accessible and improvements are needed to keep these devices competitive.

Moreover, the communities of engineers and metallurgists have shown a growing interest for the characterization of microstrain, and heterogeneities of mechanical behavior. This kind of research requires measurements coupled textures/strain (including measures in situ under load). So, as part of the rejuvenation of the 6T1 diffractometer to upgrade its capabilities, it was decided to design a versatile device that enables both measures of strains and crystallographic texture on a beam of thermal neutrons.

Thus, Super 6T1 will be a 4-circles diffractometer using thermal neutrons, optimized for characterization of texture, internal strain measurements from multiple Bragg reflections, and for analysis of line profiles, with acquisition times significantly reduced (by a factor of about 5 for textures, and up to 30 for strains).

The development of the diffractometer should be completed in several phases:

- At the beginning of 2012, the first step was to install a **new sample - detector support**. This support contains an innovative Euler cradle including x, y, z translations allowing to perform maps of internal strains and / or texture. In parallel, an original sample changer for measuring pole figures of twelve sam-

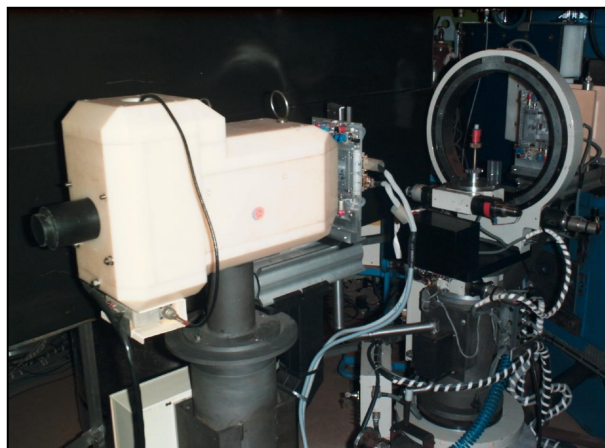


Figure 1: The old 4-circles diffractometer 6T1 dedicated only to texture measurements.

ples sequentially was developed. Concerning the sample environment, a tensile machine adaptable to the Euler cradle, and associated with an image correlation system, is also available for in situ internal strain measurements. For in situ measurements at high temperatures, a furnace is also available.

- A **new 2D detector** with a working area of 200x200 mm² and a set of four radial collimators (covering a sufficiently wide resolution range) will be available before the end of 2012.
- This diffractometer should have **several wavelengths** and it constitutes the next important step of this project scheduled for 2013. The protection of the output beam will be modified to have access to 3 different take-off angles. So, with two focusing monochromators (Cu (111) and PG(002)), the diffractometer will dispose of 6 possible wavelengths.
- By the end of 2012, the LLB will have thus already a very competitive new instrument for the study of materials in the field of mechanics and metallurgy.
- By the end of 2013, the variable wavelength will give access to measurement geometry close to $2\theta = 90^\circ$ and residual stress mapping may be carried out on industrial parts of reasonable size (25 kg maximum).

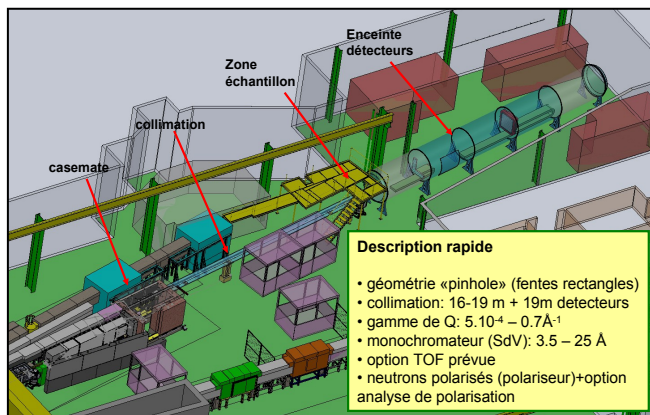


Figure 2: Sample-detector support with a new Euler Cradle including x,y,z translations.

PA20: A new SANS + GISANS project for soft matter, materials & magnetism

G. CHABOUSSANT, S. DÉSSERT, P. LAVIE & A. BRÛLET

PA20 will replace PAXE at the end of 2013 with several major upgrades and brand new functionalities: the total length of PA20 will be 40 m, including a 19 m collimation length, a 20 m detector tank containing high-resolution/high-efficiency XY detectors. The casemate will contain a monochromator (velocity selector $\lambda=0.3-2.0$ nm), a chopper system for Time-of-Flight (TOF) mode, a polarizer and a RF spin flipper. The detector system will consist in one rear detector at "small angles" and two panels of front detectors for "high angles". PA20 will improve SANS experiments in a variety of ways in terms of neutron flux, scattering angle coverage, Q-resolution and neutron polarization.



PA20 general layout along the G5 guide

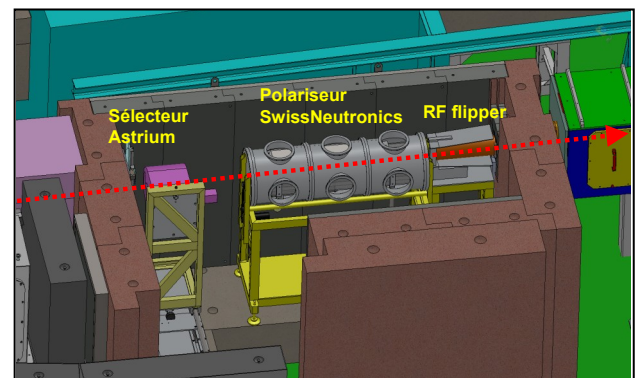
PA20 will allow faster measurements, with "single-shot" access to a wider range of scattering vectors (from very small scattering vectors, lower than 0.01 nm^{-1} (at $\lambda=0.8$ nm and 19 m) up to 7 nm^{-1} (at $\lambda=0.4$ nm and 1.0 m)). Faster data acquisition rates enables kinetics measurements or systematic studies as a function of temperature near phase transitions where better resolution are critical to differentiate between models or theories. Also, the increased Q-range coverage allowed by the 2D front and rear detectors will permit a more rigorous analysis of interface effects, their fractal aspects (Porod regime) compared to volume effects (Guinier regime). Pushing the limits in terms of flux and resolution is also critical when dealing with samples that are difficult to synthesize or which can be obtained only in modest quantity. The new instrument PA20 will make it possible to tackle such studies. Regarding magnetic studies, PA20 will be the first SANS/GISANS with multi-wavelength neutron polarization at LLB, fulfilling the needs to study magnetization processes in nano-objects and thin films. The GISANS setup will be particularly useful to study nanostructured surfaces and interfaces (deposited or embedded nano-objects), magnetic do-

main formation, multilayered materials or magnetic thin films through specular and off-specular signals. In parallel, SANS with polarized neutron from $\lambda=0.4$ nm upwards will increase the possibilities to studies strongly correlated electrons systems, complex magnetic configurations (long-range periodicity, frustrated), photo-magnetic molecular systems, and composite magnetic materials. The key components forming PA20, whose general layout is shown in Fig.1, are the casemate, the collimation line and the detectors tank.

The casemate is 3 m long and composed of lead and heavy concrete. It will house a Dornier-type velocity selector that can be replaced by a chopper when PA20 is operating in Time of Flight (TOF) mode, an escapable polarizer placed in vacuum, and a RF spin flipper.

The collimation line offers maximum flexibility in terms of beam shapes and accuracy. The maximum collimation length, in polarized mode, will be 16 m and 19 m in non-polarized mode. This system of independent slits, with horizontal and vertical adjustments, has been chosen to provide square shaped collimation for SANS and vertical or horizontal rectangular shape for GISANS.

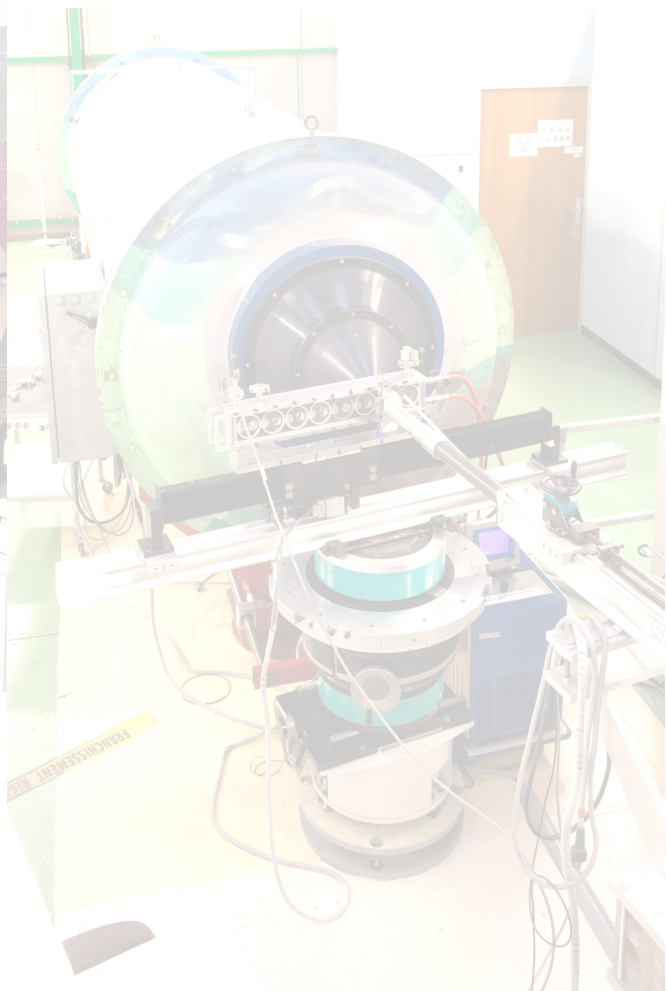
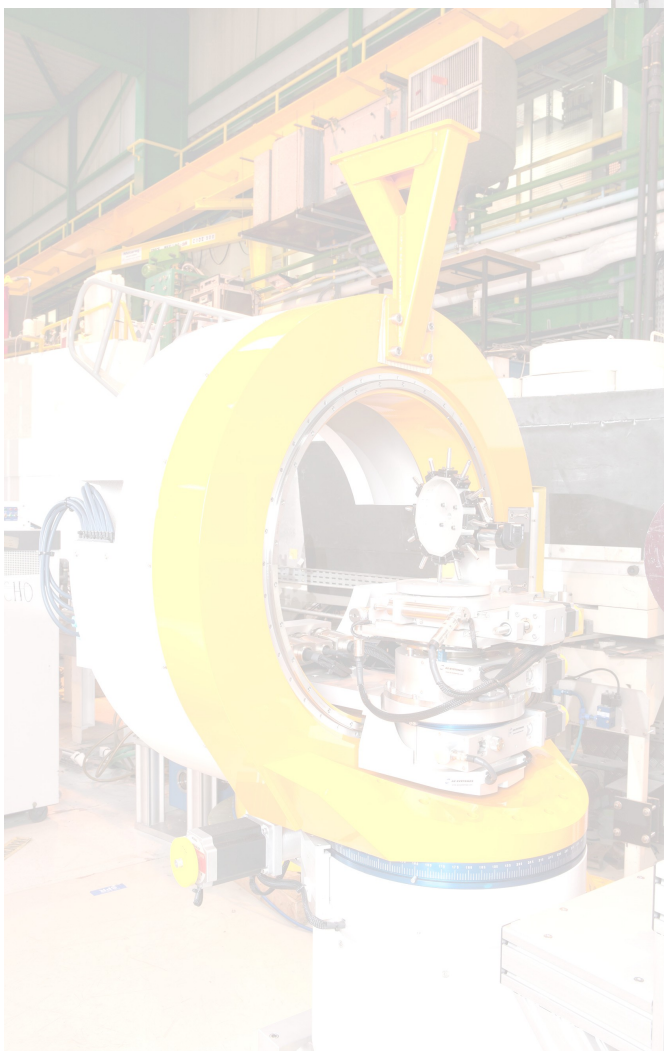
Two sets of 2D XY ^3He detectors will be placed inside the detector tank to achieve high angular resolution and large angular coverage. The rear detector is a $64 \times 64 \text{ cm}^2$ ^3He single-bloc Aluminium multi-tube ILL-made detector with 5 mm vertical and horizontal pixel size. The front detectors, also with ^3He , consist of two sets of 12 mm tubes placed perpendicular one to another. Each set will be 20 cm wide and 64 cm high. The front detector will allow covering an extended Q-range and its distance to sample will be adapted according to the position of the rear detector.



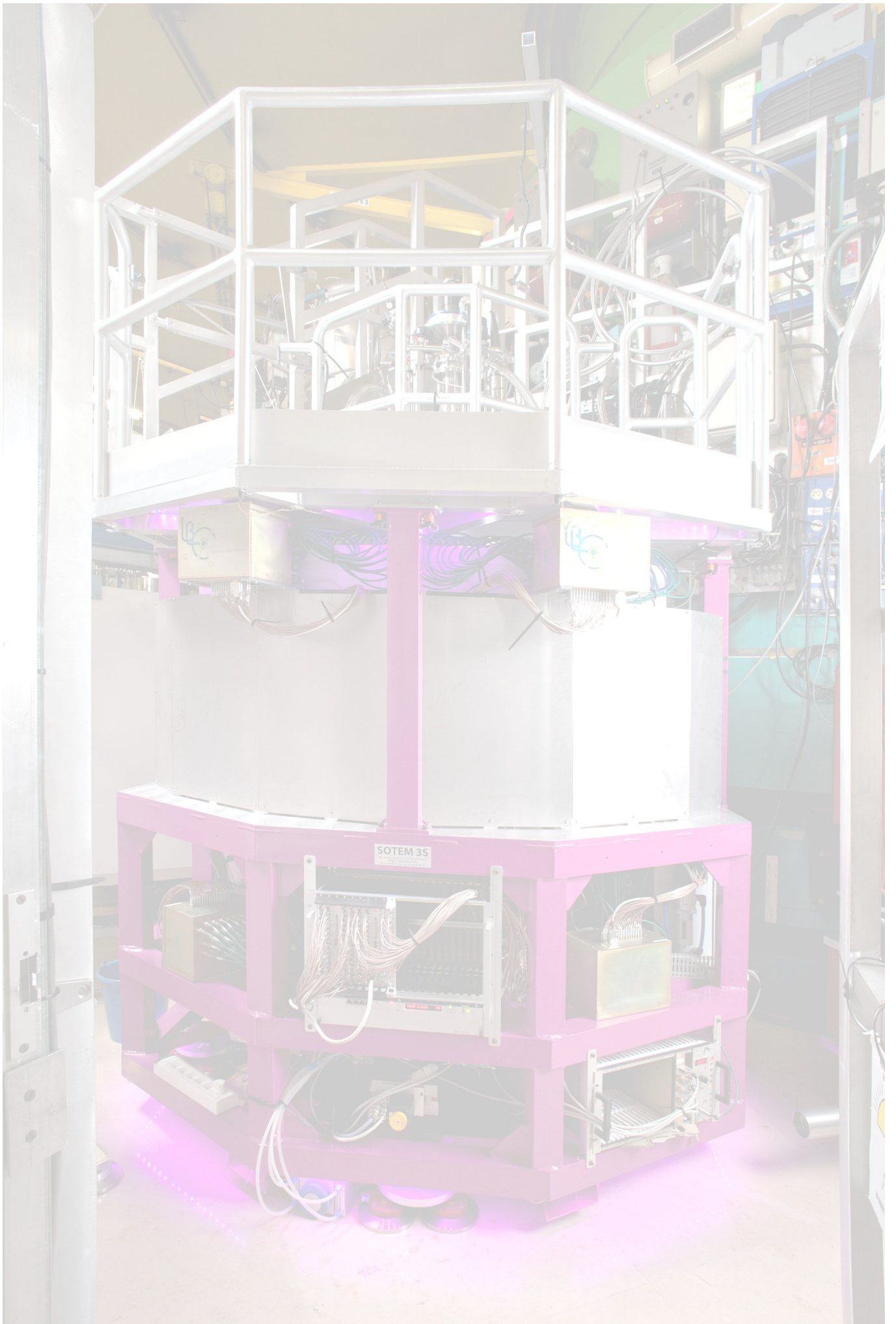
Casemate details
(to be installed in summer 2012)

References

1. G. Chaboussant et al (2012) *J. Phys.: Conf. Ser.* 340 012002



Highlights



AXE 1:

STRONGLY CORRELATED QUANTUM MATERIALS AND MAGNETISM.

The “strongly correlated electron systems” denote a class of materials and physical phenomena which cannot be described in terms of the standard theory for a Fermi gas of non-interacting electrons. Such situations mainly occur in compounds containing transition-metal or rare-earth elements, because *d* and *f* orbitals have a more pronounced localized character. One common feature in many of these materials is the coexistence of several degrees of freedom associated with the electron- (charge, spin, orbital) or lattice sub-systems, whose interplay is responsible for a large variety of ground states and excitation spectra. Well-known examples studied at LLB, both experimentally and theoretically, include cuprate or ferropnictide high- T_c superconductors, “giant magneto-resistance” manganites, compounds with short-range magnetic interactions subject to geometrical frustration (multiferroics, spin-ices, etc.), lanthanide-based heavy-fermion systems and “Kondo insulators”, as well as a number of materials in which unconventional orders occurs, such as the “magnetic blue phase” of MnSi, or the multipole-order states found in rare-earth hexaborides. Because neutrons interact with both the atom nuclei and their electron shells, neutron scattering is one of the best tools to study this type of physics involving interplay of lattice and magnetic properties. Polarized neutron beams, implemented on several spectrometers at LLB, further enhance the potential of neutron experiments for studying strong correlation phenomena in condensed matter.

- 1) SINGLE CRYSTAL INVESTIGATION OF THE *KAGOMÉ* ANTIFERROMAGNET $U_3Ru_4Al_{12}$.
R. Troc, M. Pasturel, O. Tougait, A. P. Sazonov, A. Goukassov, C. Sulkowski, & H. Noël
- 2) MAGNETIC EXCITATIONS IN LAYERED RUTHENATES.
P. Steffens, O. Friedt, Y. Sidis, P. Link, J. Kulda, K. Schmalzl, S. Nakatsuji, & M. Braden
- 3) MIXED ACOUSTIC PHONONS AND PHASE MODES IN AN APERIODIC COMPOSITE CRYSTAL.
B. Toudic, R. Lefort, C. Ecolivet, L. Guérin, R. Currat, P. Bourges, T. Brezczewski
- 4) NEUTRON AND CHIRALITY: EXPERIMENTS AND SIMULATION.
V. Simonet, M. Loire, S. Petit, R. Ballou
- 5) STRUCTURE AND MAGNETIC PROPERTIES OF In_2RuMnO_6 AND In_2RuFeO_6 : HEAVILY TRANSITION-METAL DOPED In_2O_3 -TYPE BIXBYTES.
C. de la Calle, M. J. Martínez-Lope, V. Pomjakushin, F. Porcher, J.A. Alonso

Single crystal investigation of the *Kagomé* antiferromagnet $U_3Ru_4Al_{12}$

R. TROC^A, M. PASTUREL^B, O. TOUGAIT^B, A. P. SAZONOV^C, A. GOUKASSOV^C, C. SUKOWSKI^A & H. NOËL^B

A Institute of Low Temperature and Structure Research, Polish Academy of Sciences, Wrocław, Poland

B Institut des Sciences Chimiques de Rennes, Chimie du Solide et Matériaux, Rennes, France

C Laboratoire Léon Brillouin, CEA-CNRS, CEA Saclay, 91191 Gif-sur-Yvette, France

r.troc@int.pan.wroc.pl

Single crystal neutron diffraction was used to determine the magnetic structure of a novel Kagomé antiferromagnet ($T_N = 9.5(5)$ K), $U_3Ru_4Al_{12}$. An original arrangement of the magnetic moments, lying in the 2D Kagomé network of uranium atoms has been evidenced, resulting in a net moment in each $[U_3]$ triangle, leading to a ferromagnetic-like component in each U-layer, nearest neighbouring layers being coupled antiferromagnetically. Anisotropic electrical transport measured at high temperature highlights the presence of Kondo-like interactions and those below T_N the opening of a gap in the Fermi surface.

The ternary uranium based aluminides $U_3T_4Al_{12}$ ($T = Fe, Co, Ru$) crystallize in the hexagonal $Gd_3Ru_4Al_{12}$ structure-type (space-group $P6_3/mmc$, no. 194), in which the magnetic uranium atoms are forming a 2D distorted *Kagomé* network parallel to the (*a*, *b*) plane. This geometry is usually favourable for magnetic moment frustration and was thought to be responsible of the spin-glass behaviour of the iron and cobalt based compounds^{1,2}. Surprisingly, a polycrystalline sample of $U_3Ru_4Al_{12}$ was found to order antiferromagnetically at $T_N = 8.4(5)$ K and electrical transport properties are dominated by Kondo-like interactions³.

means of magnetic, electrical, magnetoelectrical, thermopower and specific heat measurements, as well as by neutron diffraction at low temperature⁴.

The thermal variation of the magnetic susceptibility (Fig. 1), measured along *a*- and *c*-axis, shows a high anisotropy between both crystallographic directions. Along the *a*-axis, a pronounced maximum is observed at $T_N = 9.5(5)$ K, in agreement with the expected antiferromagnetic ordering, while along the *c*-axis, only a shallow hump is observed at 6(1) K. The average value $2/3 c_a + 1/3 c_c$ nicely fits the value for the polycrystalline sample. From the previous observations, one can expect the ordering of the moments in the (*a*, *b*) plane. In order to check this assumption, unpolarized neutron diffraction studies were performed at $T = 1.6$ K and 10 K on the 6T2 diffractometer ($\lambda = 0.9$ Å) at the Orphée reactor of the Laboratoire Léon Brillouin. As many as 136 Bragg reflections were collected up to $\sin\theta/\lambda = 0.45$ Å⁻¹ at 1.6 K. The nuclear structure parameters were deduced from the measurements at 10 K, corroborating these obtained at room temperature by single crystal XRD.

The refinement of the magnetic structure indicates relatively large U^{3+} magnetic moments of 2.5(2) μ_B , lying in the (*a*, *b*) plane, as expected (Fig. 2). They are parallel either to the *a*-axis or the *b*-axis as well as to the shortest diagonal of the rhombus formed by those axes. The three uranium moments are forming an angle $\alpha = 2\pi/3 = 120^\circ$ at the three apexes of the smallest $[U_3]$ triangles of the *kagomé* network. The interatomic distances in this triangle are $d_{U-U} = 3.575(1)$ Å, the value not far from the 3.5 Å Hill criterion for appearance of a magnetic ordering. This and the other d_{U-U} distances are visualized in Fig. 2. It should be noted that the classical

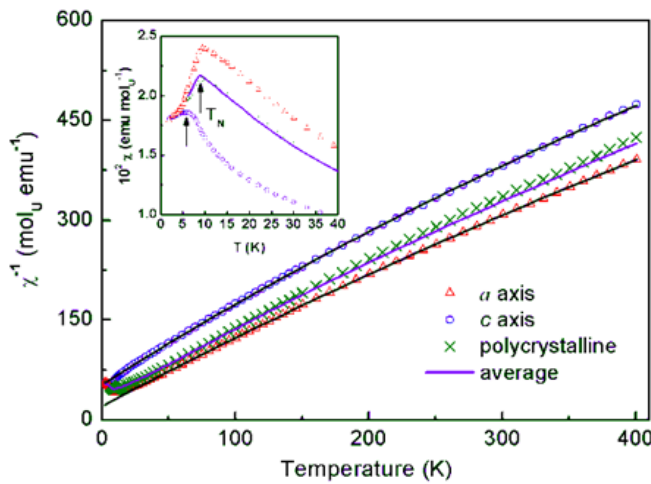


Figure 1 : Temperature dependencies of the reverse molar susceptibility measured under a magnetic field of 0.5 T applied parallel to the *a*- and *c*-axes. Solid lines represent fits to the modified Curie Weiss law of the experimental data above about 20 K. Such dependencies for average susceptibility and for

In order to further investigate this intermetallic, a single crystal has been grown by the Czochralski tetra-arc pulling method and carefully examined by

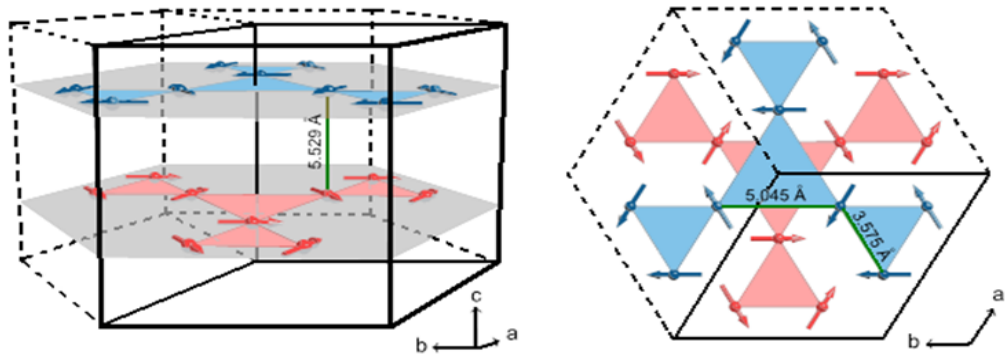


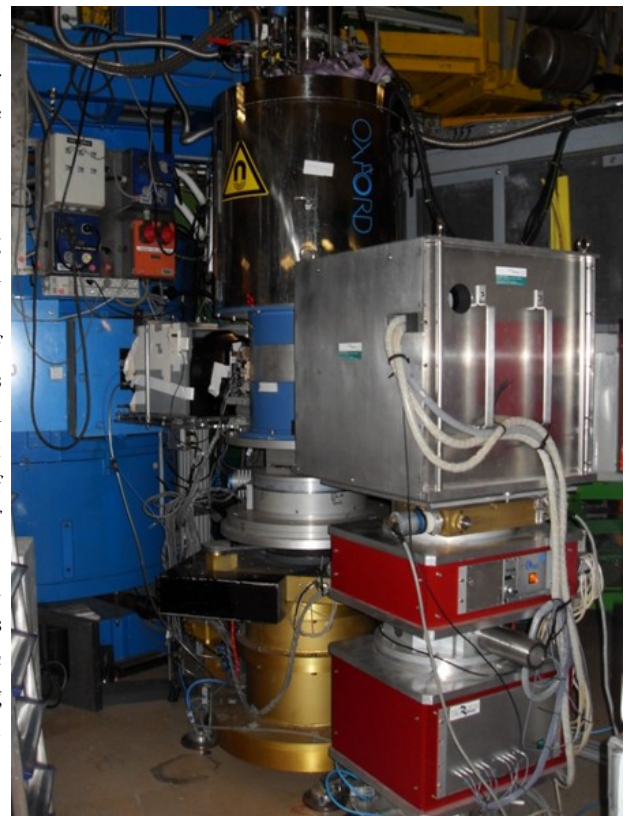
Figure 2 : Magnetic structure (left panel) of $U_3Ru_4Al_{12}$, and its projection on the basal (a , b) plane (right panel). For clarity, only the uranium atoms are presented.

ground state of a *kagomé* lattice antiferromagnet is an ordered state where the three spins around any triangle are oriented 120° apart, such that the sum of these three spins shows no net moment on the triangle. Surprisingly, the magnetic structure for $U_3Ru_4Al_{12}$ features a net moment on each triangle, where the spins are rotated -60° , 0° , and $+60^\circ$ from the b -axis. Thus $2/3$ of all nearest-neighbor bonds are slightly ferromagnetic while $1/3$ is antiferromagnetic leading to a ferromagnetic-like component in the layer. The nearest-neighbor layers are coupled in such a way that their ferromagnetic-like components compensate each other, which results in an overall antiferromagnetic structure.

Electrical resistivity measurements also evidence a strong anisotropy between a - and c -axes. At high temperature, both of them show some logarithmic increase domains with decreasing temperature, in agreement with the presence of Kondo fluctuations. A rapid decrease of $r(T)$ below T_N is observed along the c -axis, as expected from the decrease in the spin disorder resistivity, while a sharp peak develops at this temperature along the a -axis, highlighting the opening of a gap in the Fermi surface. The observed thermal variation of these resistivities, as well as these of the transverse magnetoresistivity, Seebeck coefficient and specific heat (giving a Sommerfeld coefficient $g = 200 \text{ mJ K}^{-2} \text{ mol}_U^{-1}$) compares well with those reported previously for the antiferromagnetic moderate heavy fermion UCu_5In_5 or Cr_6 , where the gapping of the Fermi surface is attributed to the formation of a spin density wave.

Further experimental work should be performed to ascertain this hypothesis, as well as further neutron diffraction experiments under magnetic field in order to identify the metamag-

netic transition observed on the $M=f(B)$ curve at 2 K above $B = 1 \text{ T}$.



The thermal neutron diffractometer 6T2

References

1. A.P. Gonçalves et al., *Intermetallics*, 17, 25
2. O. Tougaard et al., *J. Solid State Chem.*, 177, 2053
3. M. Pasturel et al., *J. Phys.:Cond. Matter*, 21, 125401
4. R. Troć et al., *Phys. Rev. B*, in press
5. D. Kaczorowski et al., *Phys. Rev. B*, 63, 144401
6. A. S. Barker Jr. et al. *Phys. Rev. Lett.*, 20, 384

Magnetic excitations in layered Ruthenates

P. STEFFENS^{AB}, O. FRIEDT^A, Y. SIDIS^C, P. LINK^D, J. KULDA^B, K. SCHMALZL^E, S. NAKATSUJI^F, & M. BRADEN^A

A II. Physikalisches Institut,
Univ. Köln, Germany

B Institut Laue-Langevin, Gre-
noble, France

C Laboratoire Léon Brillouin,
CEA-CNRS, CEA Saclay,
91191 Gif-sur-Yvette, France

D FRM2, Garching, Germany

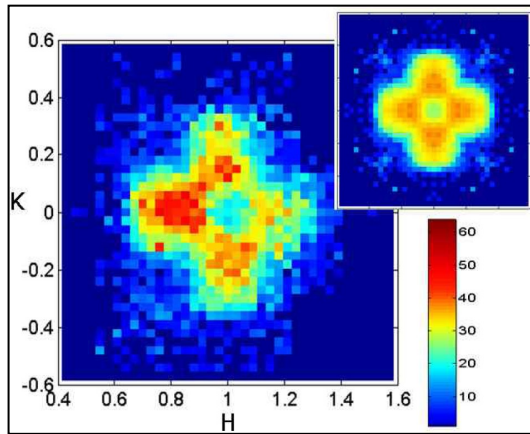
E Jülich Centre for Neutron
Science, Germany

F Institute for Solid State Phys-
ics, University of Tokyo, Japan

steffens@ill.fr

In a comprehensive study on various triple-axis spectrometers, we have analyzed the magnetic excitations of the layered Ruthenates $\text{Ca}_{2-x}\text{Sr}_x\text{RuO}_4$. In the concentration close to the metal-insulator transition but still on the paramagnetic and metallic side, these materials show magnetic correlations which indicate a competi-

tion of different magnetic instabilities. An applied magnetic field sensitively changes the correlations and gives rise to a metamagnetic transition above which a ferromagnetic state with its characteristic excitations is induced.



The family of layered ruthenates has been in the focus of interest since the discovery of superconductivity in Sr_2RuO_4 , which is an unconventional superconductor with electrons most likely pairing into triplets.

The series $\text{Ca}_{2-x}\text{Sr}_x\text{RuO}_4$, which arises from Sr_2RuO_4 by substitution of Strontium by Calcium, exhibit a variety of exciting phenomena. Although the replacement of Sr by Ca does not change the number of charge carriers, the electronic and magnetic behaviour is closely coupled to slight structural changes and varies considerably as a function of the Sr content x . In the concentration range of $0.2 < x < 0.5$, samples exhibit a metamagnetic transition from a state with low susceptibility, reminiscent of antiferromagnetic correlations, to a state with high magnetic polarization. A similar transition has been observed in the closely related material $\text{Sr}_3\text{Ru}_2\text{O}_7$, where exciting phenomena related to the quantum-critical end point of the metamagnetic transition were reported.

Although there is no static magnetic order, magnetic correlations are likely to determine the physics of phenomena like the metamagnetic transition or spin-triplet superconductivity (which is supposed to be

related to ferromagnetic fluctuations). By the possibility to vary the parameters Sr-concentration, temperature and magnetic field, we can systematically probe the magnetic correlations by inelastic neutron scattering. Among the instruments used for these studies are the triple axis spectrometers of the LLB: 1T, 2T, 4F1 and 4F2

The ruthenates studied here have a layered structure, analogous to the cuprate High-Tc superconductors, which is formed by planes of ruthenium and oxygen ions. These planes determine the electronic properties, and also the magnetic correlations are highly two-dimensional.

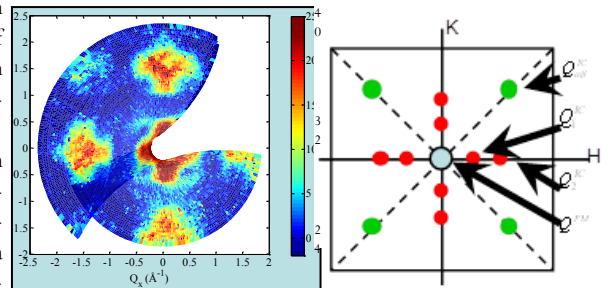


Figure 1 : Magnetic inelastic scattering over several Brillouin zones (left) and sketch of the positions of the different contributions in one zone (right).

As there is no static order, the entire magnetic scattering is inelastic. The intensity map in Fig. 1 (and in the title) show the inelastic magnetic scattering ($\Delta E = 4 \text{ meV}$ and 2.5 meV , respectively) over several (2D) Brillouin zones in $\text{Ca}_{1.8}\text{Sr}_{0.2}\text{RuO}_4$ at $T = 2 \text{ K}$. While scattering is concentrated near the zone centre (which would correspond to ferromagnetic correlations) there is no maximum just at the zone centre, but at positions separated by a small finite vector along the axes. This means the scattering is antiferro-

magnetic in nature, with an incommensurate propagation vector. A more detailed analysis reveals that there are contributions from at least two Q-vectors near each other, which cannot be separated in the intensity maps. The sketch in the right part of Fig. 1 shows the Q-vectors from which these contributions arise. Those from the incommensurate positions Q_{ic1} and Q_{ic2} give the strongest intensity in the map, but also the one on the diagonal, $Q=(0.3,0.3,0)$, is present, see the detail in Fig. 2a. These particular Q-vectors result from the electronic band structure of the material and correspond to excitations of electrons from one to another place on the Fermi surface. This itinerant mechanism determines magnetic excitations also in other classes of materials, for example some iron arsenide superconductors, and it is decisive for many of the physical properties .

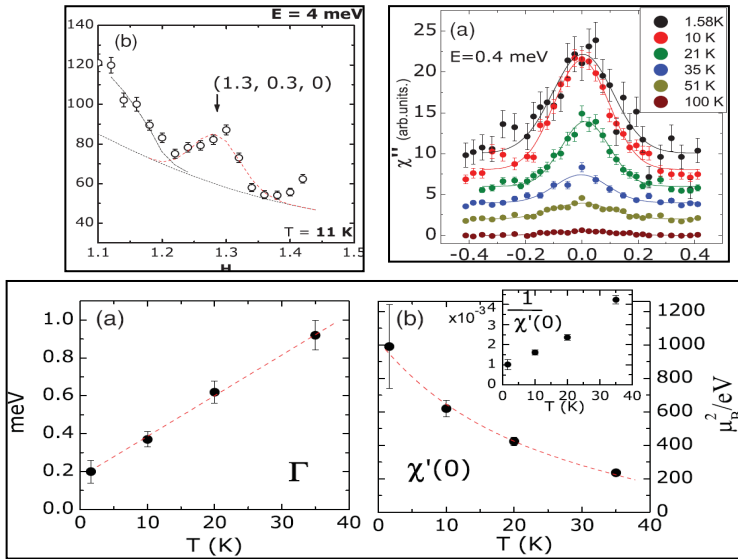


Figure 2 : Magnetic scattering in $Ca_{1.38}Sr_{0.62}RuO_4$. (a) Contribution from the diagonal nesting vector. (b-d) Ferromagnetic component and its characteristic parameters.

At low temperature, ferromagnetic correlations are entirely suppressed in the sample with $x=0.2$. However, they are very strong when slightly increasing the temperature and/or the Sr concentration, as can be seen in Fig. 2b for a scan across the zone centre for different temperatures at low energy transfer. The analysis of the ferromagnetic scattering in part (c) and (d) of the same figure shows how the characteristic energy Γ of the fluctuations decreases, and how the real part of the magnetic susceptibility diverges when lowering

the temperature. Both effects represent the typical behaviour when approaching the transition into a ferromagnetic state.

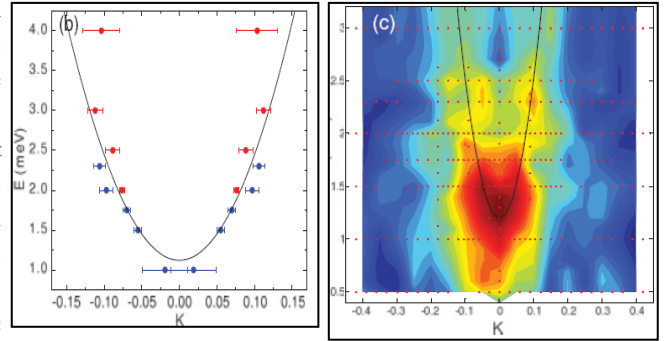


Figure 3 : Magnetic scattering above the metamagnetic transition (at $B = 10T$) in $Ca_{1.8}Sr_{0.2}RuO_4$. (left) Dispersion and (right) intensity map of the induced excitation.

After comprehensive measurements on different samples in different conditions, we arrive thus at a generalized picture. Magnetic correlations in layered ruthenates are characterised by competition of ferro- and antiferromagnetic instabilities with the balance depending sensitively on temperature and Strontium concentration.

This balance can also be influenced by the application of a magnetic field. Contrary to the simple case where an external field acts only to polarize magnetic moments in the sample, our inelastic neutron scattering results prove that the intrinsic correlations change fundamentally: while being antiferromagnetic in character in $Ca_{1.8}Sr_{0.2}RuO_4$ (without field at low temperature), a dispersive excitation resembling a magnon in a ferromagnet appears under field (Fig. 3), whereas the antiferromagnetic features are suppressed.

In summary, inelastic neutron-scattering reveals the delicate balance of different magnetic instabilities driving the physical properties and the metamagnetic transition in layered ruthenates.

References

1. P. Steffens, O. Friedt, Y. Sidis, P. Link, J. Kulda, K. Schmalzl, S. Nakatsuji, and M. Braden, *Phys. Rev. B* **83**, 054429 (2011);
2. P. Steffens, Y. Sidis, P. Link, K. Schmalzl, S. Nakatsuji, Y. Maeno, and M. Braden, *Phys. Rev. Lett.* **99**, 217402 (2007);
3. O. Friedt, P. Steffens, M. Braden, Y. Sidis, S. Nakatsuji, and Y. Maeno, *Phys. Rev. Lett.* **93**, 147404 (2004); and references therein.

Mixed acoustic phonons and phase modes in an aperiodic composite crystal

B. TOUDIC^A, R. LEFORT^A, C. ECOLIVET^A, L. GUÉRIN^A, R. CURRAT^B, P. BOURGES^C & T. BREZIEWSKI^D

A Institut de Physique de Rennes, UMR UR1-CNRS 6251, Université de Rennes 1, 35042 Rennes, France

B Institut Laue-Langevin, Grenoble, France

C Laboratoire Léon Brillouin, CEA-CNRS, CEA Saclay, 91191 Gif-sur-Yvette, France

D Facultad de Ciencias, Universidad del País Vasco, Bilbao, Spain

bertrand.toudic@univ-rennes1.fr

Aperiodic crystals which are long range ordered materials present original dynamics features due to the lack of translational symmetry formally implying the nonvalidity of the Brillouin zone concept. We report the observation by neutron

scattering of an overdamped acoustic-like mode at a Bragg peak position in a n-alkane-urea inclusion crystal. This result implies the existence of a gap in the dispersion branch.

Aperiodic crystals may show low lying excitations resulting from the infinite degeneracy of their ground state related to the possibility of describing these structures in a higher dimensional space [1, 2]. Among the various types of incommensurate systems, one of the simplest is illustrated by uniaxial composite crystals. There, contrary to displacively modulated crystals, no mean Brillouin zone can be defined and consequently, no perturbative approaches can be used to approximate phonon branches.

infinite wavelengths, each one corresponding to a rigid displacement of one sub-lattice with respect to its fixed counterpart. Two sound velocities for host and guest sub-lattices could then be defined. In real materials, interaction between sublattices couples the sublattice acoustic modes to give rise to two new modes at infinite wavelengths, an actual unique acoustic mode for the composite V_+ and a mode corresponding to the relative anti-translation (sliding mode) of both sublattices V_- .

n-alkane/urea crystals are incommensurate along the channels direction labeled the c axis (Fig. 1). A misfit parameter is defined by the ratio of the host and guest periodicities $\gamma = c_h/c_g$, respectively determined by the pitch of the urea helices and the guest repeat distance. The room temperature superspace group is of rank 4, $P6_122(00\gamma)$ with the vectors Q_{hklm} :

Coherent neutron scattering experiments [4], partly done on the LLB cold neutron triple-axis 4F1, were performed using a single crystal of fully deuterated nonadecane/urea, in its high symmetry phase in order to avoid the complexity of the different higher dimensional ordered phases below $T_{c1} = 150K$ [3]. Phonon excitations were measured at $T = 160K$, i.e. in the high symmetry phase $P6_122(00\gamma)$, and near the Bragg position Q_{1040} . Around that wavevector, $Q = Q_{1040} + q \cdot c_{host}^*$, a simultaneous measurement of the LA and the TA modes propagating along the aperiodic direction is allowed. Inelastic phonon LA and TA modes were fitted with normalized damped oscillator functions convoluted with the spectrometer resolution [4].

The obtained dispersion curves for the LA and TA branches are presented in Fig. 2(a). Usual behavior is obtained for the doubly degenerated TA propagating along the incommensurate direction both considering the damping which follows the hydrodynamics law in q^2 and the energy dispersion. The striking result is the evidence of a totally new behavior for the longitudinal “acoustic-like” excitation. Indeed, on the Bragg peak location it generates a well-resolved quasielastic scattering in the spectrum [4]. This implies a gap in the dispersion of this LA branch since for a damped oscillator of intrinsic frequency ω_0 and width Γ_0 the quasielastic width tends towards ω_0^2/Γ_0 when approaching the overdamped regime. This gap is found equal to 80 GHz at the Bragg peak position. The damping of this branch also presents a

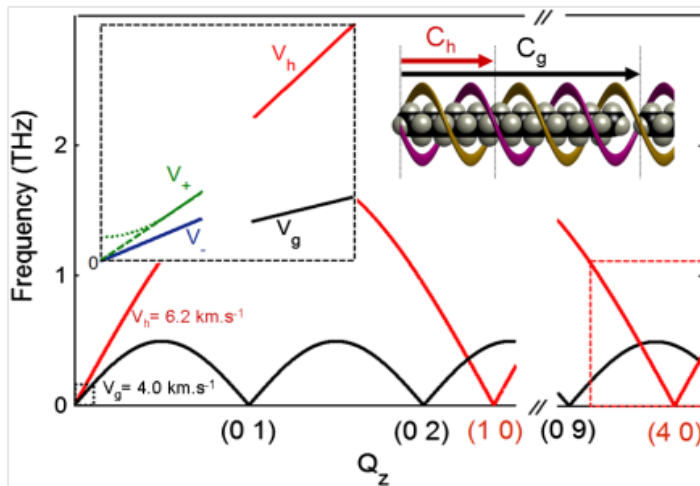


Figure 1 : Predicted dispersion curves of the longitudinal acoustic phonons propagating along the aperiodic direction Q_z of the n-nonadecane-urea. (insert : zoom of the small Q_z range)

$$Q_{hklm} = ha^* + kb^* + lc_{host}^* + mc_{guest}^*$$

If the interaction between the sub-lattices could be neglected, one would get two zero energy modes at

very unusual behavior since it does not go to zero at low q values, violating the hydrodynamics rules in q^2 expected for infinite wavelength. Its value at 160 K is almost constant around 180 GHz, in total disagreement with the expected dependence shown by the dotted line in Fig. 2(b). Moreover, the room temperature damping is 330 GHz, indicating rather linear temperature dependence. The observed gap could be the consequence of a strong interaction between both sublattices when the intermodulation function becomes nonanalytic. In *n*-alkane/urea compounds, this strong interaction is indeed observed with depinning and lock-in phenomena and could account both for the reported observations close to $Q = Q_{1040}$ and to $Q_z = 0$ (reciprocal space center).

Similar observations to the ones done in this study were never performed before in any type of aperiodic crystals, although all these materials enter the superspace crystallographic description. In quasicrystals, it has been shown that strong Bragg peaks can act as the pseudo-Brillouin zone center and in inorganic aperiodic composites, different longitudinal acoustic modes at various sublattice Bragg reflections were observed, with a normal behavior for the dispersion and the damping. Theoretical modelizations including actual interaction energy terms are necessary to go further on in order to describe the complex observation in the acoustic phonon spectrum beyond the hydrodynamics limit.

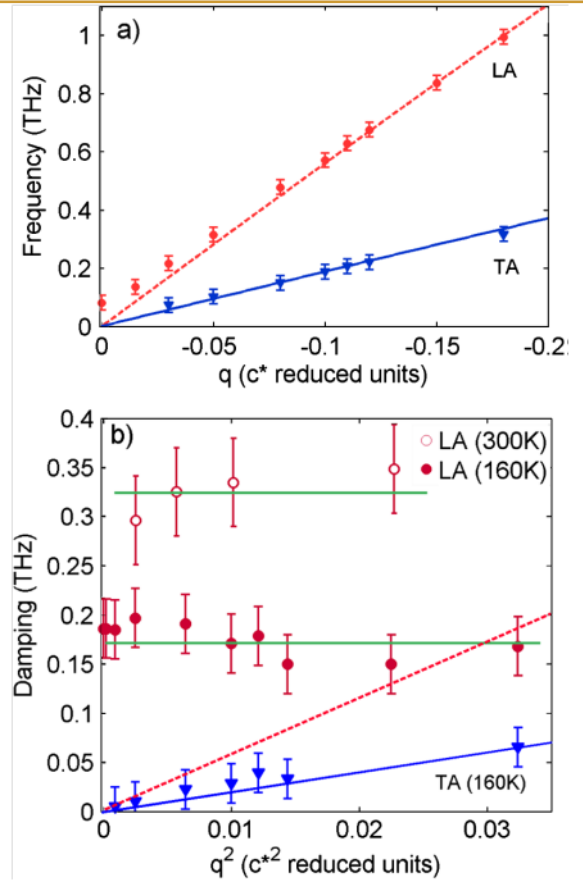
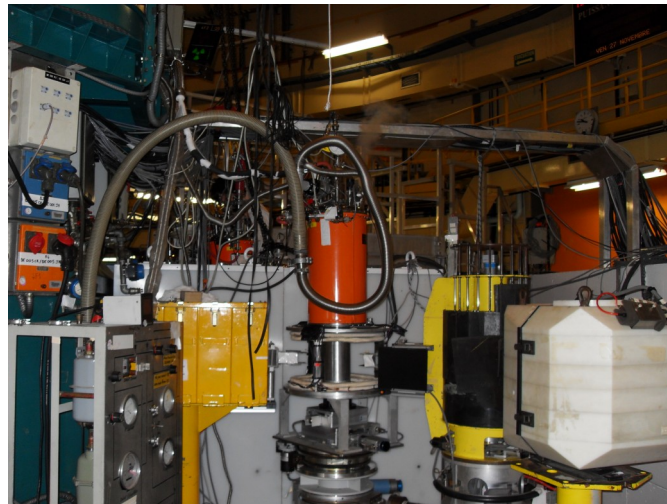


Figure 2 : Frequency at 160 K (a) and damping (b) of the LA (circles) and degenerate TA (triangles) modes propagating along the aperiodic c^* direction of *n*-nonadecane/urea. Dotted lines in (a) and (b) describe the usual LA behavior.



The 4F1 triple-axis spectrometer

References

1. T. Janssen, G. Chapuis, and M. de Boissieu, *Aperiodic Crystals: From Modulated Phases to Quasicrystals*. (Oxford University Press, Oxford, 2007).
2. J. D. Axe and P. Bak, *Phys. Rev. B* 26, 4963 (1982).
3. B. Toudic et al., *Science* 319, 69-71 (2008).
4. B. Toudic, R. Lefort, C. Ecolivet, L. Guérin, R. Currat, P. Bourges and T. Breczewski, *Phys. Rev. Lett.* 107, 205502 (2011).

Neutron and chirality: experiments and simulation

V. SIMONET^A, M. LOIRE^A, S. PETIT^B & R. BALLOU^A

A Institut Néel, BP 166, 38042 Grenoble

B Laboratoire Léon Brillouin, CEA-CNRS, CEA Saclay, 91191 Gif-sur-Yvette, France

virginie.simonet
@grenoble.cnrs.fr

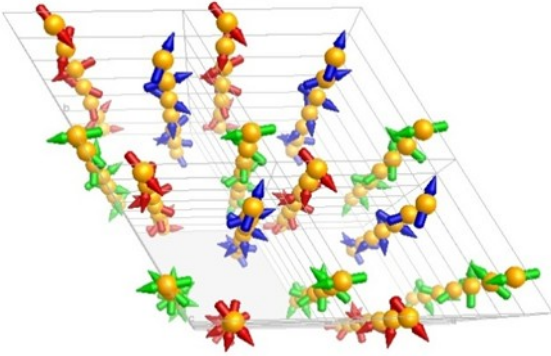


Figure 1 : Magnetic structure of $Ba_3NbFe_3Si_2O_{14}$

Ubiquitous in nature, chirality is what distinguishes a phenomenon from its materialization in a mirror [1]. Condensed matter physics and especially magnetism provide a rich playground to investigate this phenomenon, as it appears naturally to describe the arrangement of mag-

netic moments in non-collinear magnets. Here we report neutron experiments performed in the $Ba_3NbFe_3Si_2O_{14}$ langasite (BNFS) [2], along with numerical simulations, describing a pure chiral phase as well as chiral excitations. .

In magnetism, the chirality accounts for the sense of rotation of the spins on moving along an oriented line. The latter can be a straight line around which the spins form a helix, or an oriented loop, for instance a triangle, at the summits of which the spins are orientated at 120° from each other. For such coplanar spin configurations, it can be uniquely characterized on a bond connecting two consecutive spins \mathbf{S}_i and \mathbf{S}_j by the parity breaking vector product $\mathbf{S}_i \times \mathbf{S}_j$, defining the magnetic vector chirality. As far as domains of opposite chiralities are equipopulated, the chirality is usually averaged to zero in centrosymmetric magnets. However, in non-centrosymmetric compounds as for instance in the $Ba_3NbFe_3Si_2O_{14}$ langasite (BNFS) [2], neutron experiments have evidenced pure chiral phases. Actually, these studies focused on the ground state properties and the way the associated excited states inherit from the chiral properties remains an open issue. In a recent publication [3], we addressed this question, investigating the spin dynamics in a BNFS single crystal by means of neutron scattering.

BNFS crystallizes in the acentric space group P321 which confers the compound a structural chirality denoted $\varepsilon_r = +/-1$ for right(left)-handedness. The magnetic carriers are the Fe^{3+} ions arranged on trimers whose centers form triangular lattices perpendicular to the trigonal c axis (see Fig. 1). A magnetic order sets in below the Néel temperature $T_N = 27$ K. The spins lie in the (a, b) plane with the same 120° configuration on each triangle unit, thus exhibiting a single triangular chirality, denoted ε_D . This planar arrangement is helically propagated along the c -axis with a period $1/\tau \sim 7$, and a single chirality

(named helicity), denoted ε_H . A global overview of the spin waves was provided by unpolarized experiments performed on the ToF spectrometer IN5 at the ILL (on a single crystal in rotation around the vertical zone axis a [4]) allowing to measure the magnetic dynamical structure factor $S(Q, \omega)$, associated to symmetric spin correlations. As shown in Fig. 3, two spin-wave branches emerging from the magnetic satellites are identified. Further polarized experiments carried out on IN20 confirmed the magnetic origin of the two modes. By extracting the chiral magnetic dynamical scattering $C(Q, \omega)$, associated with antisymmetric spin correlations, we could establish that the lower mode is achiral whereas the upper mode has is fully chiral over the whole energy spectrum.

Meanwhile, owing to developments in numerical and computer science, numerical simulations have become an important trend in physics and a useful tool to design and explain experiments. Using the “spinwave” software developed at LLB, based on the standard Holstein-Primakov formalism in the linear

approximation [5], we could determine the correlation functions and reproduce quantitatively the observed spectra. The in-plane 120° spin arrangement is stabilized by antiferromagnetic intra-trimer J_1 and inter-trimer J_2 interactions within the (a, b) planes. Three interplane interactions, J_3 – J_5 , connect each moment to the 3 moments of the upper or lower trimer along the c axis (see Fig 2). The acentric structure imposes different J_3 and J_5 , oppositely

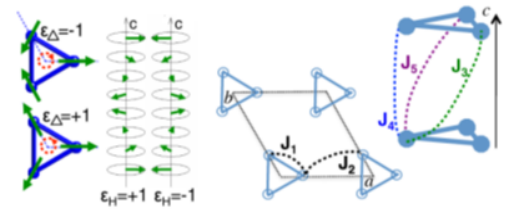


Figure 2 : Different chiralities in $Ba_3NbFe_3Si_2O_{14}$

approximation [5], we could determine the correlation functions and reproduce quantitatively the observed spectra. The in-plane 120° spin arrangement is stabilized by antiferromagnetic intra-trimer J_1 and inter-trimer J_2 interactions within the (a, b) planes. Three interplane interactions, J_3 – J_5 , connect each moment to the 3 moments of the upper or lower trimer along the c axis (see Fig 2). The acentric structure imposes different J_3 and J_5 , oppositely

twisted around c . The dominant one drives the helical modulation according to the structural and triangular chiralities; the two weakest interactions allow tuning the periodicity of the helix. This model implies that the magnetic and structural chiralities are related $\epsilon_{\Delta} = \epsilon_T \epsilon_H$. For the investigated crystal, $\epsilon_T = -1$ is observed (strong J_5), imposing opposite senses of rotation for the helicity and the triangular chirality. We are left with two different solutions (out of four) for the magnetic chiralities ($\epsilon_H=1, \epsilon_D=-1$ and $\epsilon_H=-1, \epsilon_D=1$). The observed ultimate selection of a single magnetic chirality was proposed [2,6] to originate from the antisymmetric Dzyaloshinskii-Moriya exchange interaction.

As shown in Fig. 3, an excellent agreement between experiment and calculation is achieved with the exchange parameters (in meV) $J_1 = 0.85 \pm 0.1$, $J_2 = 0.24 \pm 0.05$, $J_3 = 0.053 \pm 0.03$, $J_4 = 0.017$, and $J_5 = 0.24 \pm 0.05$ and a DM vector along c of 1% $|J_1|$. As shown in Fig. 4, the calculations demonstrate that $S(Q, \omega)$ reflects the structural chirality ϵ_T . The spectral weights of the branches emerging from the $+\tau$ and $-\tau$ are inverted between the two structural chiralities. On the other hand, $S(Q, \omega)$ does not depend on the magnetic chiralities. The two corresponding ground states yield how-

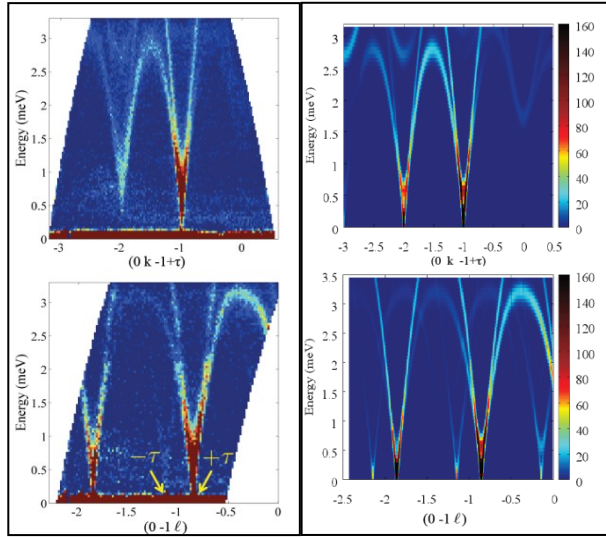


Figure 3 : (left) inelastic neutron scattering intensities at 1.6 K in the (b^*, c^*) scattering plane on the ToF spectrometer IN5. Displayed are intensity maps along $(0, k, -1+t)$ and $(0, -1, l)$ lines in the reciprocal space (Q -cuts). (right) Numerical simulations of $S(Q, \omega)$.

ever different $C(Q, \omega)$ with opposite sign. $S(Q, \omega)$ and $C(Q, \omega)$ are therefore a strong fingerprint of the ground state global chirality.

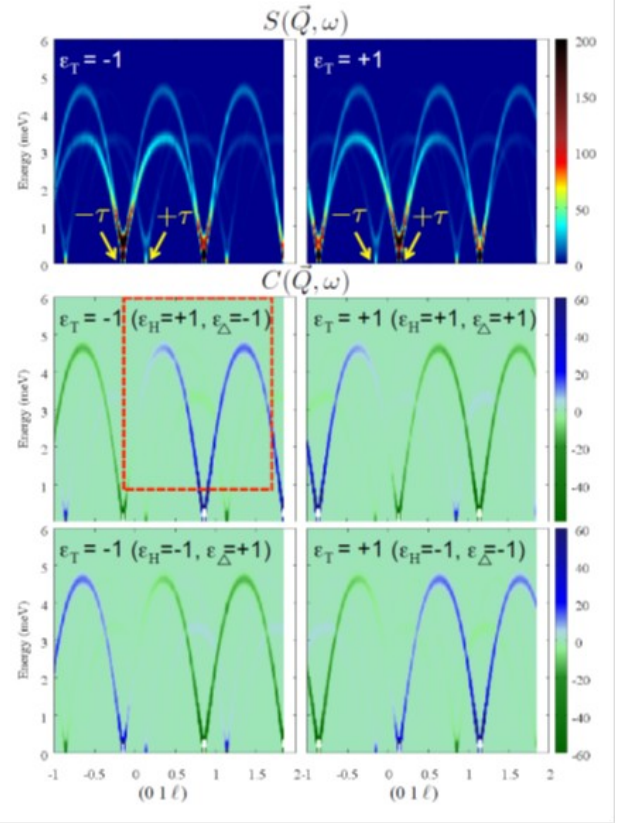


Figure 4 : Calculated $S(Q, \omega)$ and $C(Q, \omega)$ for different chiral configurations. The red frame points out the calculation agreeing with the experiment.

This establishes the observation of a dynamical chirality unbiased by macroscopic time-reversal symmetry breaking (*i.e.* in strictly zero magnetic field), but solely associated with the space inversion symmetry breaking. This intrinsic property of the spin waves is here highlighted thanks to the chiral single domain ground state of the BNFS compound.

References

1. G. H. Wagnière, "On Chirality and the Universal Asymmetry", Wiley VCH, Zürich, Weinheim, 2007.
2. K. Marty, *et al*, *Phys. Rev. Lett.* 101, 247201 (2008).
3. M Loire *et al*, *Phys. Rev. Lett.* 106, 207201 (2011).
4. J. Ollivier *et al.*, *Neutron News* 21 (2010) 22.
5. S. Petit, in *Neutron and Simulations*, EDP Sciences, ISBN 978-2-7598-0651-5
6. A. Zorko *et al*. *Phys. Rev. Lett.* 107, 257203 (2011).

Structure and magnetic properties of $\text{In}_2\text{RuMnO}_6$ and $\text{In}_2\text{RuFeO}_6$: heavily transition-metal doped In_2O_3 -type bixbytes

C. DE LA CALLE^A, M. J. MARTÍNEZ-LOPE^A, V. POMJAKUSHIN^B, F. PORCHER^C & J. A. ALONSO^{A*}

^A Instituto de Ciencia de Materiales de Madrid, C.S.I.C., Cantoblanco E-28049 Madrid, Spain.

^B Laboratory for Neutron Scattering, ETH Zurich and PSI Villigen, CH-5232 Villigen PSI, Switzerland.

^C Laboratoire Léon Brillouin, CEA-CNRS, CEA Saclay, 91191 Gif-sur-Yvette, France.

ja.alonso@icmm.csic.es

It is well known that In_2O_3 is able to dissolve certain amounts of transition metals but, at ambient pressure, the solubility is rather small, inferior to $s = 0.5$ in $\text{In}_{2-s}\text{M}_s\text{O}_6$; here we describe a substantial incorporation of magnetic transition metals into In_2O_3 of half of the metal positions ($s = 1$), by simple thermal treatment at temperatures in the 1300–1400°C range. The crystal structure of $\text{In}_2\text{RuMnO}_6$ and $\text{In}_2\text{RuFeO}_6$ has been studied at room temperature (RT) from high-resolution neutron

powder diffraction (NPD) data. In, Ru and $M = \text{Mn, Fe}$ are distributed at random over the metal sites of a $\text{C-M}_2\text{O}_6$ bixbyte-type structure, space group $Ia-3$, with $a = 9.89000(3)$ Å for $M = \text{Mn}$ and $a = 10.07536(4)$ Å for $M = \text{Fe}$. The magnetic properties suggest valence equilibrium $\text{Ru}^{3+}/\text{M}^{3+} \leftrightarrow \text{Ru}^{4+}/\text{M}^{2+}$. $\text{In}_2\text{RuFeO}_6$ shows antiferromagnetic interactions below $T_N \sim 95$ K, with a very weak ferromagnetism effect at low temperatures.

Indium-based perovskites containing Fe and Mn have only been stabilized under high-pressure conditions [1–5], with compositions $(\text{In}_{1-x}\text{M}_x)\text{MO}_3$ ($x = 0.112$ – 0.176 and $M = \text{Fe}_{0.5}\text{Mn}_{0.5}$) [1] or $(\text{In}_{1-y}\text{Mn}_y)\text{MnO}_3$ [5]. Some of them attracted much attention as new RT multiferroic materials [1–3]. In fact, with In^{3+} ($i.r. = 0.92$ Å) the perovskite structure becomes unstable and leads to the stabilization of a C-type R_2O_6 bixbyte structure, as adopted by ScVO_3 [6, 7]. In our work, we describe new complex oxides containing In, Mn/Fe and Ru with bixbyte structure; we report on a detailed structural and magnetic study carried out from neutron powder diffraction data in complement with magnetic susceptibility measurements.

In_2RuMO_6 ($M = \text{Mn, Fe}$) materials were obtained in powder form by a citrate technique. Stoichiometric amounts of analytical grade In_2O_3 , RuO_2 and $\text{C}_2\text{FeO}_4 \cdot 2\text{H}_2\text{O}$ or MnCO_3 were treated in citric acid with some droplets of HNO_3 . The organic resin was dried at 120°C and slowly decomposed at temperatures up to 600°C for 12 h. The precursor with $M = \text{Mn}$ was then heated at 900°C, 1000°C, 1300°C with intermediate grinding for 12 h. To obtain the clean sample with $M = \text{Fe}$ a final heating at 1400°C was necessary. The first characterization was performed by XRD. A NPD diagram for $\text{In}_2\text{RuFeO}_6$ was collected at RT and low-T (HRPT, SINQ, at PSI, in Switzerland, and D20, ILL, in France, respectively). For $\text{In}_2\text{RuMnO}_6$ the NPD diagrams were recorded at RT (3T2, LLB, Saclay in France). The magnetic susceptibility was measured with a commercial SQUID magnetometer on powdered samples, in the temperature range 5–330 K.

was performed in the $Ia-3$ (No. 206) space group, using the In_2O_3 bixbyte structure as starting model [8]. At first, we considered that In, Ru and M atoms were distributed at random at $24d$ and $8b$ positions with 2:1:1 occupancy. We assumed that half of the $24d$ and $8b$ sites are occupied by In and then the mixed occupancy of Ru: M over the two sites was refined with a single parameter, constrained to the departure stoichiometry. For $M = \text{Fe}$ the refinement rapidly converged in a unique way, with improvement of the quality of the fit, with a final Bragg R-factor of 2.40%, Fe atoms showing a preferred occupancy of the $24d$ sites. For $M = \text{Mn}$, by unconstraining the occupancy factors of both sites a clear deficiency of Mn with respect to the ideal stoichiometry was observed. The final crystallographic formula is $\text{In}_2\text{Mn}_{0.79(1)}\text{Ru}_{1.21(1)}\text{O}_6$. In this case the final Bragg discrepancy factor is of 2.72%. The Mn_3O_4 impurity, segregated from the main phase, was included as a second phase in the refinement. The quality of the fit is illustrated in Fig. 1 for $M = \text{Mn}$. A view of the crystal structure is shown in Fig. 2.

The crystal structure is an assembly of edge-sharing, distorted octahedral groups: each octahedral coordination group shares six edges. The first type of metal ion, In1, has 2 oxygens at each of the distances 2.206, 2.211 and 2.108 Å with an average bond-length of 2.175 Å for $M = \text{Mn}$, and 2.193, 2.144 and 2.065 Å for $M = \text{Fe}$, with an average bond-length of 2.134 Å. The second type, In2, has 6 equidistant O neighbors at 2.155 Å and 2.130 Å, for $M = \text{Mn, Fe}$ respectively. The determination of the valences of the metal elements by the bond-valence theory [9–11] from the In–O and In2–O distances is misleading, since the three elements (In, Ru and M) are distributed at random over the same crystallographic positions; valences close to 3⁺ are obtained for In at both In1 and In2 sites, whereas for Ru too-low valences between 2 and 2.5⁺ are observed, and also 2⁺ for $M = \text{Fe, Mn}$. It is clear that Ru and M are statistically occupying too big sites for their ionic sizes; hence an unrealistically low bond-valence derives from such calculation. Between the couples $\text{Ru}^{3+}/\text{M}^{3+}$ or $\text{Ru}^{4+}/\text{M}^{2+}$, there is probably an

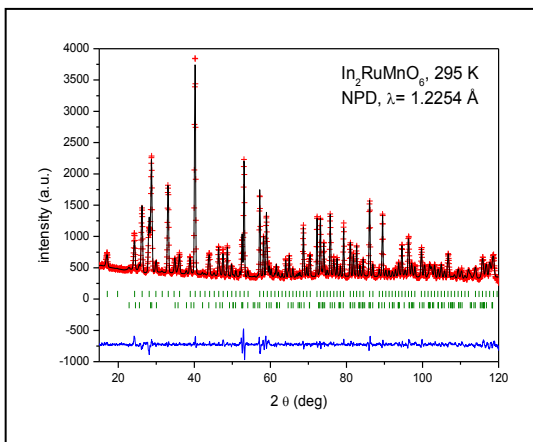


Figure 1. Rietveld plot of $\text{In}_2\text{RuMnO}_6$ bixbyte, from NPD data collected at RT at 3T2 high-resolution diffractometer.

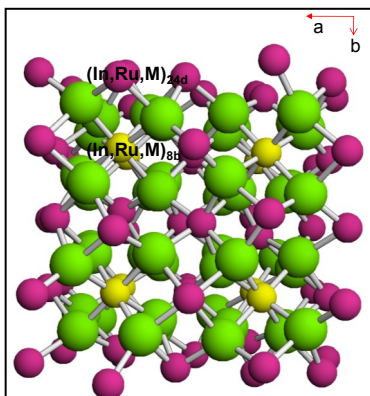


Figure 2. View of the crystal structure along c axis.

The structural refinement from RT high-resolution NPD data of In_2RuMO_6 ($M = \text{Mn, Fe}$)

equilibrium or a partial charge disproportionation effect ($\text{Ru}^{3+}/\text{M}^{3+} \leftrightarrow \text{Ru}^{4+}/\text{M}^{2+}$).

The magnetic properties of the $M = \text{Mn}$ *bixbyte* phase are significantly masked by the presence of Mn_3O_4 with spinel structure (Hausmanite). For $\text{In}_2\text{RuFeO}_6$, obtained as a pure *bixbyte* phase, ZFC and FC magnetic susceptibilities are perfectly coincident (Fig. 3a); the inset displays the reciprocal susceptibility vs T measured in the FC mode.

A linear Curie-Weiss fit between 100 and 300 K gave $\mu_{\text{eff}} = 7.18(1) \mu_{\text{B}}$. The calculated value for high-spin Ru^{4+} ($S = 2$) and high-spin Fe^{2+} ($S = 2$) is $6.93 \mu_{\text{B/f.u.}}$, whereas for a $\text{Ru}^{3+}(S = 5/2)/\text{Fe}^{3+}(S = 5/2)$ configuration, the estimated value of the paramagnetic moment is $8.36 \mu_{\text{B}}$. The determined moment suggests a $\text{Ru}^{4+}/\text{Fe}^{2+}$ configuration, with a slight admixture of $\text{Ru}^{3+}/\text{Fe}^{3+}$. The observed Weiss temperature is $\theta_{\text{Weiss}} = -282$ K, suggesting antiferromagnetic interactions, that may lead to an antiferromagnetic coupling below $T_{\text{N}} = 95$ K, were the reciprocal susceptibility deviates from the linearity (Fig. 3a, inset). The 4 K isotherm (Fig. 3b) is linear with a subtle curvature, characteristic of an antiferromagnetic system with a slight canting or weak ferromagnetism effect. Low-temperature NPD data were collected for $\text{In}_2\text{RuFeO}_6$ to assess the possible establishment of a long-range magnetic structure. After the refinement of the crystal structure at 2 K ($a = 9.8915 \text{ \AA}$), which basically displays the same features as the RT phase, a single tiny peak at $43.8^\circ 2\theta$ is the only symptom of a long-range magnetic arrangement. This peak can be indexed with a propagation vector $\mathbf{k} = (0, 0, 1/3)$. The resolution of a magnetic structure has not been possible from the insufficient information of magnetic origin exhibited by the pattern. These long-range magnetic interactions are probably driven by Fe-O-Fe magnetic couplings generated in Fe-rich regions of the structure, given that Fe is statistically distributed with non-magnetic In over the 24d sites (and, in minor proportion, over the 8b positions). Transport measurements display a resistivity higher than $40 \times 10^6 \text{ W cm}^{-1}$ at 295 K. The thermal variation of the resistivity was not measured.

In summary, In_2RuMO_6 ($M = \text{Mn, Fe}$) crystallizes in the C- M_2O_3 or *bixbyte* structure, as demonstrated from a high-resolution NPD analysis. For $M = \text{Mn}$, a statistical distribution of In, Ru and Mn are observed over the 24d and 8b crystallographic sites;

for $M = \text{Fe}$ this metal shows a preference for the 24d site. Thus, we describe a substantial incorporation of magnetic transition metals into half of the metal positions ($s = 1$) of In_2O_3 , by simple thermal treatment at temperatures in the 1300-1400°C range.

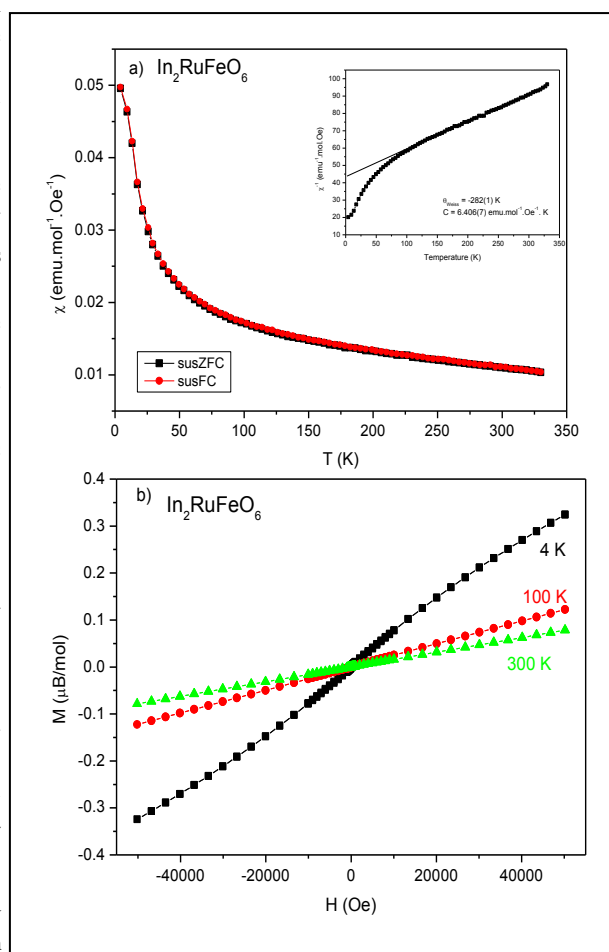
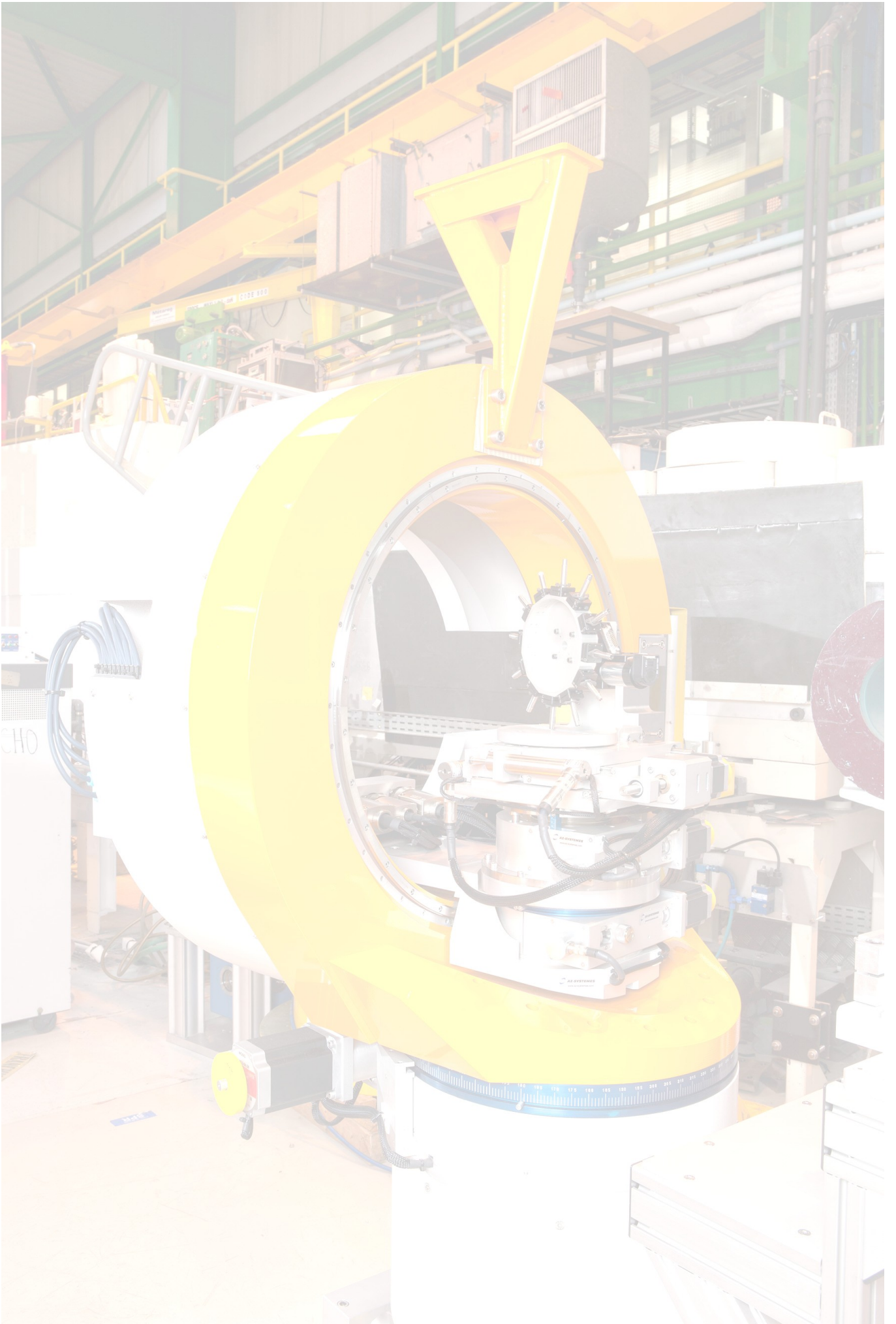


Figure 3. a) Magnetic susceptibility of $\text{In}_2\text{RuFeO}_6$; inset: reciprocal susceptibility; b) Isothermal magnetization curves at 4, 100 and 300 K.

The magnetic measurements of the Fe compound display antiferromagnetic interactions below $T_{\text{N}} \sim 95$ K, probably driven by Fe-O-Fe magnetic couplings generated in Fe-rich regions of the structure.

References

1. A.A. Belik, T. Furubayashi, Y. Matsushita, M. Tanaka, S. Hishita, E. Takayama-Muromachi, *Angew. Chem.* 121 (2009) 6233,
2. A. A. Belik, T. Furubayashi, Y. Matsushita, M. Tanaka, S. Hishita, E. Takayama-Muromachi *Angew. Chem. Int. Ed.* 48 (2009) 6117-6120.
3. E. Kan, H. Xiang, C. Lee, F. Wu, J. Yang, M.H. Whangbo, *Angew. Chem.* 122 (2010) 1647; *Angew. Chem. Int. Ed.* 49 (2010) 1603-1606.
4. J.A. Alonso, *Chem. Phys. Chem.* 11 (2010) 58-60.
5. A. A. Belik, Y. Matsushita, M. Tanaka, E. Takayama-Muromachi, *Angew. Chem. Int. Ed.* 49 (2010) 7723-7727.
6. J.A. Alonso, M.T. Casais, M.J. Martínez-Lope. *J. Chem. Soc. Dalton Trans.* (2004), 1294-1297.
7. E. Castillo-Martinez, M. Bieringer, S.P. Shafi, L.M.D. Cranswick, M.A. Alario-Franco. *J. Am. Chem. Soc.* 133 (2011) 8552-8563.
8. M. Marezio, *Acta Crystallogr.* 20 (1966) 723-728.
9. I. D. Brown, *Structure and Bonding in Crystals*, eds. M. O'Keefe and A. Navrotsky, (New York: Academic Press) vol.2 (1981) p.1.
10. N. E. Brese, M. O'Keefe, *Acta Crystallogr. Sect. B* 47 (1991) 192-197.
11. I. D. Brown, *Z. Kristallogr.* 199 (1992) 255-272.



AXE 2: MATERIALS AND NANOSCIENCES: FUNDAMENTAL STUDIES AND APPLICATIONS.

The second axis “Materials and Nanosciences: Fundamental Studies and Applications“, covers the activities related to the research in materials sciences and more generally in hetero-systems (interfaces, alloys, composites materials, confined systems). The studies cover detailed structures of nano-objects, interactions between nano-objects, and the role of nanostructures in composite materials. The length-scales which characterize the properties of the systems range between 1-100 nm. More specifically the following areas are addressed at the LLB: *Magnetic nanostructures* (metallic layers, oxide epitaxial layers, nanoparticles) studied by diffraction, SANS and reflectometry; *Composite materials* (polymer reinforcement by nano-particles, metallurgical composites) whose properties are studied by SANS; *Metallurgy* (both fundamental and industrial). Textures and Strain heterogeneities are studied by diffraction in various alloys or nuclear materials; *Confined systems* (microporous materials and organized guest-hosts systems, mesoporous materials and organized guest-hosts systems) in which the dynamics of the confined elements can be studied by inelastic scattering techniques; *Amorphous materials* (disordered systems – glasses). The local atomic order is also investigated by diffraction.

- 1) **NEUTRON PRECESSION SPECTROSCOPY: A NEW METHOD TO PROBE IN-DEPTH MAGNETIC MICROSTRUCTURES**
P.Thibaudeau, F. Ott, A. Thiaville

- 2) **HOW MUCH WATER DOES PENETRATE INTO THE SILICA UNDER STRESS?**
E. Bouchaud, F. Lechenault F.Cousin, C. L. Rountree

- 3) **SANS/VANS INVESTIGATION OF POROSITY MICROSTRUCTURE IN ROCKS FROM A NATURAL CO₂ RESERVOIR.**
G. Bicocchi, R. Magli, A. Brulet, M.-H. Mathon

- 4) **WHAT IS THE STRUCTURE OF LIQUID BISMUTH?**
E. N. Caspi, Y. Greenberg, E. Yahel, G. Makov, B. Beuneu

- 5) **COMPOSITION AND STRUCTURE OF SOLID SOLUTIONS IN THE BI₂O₃—SiO₂—V⁵⁺₂O₅ SYSTEM WITH THE STRUCTURE SILLENITE**
T. Mel'nikova, G. Kuz'micheva, V. Rybakov, N. Bolotina, A. Cousson

- 6) **SYNTHESIS AND STRUCTURE DETERMINATION OF THE HIGH TEMPERATURE FORM OF LA₂WO₆**
M. Allix, M.H. Chambrier, E. Véron, F. Porcher, M. Suchomel, F. Goutenoire

Neutron Precession Spectroscopy: a new method to probe in-depth magnetic microstructures

P. THIBAudeau^A, F. OTT^B & A. THIAVILLE^C

A CEA/Le Ripault, DAM, BP 16, F-37260, Monts

B Laboratoire Léon Brillouin, CEA-CNRS, CEA Saclay, 91191 Gif-sur-Yvette, France

C Laboratoire de Physique des Solides, Univ. Paris-Sud, CNRS UMR 8502, 91405 Orsay

pascal.thibaudeau@cea.fr

An experimental method is presented which allows probing the shape of a magnetic domain wall created within the thickness of a soft magnetic double film with equivalent in-plane anisotropies oriented at 90° [1]. The method is based on the precession of the spin of neutrons travelling across the domain wall structure. The technique is experimentally

Polarized neutrons transmission is a technique developed very early [2] to probe the magnetic structure of materials. However, Newton and Kittel have suggested, also early, that neutron spin precession (without depolarization) could be used to probe the internal structure of a domain wall, for example to measure the thickness of a 180° Bloch wall [3]. A generalization of this idea is presented to a technique imaging magnetic structures within the thickness of the sample, through neutron spin precession. A polarized neutron reflectometer is used to perform transmission measurements, over a wide range of neutron precession paths. As a first non-trivial demonstration of the technique, measurements of a 90° in-plane Bloch wall within the thickness of a sample are presented. This wall is stabilized by engineering the magnetic anisotropy across the film thickness. The neutron velocity variation is realized by varying the (grazing) incidence angle of the neutron beam as shown in Fig. 1.

demonstrated on a planar (half)-Bloch wall created within the thickness of a soft magnetic double film with equivalent in-plane anisotropies oriented at 90° [1].

The experiments were performed on the polarized neutron reflectometer PRISM at the Laboratoire Léon Brillouin. Precession spectra as a function of grazing angle were measured for several applied fields and sample orientations. The smallest incidence angle considered is of the order of 0.7°, for which the classical precession approach is still valid. Instead of trying to reproduce every spectrum by a magnetization profile as a function of position across the sample thickness, the micromagnetic parameters for the bilayer that allowed reproducing best one spectrum (namely with a neutron spin along [010]) were adjusted by trial and error.

It was observed that reproducing this spectrum did put severe constraints on the micromagnetic

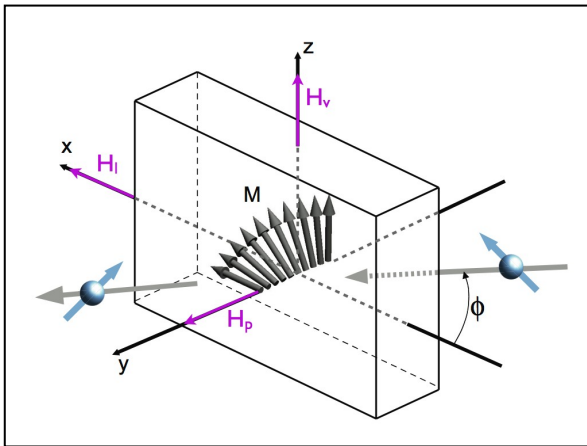


Figure 1: Sketch of the experiment geometry and definition of axes and field components: longitudinal (H_l), perpendicular (H_p) and vertical (H_v). The magnetization lies in the plane of the sample (defined by an angle θ with the z -axis), the field in the plane of the sample is defined by an angle ψ with the z axis, and the neutron beam travels in the $x - y$ plane

The evolution of the spin direction of a neutron travelling through the magnetic material is determined by the classical precession equation. The emerging spin state is analyzed as a non spin flip intensity.

Calculated precession spectra (through a numerical solution of the equation of precession) for samples with a non-uniform magnetization in the form

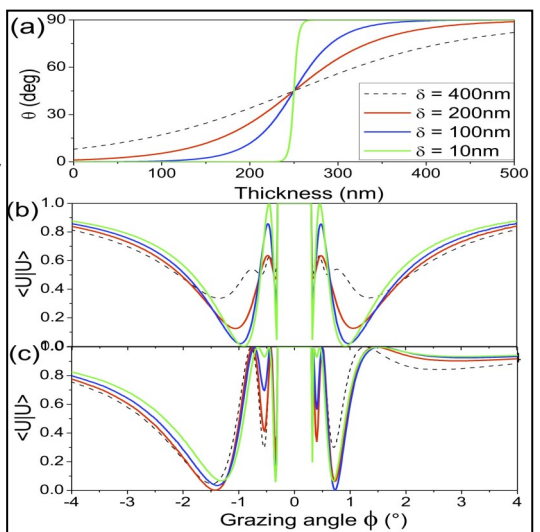


Figure 2 : (a) Profiles of 90° domain walls with different thickness (400, 200, 100, and 10 nm) in a 500 nm film. The magnetization rotates from the (Oz) to the (Ox) axis. (b -c) Calculated precession spectra using the parameters of the experiments. The incident neutron spin is along [100] (b), or along $[1/\sqrt{2} \ 1 \ 1/\sqrt{2}]$ (c).

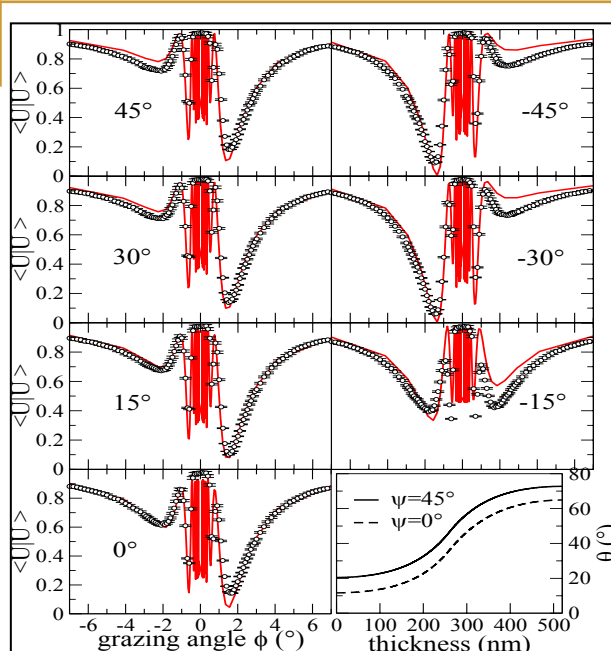
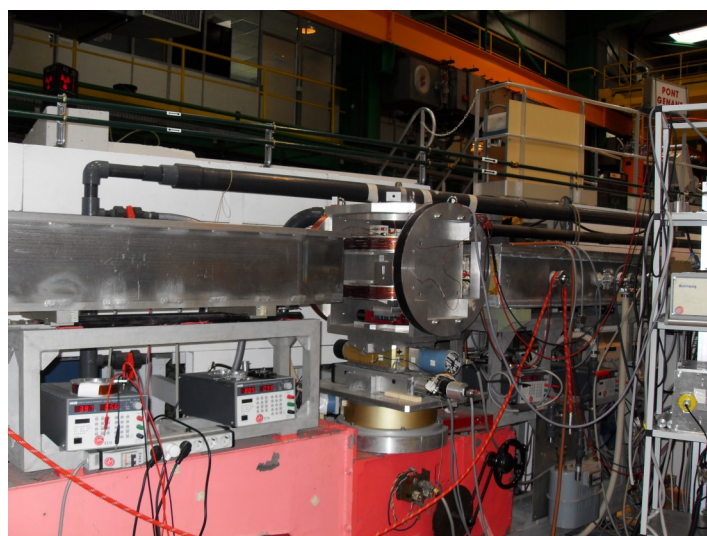


Figure 3 : Experimental transmission spectra for several values of a rotating magnetic field with in-plane components along different angles, the nominal easy axis of the first layer being vertical. The applied field has also a perpendicular component so that the neutron comes with a spin at 45° of the sample plane. The curves show the result of the micromagnetic modeling followed by the calculation of neutron spin precession

parameters of the model. The transmission ratios were then measured for other configurations of applied magnetic fields, consisting in a perpendicular field H_p together with an in-plane field H_{ip} of varying orientation as shown in Fig.3. The field $H_p = 400$ A/m was applied in order to have a component normal to the sample plane, a necessary condition to observe asymmetric spectra. This field is small in comparison with M_s and does not affect the magnetization configuration.

With the sample parameters determined above, micromagnetic modeling reproduced very well the series of the 7 spectra measured in this run, proving that we have determined by this technique the wall profile. Note for example that the sharp minimum adjacent to this shallow minimum is also well reproduced, confirming the correct evaluation of the domain wall width.

This method provides an alternative to polarized neutron reflectometry for thicker samples. However, it also requires a non-trivial inversion.



The PRISM reflectometer

References

1. Thibaudeau P., Ott F., Thiaville A., Dubuget V., and Duverger F., *Europhys. Lett.* **93**, 37003 (2011).
2. Halpern O. and Holstein T., *Phys. Rev.* **59**, 960 (1941).
3. Newton R. and Kittel C., *Phys. Rev.* **74**, 1604 (1948)

How much water does penetrate into the silica under stress?

E. BOUCHAUD^A, F. LECHENAULT^A, F. COUSIN^B & C. L. ROUNTREE^C

A CEA/IRAMIS/SPEC, CNRS
URA 2464, 91191 Gif-sur-
Yvette

B Laboratoire Léon Brillouin,
CEA-CNRS, CEA Saclay,
91191 Gif-sur-Yvette, France

C CEA/IRAMIS/SPCSI, 91191
Gif-sur-Yvette

Corrosion under stress - combined action mechanical stresses and corrosion by water in the surrounding atmosphere - is often the source of crack propagation in glasses. A study by neutron reflectivity at the Laboratoire Léon Brillouin (IRAMIS / LLB) of samples of silica glass fractured under an atmosphere of heavy water (D₂O) shows a high penetration of water into the glass. Concentration under the fracture surface is so large that it suggests the presence of a high damage around the crack tip. These observations show the need to develop new models of corrosion under stress.

By observing the slow growth of cracks caused by the impact of a small stone on the windshield of your car, you will probably see a phenomenon of stress under corrosion. If your windshield were under high vacuum, these cracks would not propagate, because they are not sufficiently mechanically stressed. But exposed to a humid atmosphere, water molecules are helping mechanical stresses to allow the growth of cracks beginnings resulting from the initial shock.

While this phenomenon - and its nuisances! - has long been recognized, it is only in the eighties that the first models appeared. However, they are not entirely satisfactory: first, they do not

take into account the amorphous nature of the glass structure and on the other hand, they assume that the chemical reaction (hydrolysis) between the water and silica, which causes the breaking of atomic bonds in the glass, takes place in the crack tip and nowhere else. The aim of our study was to show that when the glass is under stress, even moderate, the water enters the glass and damage much more than just breaking atomic bonds at the crack tip.

We therefore sought to detect the presence of water in the glass. For this, the measurement of thermal neutron reflectivity is a technique sensitive to the presence of light elements, which can even rise by using heavy water (D₂O), whose presence changes the reflectivity ten times more than usual water (H₂O). After the controlled break of samples of pure silica under an atmosphere of heavy water, we measured the neutron reflectivity of the fractured surfaces as compared to that of a sample "control", not subject to constraints. Fig. 2 shows the reflectivity measured on the reflectometer EROS of LLB for two fractured surfaces obtained for different applied loads. We see that the reflectivity of these surfaces is significantly greater than that of the surface control, evidence for the presence of heavy water trapped in the broken samples.

In both cases studied, the measurements indicate an average depth of penetration of heavy water of about 10 nm below the surface of rupture with a very high concentration (35% for the load the lower 57% the highest load) on the first 4 nm.

The diffusion coefficient of water in silica is very low: a water molecule only could migrate a nanometer in more than a hundred days! Interpretation of the reflectivity curves measured then implies to take into account the acceleration of diffusion under effect of the constraint, very high at the crack tip. The relaxation induced by the growth of the

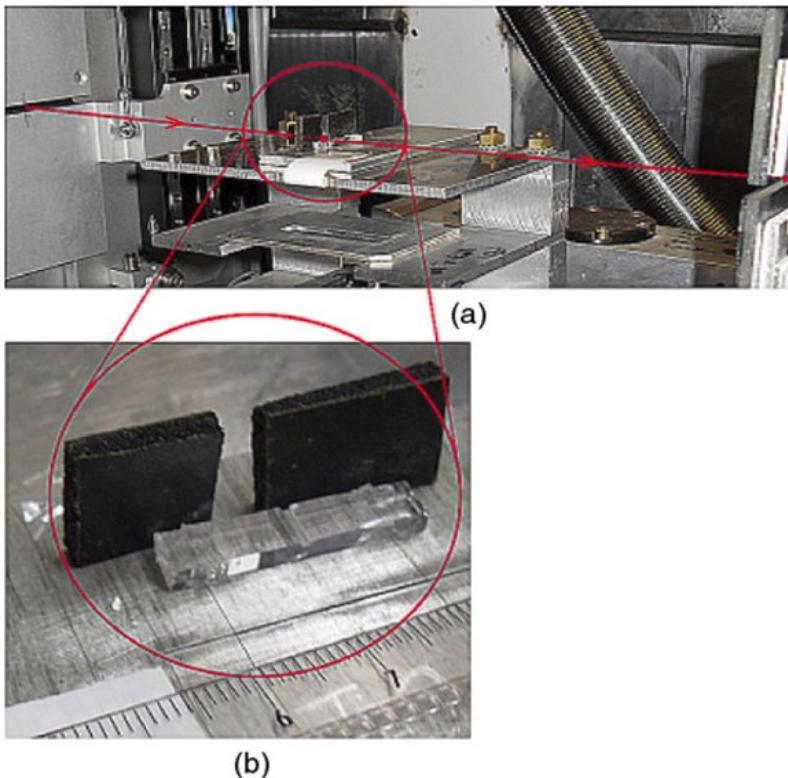


Figure 1: a) Experimental device (red line: neutron beam). b) Broken silica sample, before the black B4C plates, defining the region of analysis

crack, which trap the water released under the fracture surface of the material, changes its reflectivity for neutrons. In addition, the very high concentration of heavy water, measured in the first 4 nm below the surface, indicates that the diffusion under stress of water leads to a heavy damage of the material by corrosion.

A systematic study of the reflectivity as a function of the applied load could allow to propose a new model of stress corrosion of silica glass. The detailed study of this model system will bring a new understanding for a phenomenon of great technological importance.

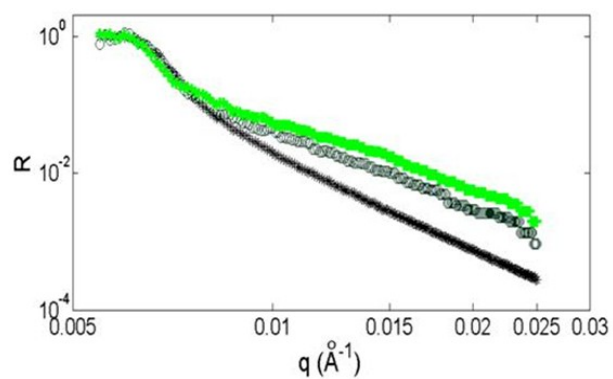


Figure 2 : Measured reflectivity plotted versus the scattering vector. Black Stars: control sample. Green symbols: fractured surfaces (solid symbols: greater applied load).



References

1. F. Lechenault, C. L. Rountree, F. Cousin, J.-P. Bouchaud, L. Ponson, E. Bouchaud *Phys. Rev. Lett.* 106, 165504 (2011).

SANS/VSANS investigation of porosity microstructure in rocks from a natural CO₂ reservoir.

G. BICOCCHI^A, R. MAGLI^B, A. BRULET^C & M.-H. MATHON^C

a Dept. of Earth Sciences, Univ. Florence, Italy

b Dept. of Chemistry, Biochemistry and Medical Biotechnologies, Univ. Milan, Italy

c Laboratoire Léon Brillouin, CEA-CNRS, CEA Saclay, 91191 Gif-sur-Yvette, France

gabriele.bicocchi@unifi.it

Carbon capture and storage (CCS) is considered a valid option to reduce the CO₂ concentration in atmosphere. The gas is collected from industrial plants, then injected and stored underground in geological reservoir. A very wide range of information about chemical-physical characteristics of the sequestration site is therefore needed and, among them, data on porosity microstructure are crucial. Part of the processes which affect micro-porosity and act during and after the rocks formation can be reconstructed by studying the micro-porosity features. We have therefore per-

formed a couple of SANS and VSANS experiments on rocks coming from a CO₂ reservoir (which represents a natural analogue of a CCS site) in order to define the role and the possible effects of CO₂ alteration in determining the micro-porosity and to check the sealing potential of rocks overlying the reservoir, which act as a barrier with respect to CO₂-rich gas. The collected data are expected to be beneficial for developing theoretical model about the effects of CO₂ sequestration in deep geological reservoirs.

Introduction

Sequestration of CO₂ in deep geological reservoirs represents one of the potential methods to reduce anthropogenic emissions into the atmosphere. In the long term, the injected fluid dissolves into the local formation of rocks and, when present, in saline deep aquifers, participating to a variety of geochemical reactions. The overall impact of these processes produces changes in mineralogy, texture, permeability and porous structure of the rocks, to a level which depends on the different lithology of the rocks. These changes can be investigated by considering what occurs in rocks with natural CO₂ accumulations, as analogues for geological sequestration. Also, computer simulations based on thermodynamics, kinetics and geochemical modelling can be beneficial. On the other hand, reliable data concerning the porous structure, which is so important to trap

CO₂, can be hardly extracted from computer simulations. Here the preliminary results of a SANS and VSANS investigation on rocks pertaining to a geological context (located in Eastern Tuscany, Central Italy) characterized by the presence of a deep gas reservoir are presented. The reservoir was intercepted at ~3,700 m depth by a bore-well drilled in the eighties and is presently hosting supercritical CO₂ (calculated density ~860 kg/m³) at the estimated pressure and temperature of 670 bars and 120 °

Experimental Settings

C. Texture and mineralogy of volcanic rocks samples, from drill cores located into the reservoir in the 3,864 to 3,871 m depth range, were found heavily modified by the interaction with CO₂-rich fluids [1].

SANS experiments on sedimentary, volcanic and metamorphic rocks have been reported since late eighties (e.g. [2],[3] and [4]). This non-destructive method was proven to be a powerful tool for getting information about porosity microstructure in rocks (e.g. dimension, distribution and shape of pores, see [5] and references therein). We have carried out two neutron scattering experiments: the first one using the PAXE diffractometer and the second one with the VSANS (Very Small Angle Neutron Scattering) TPA diffractometer. The two experiments covered globally the $\sim 6 \cdot 10^{-4}$ to $\sim 3 \cdot 10^{-1} \text{ \AA}^{-1}$ Q range, which in direct *d*-space means from $\sim 1 \text{ \mu m}$ to $\sim 4 \text{ nm}$. Samples of rocks from the reservoir and a selection of possible analogues of the same volcanic rocks, unaffected by CO₂ presence, were chosen for the experiments together with rocks, from outcrops, corresponding to the geological layers immediately overlying the reservoir. These samples are representative of different volcanic rocks and of sedimentary rocks bearing gypsum, dolomite, calcite. Samples have been thinned down to 2 and 5 mm thick slices; also, the sample corresponding to 3,870 m depth was cut in 5 different slices from 0.7 to 5 mm thickness, respectively. Indeed, previous studies [4] showed evidence that, depending on the wavelength, for thicknesses larger than 2 mm and for Q values smaller than 10^{-3} \AA^{-1} the effect of multiple scattering (MS) can be of some relevance.

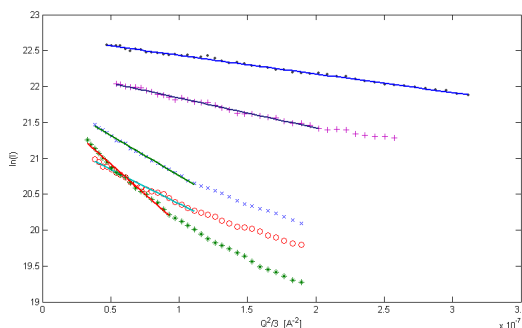


Figure 1: Guinier-like plots on some of the TPA data ($\lambda = 12 \text{ \AA}$): Burano rocks (\bullet), Volcanic rocks IG1($+$) and IG3 (o) not affected by CO₂, and Volcanic rocks 3864 (x) and 3870 ($*$) from the bore-well, therefore affected by CO₂. Straight lines represent the linear fit results. Statistical uncertainties are within the size of the symbols.

Experimental Results and Discussion

In this work we address two questions: a) which is the average pore size and b) which are the fractal dimensions shown by the selected rocks. For point a) the average pore size has been evaluated on samples with 2 mm thickness looking at the lower Q -range investigated with TPA ($\lambda = 12 \text{ \AA}$) and applying to the data a Guinier-like model

$\ln(I) = A Q^2 + B$, where I is the detected intensity as a function of the wavevector Q . Some of the resulting curves are shown in Fig. 1. The radius of the assumed spherical pores, related to the A coefficient, comes out to be roughly between 3300 and 4100 \AA with a 0.1% uncertainty for the volcanic rocks samples of the bore-well, while is significantly smaller, *i.e.* approximately between 2000 and 3100 \AA ($\pm 0.1\%$) for the possible analogues of the same volcanic rocks coming from outcrops and therefore believed not affected by CO_2 . Moreover, it is worth mentioning that the radius for the Burano samples comes out to be by far the smaller, being roughly 1600 \AA , so confirming the sealing role of those rocks overlying the reservoir. Concerning point b), if the data are modeled with a generalized Porod behaviour, *i.e.* with a power law $I(Q) = I_1 Q^{-x} + B$, from the exponent x the fractal dimension D_s for surface ($3 < x < 4$, with $D_s = 6-x$) or D_m for mass/volume ($2 < x < 3$, with $D_m = x$) can be derived [6]. We have applied this approach to the PAXE data ($\lambda = 7.8 \text{ \AA}$) in the $1.13\text{-}5.58 \cdot 10^{-2} \text{ \AA}^{-1}$ range. Some of the results curves are displayed in Tab. 1. The values of D_s for the CO_2 altered volcanic rocks lay in a wide range from 2.11 ± 0.03 (depth 3,864 m) to 2.76 ± 0.05 (depth 3,870 m), showing differences of more than 30%. A similar dispersion of values is also present in the bulk chemical (ICP-MS analysis) and mineralogical composition (XRD Rietveld refinement) of the investigated rocks. Both chemistry and mineralogical assemblage are consistently different from sample to sample, although they pertain to a contiguous drill core which is less than 10 meters long. In contrast, the D_s values relative to the analogue volcanic rocks, unaffected by CO_2 alteration, are confined between 2.33 ± 0.04 and 2.52 ± 0.04 , although these rocks come from different geological context. In the bore-well rocks the very different chemical and mineralogical composition and the wide range of D_s values found, can be interpreted considering that chemical alteration due to CO_2 -

rich fluids proceeded not homogeneously, likely due to the circulation of fluids in preferential paths. Moreover, it is worth mentioning that, for those rocks, there is a direct correlation between the radius of gyration and the D_s , *i.e.* higher values of surface fractal dimension are associated with larger

Table 1: Surface fractal dimension D_s from a generalized Porod law applied to some of the PAXE data ($\lambda = 7.8 \text{ \AA}$).

Sample ID	D_s
Rocks not affected by CO_2	
Burano	2.41 ± 0.09
IG1	2.36 ± 0.05
IG3	2.52 ± 0.04
IG2	2.33 ± 0.04
Rocks affected by CO_2	
3864	2.11 ± 0.03
3866	2.13 ± 0.06
3867	2.45 ± 0.05
3868	2.34 ± 0.05
3870	2.76 ± 0.05
3871	2.63 ± 0.05

pores sizes.

Conclusions

Several experimental approaches have been combined to get microscopic information on porosity and fractal features of rocks coming from a natural CO_2 reservoir as compared to similar rocks not affected by CO_2 . Among these approaches, the VSANS experiment allowed a preliminary determination of the average pore sizes, with indications of possible effects due to the CO_2 presence. Work is still in progress to deepen the analysis so that the shape of the pores can be evaluated and also a quantitative assessment of the porosity can be achieved. The SANS results about the surface fractal properties indicate a dispersion of the fractal dimensions for the bore-well rocks significantly larger than for the values found in rocks not affected by CO_2 presence. This confirms the results of chemical and mineralogical analysis, which give clear indications that chemical alteration due to CO_2 -rich fluids has affected the rocks along the paths chosen preferentially by those fluids. The collected data are expected to provide some help for developing theoretical model about the effects of CO_2 sequestration in deep geological reservoirs.

References

1. Bicocchi et al., *Proceedings of the 4th International Workshop on Compositional Data Analysis 2011*, 1-16.
2. Anovitz, et al., *Geochim. Cosmochim. Acta* 2009, 73, 7303–7324.
3. Lucido et al., *Phys. Rev. B* 1988, 38, 9031-9034.
4. Radlinski et al., *Phys. Rev. Lett.* 1999, 82, 3078–3081.
5. Radlinski, *Rev. Mineral. Geochem.* 2006, 63, 363-397.
6. Wong et al., *Phys. Rev. Lett.* 1986, 57, 637–640.

What is the structure of liquid bismuth?

E. N. CASPI^A, Y. GREENBERG^A, E. YAHIEL^A, G. MAKOV^B & B. BEUNELI^C

A NRCN, Beer-Sheva, Israel

B Ben-Gurion University, Beer-Sheva, Israel

C Laboratoire Léon Brillouin, CEA-CNRS, CEA Saclay, 91191 Gif-sur-Yvette, France

caspie@nrcn.org.il

The structure of liquid Bismuth is probably the best-studied among elemental liquid metals because of a combination of the interesting physical properties of Bismuth and its excellent neutron scattering properties. Transforming the structure factor into the radial distribution introduces new sources of error which causes the scatter to be greater than that required to resolve issues such as the existence of liquid-liquid phase transitions in Bi and to obtain correlation between thermo-physical properties and structure. Over the last six decades there have been more than 10 independent studies of the structure

of liquid Bi, near the melting temperature. This high number of measurements provides an opportunity to compare these results and to analyze the different sources of error contributing to the calculated pair distribution function. We consider the contribution of different parameters when transforming the structure factor to the radial distribution function. In particular, we vary the analysis procedure and the experimental configuration to demonstrate that an invariant structure factor can be obtained.

The radial distribution function (RDF) cannot be measured directly in real space. Instead, the liquid structure factor is obtained from the diffracted inten-

sity to account for scattering and absorption in the sample and the experimental setup. Following the application of these correction procedures, the accumulating systematic error in the case of neutron scattering from heavy elements is of the order of 4-5% [1-4]. An additional error is introduced by the measurement of a finite range of the momentum transfer, q , introducing errors into the RDF, most notably short wavelength oscillations (*i.e.* numerical noise). These oscillations may affect the interpretation of the RDF, and in particular prevent identification of small changes therein.

Here we report on two separate studies, 5 years apart, of the structure of liquid Bi at ambient pressure that we have performed at the 7C2 diffractometer at Saclay. Using different experimental setups, we show that the structure factors obtained agree to better than 1%. Using this structure factor as a reference, we compare a large number of experimental studies of liquid Bi at ambient pressure in order to investigate the experimental scatter in the structure factor and find out its significance. We then explore how the errors in the experimental determination of the structure factor affect the calculated RDF, focusing on two main issues: sensitivity to convergence in the high q range and choice of q_{\max} .

Structure factor – $S(q)$. In this work, we have the opportunity to compare our two measurements separated over 5 years using different setups, on the same instrument. This comparison can be undertaken to a high accuracy, while removing extraneous, non-physical sources of experimental scatter. The ratio between these two measurements of liquid bismuth $S(q)$ shows that the deviation is typically less

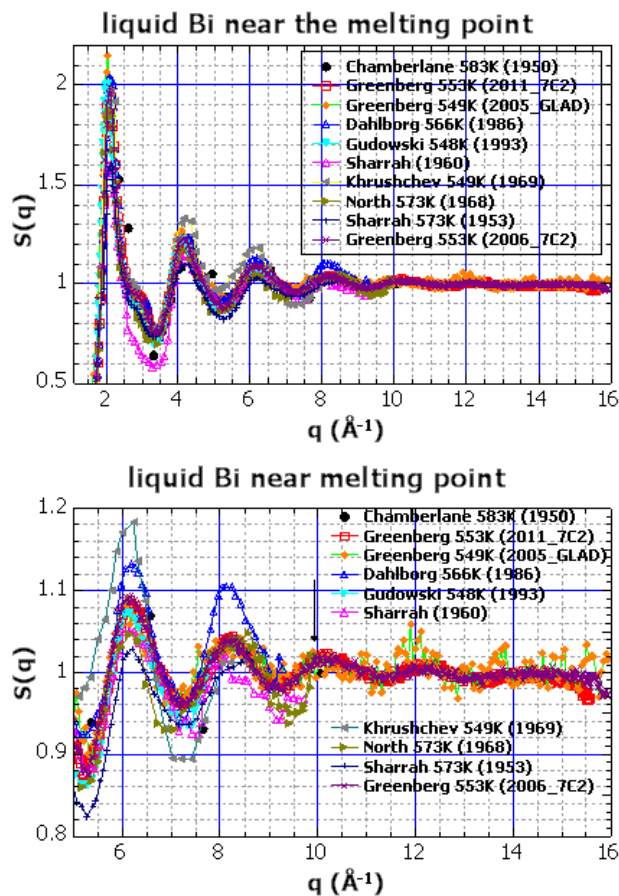


Figure 1: (top) various measurements of liquid bismuth structure factor near the melting point over the last 60 years.⁵⁻¹² (bottom) high q range of the structure factor.

sities by a series of approximations and corrections

than 1% i.e. of the order of the statistical noise (Fig. 1). This is an indication that the obtained structure factor is indeed “physical”. Nevertheless, since the analysis methods were the same in both cases, a systematic error due to uncertainties in dimensions of the diffractometer’s components within the beam path used for the absorption corrections [1], and the approximation made in the inelastic scattering corrections [3], cannot be ruled out. We compare our results with previous studies over the last 6 decades (Fig. 1). Clearly, the positions of the maxima and minima are essentially the same, as expected. In contrast, the amplitude of $S(q)$ varies considerably between the measurements. The magnitude of the variation is $\sim 30\%$ in $(S(q)^{-1})$ even for the first peak in $S(q)$. Moreover, relative scatter between measurements increases with increasing q . Finally, all measurements reduce to noise with the typical q_{\max} of 10 \AA^{-1} , with the exception of our results at 7C2 which extend to approximately 14 \AA^{-1} keeping a reasonable signal to noise ratio (Fig. 1b).

Radial distribution function – $G(r)$. Due to the experimental constraints, $S(q)$ can be determined only up to a value q_{\max} . A naïve approach is to use the maximum amount of q range available in the data, and, trivially, to aim for the longest measurement time. The effect of measurement statistical noise in determining the structure factor on the RDF was found to be negligible when number of neutron counts was increased sixfold.

We find that the oscillations in the RDF associated with the finite q -space measurements may increase with increasing q_{\max} . We consider the effect on the calculation of $G(r)$ of using different cut-off values [q_{\max} at the $S(q)$ measured data] at selected positions from a positive to negative node in $S(q)$ (cf. Fig. 1). Choosing the cut-off at a node, [$S(q_{\max})=1$], leads to a reduction in the oscillations with better results at a positive node. Choosing the cut-off at the highest available positive node requires caution if q_{\max} is in the region where the statistical noise is too high as illustrated by considering alternative choices of q_{\max} determined by the positive nodes of $S(q)$ (Fig. 2). requirement is met at a node, i.e. if $S(q_{\max})=1$. If we require that the variations in $\frac{dS(q)}{dq}$ are minimal, i.e.,

$$\frac{\partial^2}{\partial q_{\max}^2} \left(\frac{\partial \varepsilon}{\partial r} \right) = \frac{\partial}{\partial q_{\max}} \left(q_{\max}^3 (S(q_{\max})-1) \frac{q_{\max} r \cos q_{\max} r - \sin q_{\max} r}{(q_{\max} r)^2} \right) > 0$$

Then this condition is met at a node, if $S'(q_{\max}) > 0$, i.e. the node is positive.

Thus, we suggest the following requirement for the correct determination of $G(r)$ from a given $S(q)$ data: choosing

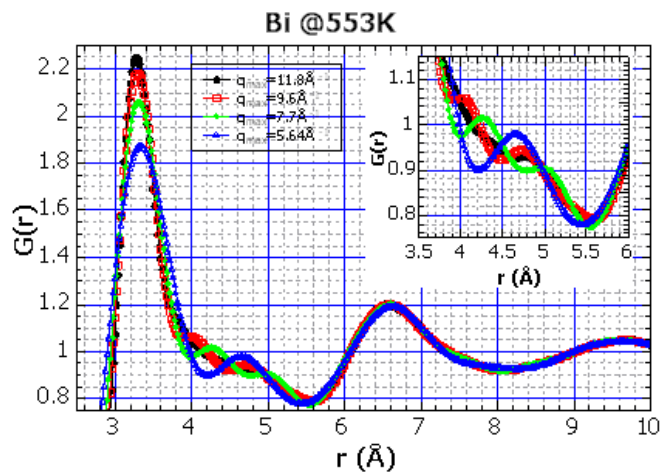


Figure 2: Liquid bismuth RDF as determined from the $S(q)$ measured at 2006 on the 7C2 diffractometer at Saclay. Different curves represent different q_{\max} cut-offs in the $S(q)$ data. All cut-offs were chosen at a positive node, i.e. $S(q_{\max})=1$, and $dS(q=q_{\max})/dq > 0$.

the highest value of “positive-node” q_{\max} in the $S(q)$ data, while keeping significant (factor of 3) signal to noise ratio in the dip (peak) just before (after) this q_{\max} value. The measurement of $S(q)$ up to a q_{\max} value, which is too low, hinders the ability to study the fine details in the calculated RDF. Only through study of liquid structure factors up to large q_{\max} it will be possible to identify the small structural changes occurring in liquids.

References

1. Paalman H H and Pings C J, *J. Appl. Phys.* **33** 2635, 1962
2. Blech I A and Averbach B L, *Phys. Rev.* **137** A1113, 1965
3. Placzek G, *Phys. Rev.* **86** 377, 1952
4. North D M et al., *J. Phys. C* **1** 1075, 1986
5. Greenberg Y et al., *Europhys. Lett.* **86** 36004, 2009
6. Chamberlain O, *Phys. Rev.* **77** 305 1950
7. Sharrah P C and Smith G P, *J. Chem. Phys.* **21** 228, 1953
8. Sharrah P C et al., *J. Chem. Phys.* **32** 241, 1960
9. Khrushchev B I and Bogomolov A M, *Fiz. Metal. Metalloved.* **27** 1011, 1969
10. Dahlborg U and Davidovic M, *Phys. Chem. Liquids* **15** 243, 1986
11. Gudowski W, et al., *J. Non-Cryst. Solid.* **156-158** 130, 1993
12. Greenberg Y, et al., *J. Chem. Phys.* **133** 094506, 2010

Composition and structure of solid solutions in the $\text{Bi}_2\text{O}_3\text{—SiO}_2\text{—V}^{5+}_2\text{O}_5$ system with the structure sillenite

T. MELNIKOVA^A, G. KUZMICHEVA^A, V. RYBAKOV^B, N. BOLOTINA^C & A. COUSSON^D

A Lomonosov State University
of Fine Chemical Technologies,
Moscow, Russia

B Moscow State University,
Moscow, Russia

C Shubnikov Institute of Crys-
tallography, Moscow, Russia

D Laboratoire Léon Brillouin,
CEA-CNRS, CEA Saclay,
91191 Gif-sur-Yvette, France

melti@list.ru

In the $\text{Bi}_2\text{O}_3\text{—SiO}_2\text{—V}^{5+}_2\text{O}_5$ system, single crystal solid solutions of the sillenite family are obtained by a hydrothermal method and characterized by neutron and X-ray diffraction analysis. For the first time, desymmetrization of the structure (a transition from the $I23$ space group into $P23$) is revealed, which is caused by the presence of several atoms in one crystallographic position and also by crystal growth conditions.

The phases $\text{Bi}_{24}\text{M}_2\text{O}_{40}$ or $\text{Bi}_{24}(\text{M},\text{M}')_2\text{O}_{40}$ with sillenite structure ($\gamma\text{-Bi}_2\text{O}_3$, sp.gr. $I23$, $z=13$ or $\text{Bi}(1)_{24}\text{Bi}(2)_2\text{O}_{40-d}$, $z=1$; coordination polyhedra of Bi(1) and Bi(2) are distorted semi-octahedron and tetrahedron, respectively) have physical properties (photoconductivity, piezo- and electrooptical effects and so on) depending on the composition, including the occupancy of each crystallographic position in the structure, which in most cases does not correspond to the nominal composition.

A structural feature of $\text{Bi}_{24}\text{M}_2\text{O}_{40}$ sillenites is two (BiO_3) dimers that are linked by regular (MO_4) tetrahedra with the same (BiO_3) dimers forming a closed group [1].

Based on the performed analysis of the available structural data [2-5], the conclusion may be drawn about the possible formation of solid solutions of the sillenite family with both defect and defect-free positions M, without and with splitting of the position of the O(3) atom into two positions with the formation of different size tetrahedra, with the appearance of additional positions for incorporated $\text{O}_i(4)$ atoms in the structure.

The purpose of this work is the determination of the composition and the study of the structural features of $\text{Bi}_{24}(\text{Si},\text{V})_2\text{O}_{40}$ solid solutions with the sillenite structure, which have not been investigated yet.

The objects of the study were shapeless green and orange single crystals with a diameter to 7 mm of the initial composition $\text{Bi}_{24}(\text{V}_x\text{Si}_{1-x})_2\text{O}_{40}$, which were obtained by a temperature difference method during hydrothermal synthesis in the form of nodules on $\text{Bi}_{24}\text{Ge}_2\text{O}_{40}$ seed crystals. A neutron diffraction study of green (sample 1) and orange (sample 3) single crystals of the nominal composition $\text{Bi}_{24}(\text{V}_x\text{Si}_{1-x})_2\text{O}_{40}$ with the dimensions of $\sim 3 \times 3 \times 3$ mm was carried out on a four-circle single crystal diffractometer mounted on the 5C2 channel of a hot source

of the Orphee reactor (LLB, France; $\lambda = 0.828$ Å). Measurements of the shapeless green crystal ($\sim 0.2 \times 0.2 \times 0.1$ mm) (sample 2) and the orange crystal (sample 4) rounded in the form of a sphere (diameter ~ 0.2 mm) of a similar composition were performed on an X-ray Xcalibur S diffractometer (Oxford Diffraction) with a two-dimensional CCD detector at room temperature (MoK_α radiation).

The crystal structure of all crystals was refined by the full-matrix LSM in the anisotropic approximation for all atoms with the JANA2000 [6] and SHELXL97 [7] programs, the possibilities of the SHELXL97 program being used to determine the presence of more than two atoms in one position.

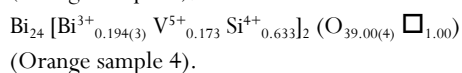
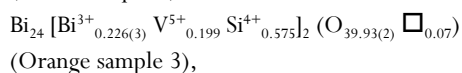
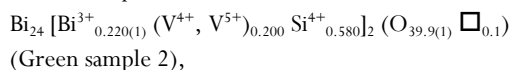
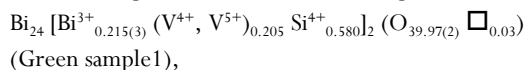
In the refinement of the structure and composition of the studied samples using the SHELXL97, JANA2000 programs the following results were obtained:

Vacancies are absent in the position Bi(1) of all studied phases.

In the refinement of the occupancy of oxygen positions, vacancies were found in the position O(3) in all phases.

The refinement of the structure of all samples with different initial ratios of Si and V atoms in the position M ($\text{Si} = \text{V}$, $\text{Si} > \text{V}$, $\text{Si} < \text{V}$) using the JANA2000 program resulted in the negative values of thermal parameters, which indicates the presence of a heavier atom (which can be only the Bi atom) in this position. The subsequent refinement with the SHELXL97 program of the occupancy of the position M with a different initial ratio of three atoms (Bi, V, Si) at fixed thermal parameters of this position and also the subsequent combined refinement of thermal parameters and the occupancy of this position resulted in the correct values of isotropic thermal parameter.

The results of the refinement of the occupancy of all positions, thermal parameters, and interatomic distances agree with the literature data [1, 3, 4]. The weighted average values calculated by VBM of the formal charge of atoms in the position M, sample color (green and orange due to V^{4+} / V^{5+} ions respectively), the fulfillment of the condition of electric neutrality, the minimum value of R -factors allow us to write the compositions of the studied samples in the form.

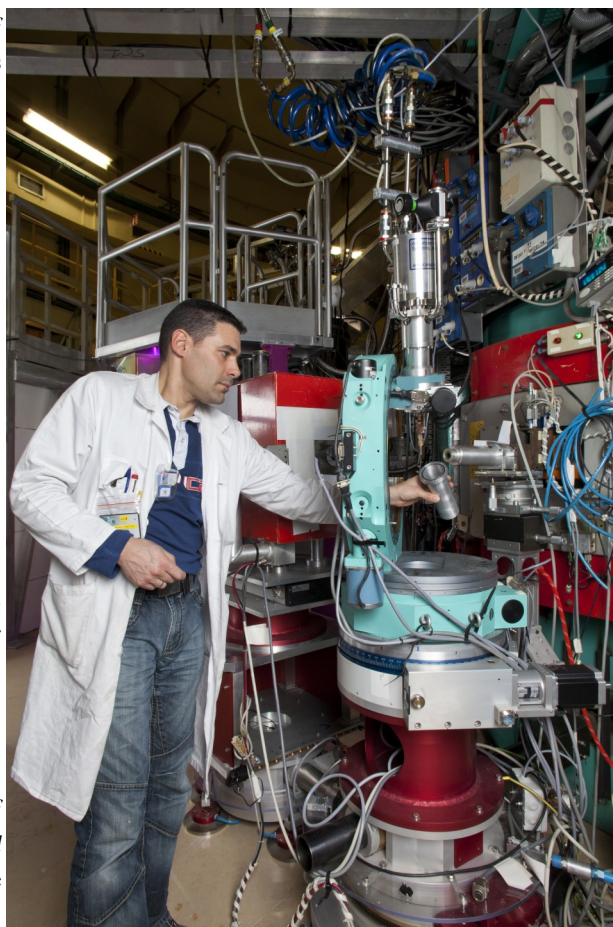


We have analyzed the causes of the appearance of additional electron (nuclear) density peaks with 0.50—0.92 $e/\text{\AA}^3$, which could be taken as the coordinates of the incorporated oxygen atoms (1/2 0 0):

— the initial model of the structure is incorrectly selected for the subsequent refinement (occupancy of the position M only by Si and V atoms, *i.e.* the absence of some number of Bi atoms in this position; incorrectly selected enantiomorphous form),

— absorption is incorrectly taken into account.

An analysis of all diffraction reflections made it possible to reveal for samples 1 and 3 some number of reflections of the hkl form with $h + k + l \neq 2n$, $0kl$ with $k + l \neq 2n$, hhl with $l \neq 2n$, $h00$ with $h \neq 2n$, which cannot be indexed in the $P23$ space group. Nothing similar was found for samples 2 and 4. This phenomenon (the kinetic (growth) phase transition of the order—disorder type we first discovered for the phases with the sillenite structure in the $\text{Bi}_2\text{O}_3\text{—SiO}_2\text{—Mn}^{4+}$ system [8], and now for the phases in the $\text{Bi}_2\text{O}_3\text{—SiO}_2\text{—V}_2^{5+}\text{—O}_5$ system. Polymorphism observed in sillenites is due to both crystal chemical factors (the presence in the structure of positions that are jointly occupied by several atoms different in size, formal charge, electronegativity) and preparation conditions (crystallization under hydrothermal conditions close to equilibrium at a temperature below 400 °C).



Mounting a shield on 5C2 close-cycle cryostat.

References

1. S.F. Radaev, V.I. Simonov, *Kristallografiya*, 1992, 37, p. 914.
2. S.C. Abrahams, J.L. Bernstein, C. Svensson, *J. Chem. Phys.*, 1979, 71(2), P. 788.
3. A.N. Yudin, E.A. Pobedinskaya, L.E. Terent'eva et al., *Neorgan. Mater.*, 1989., 25, N 10, p. 1715.
4. J.L. Soubeyroux, M. Devalette, N. Khachani et al., *J. Solide State Chem.*, 1990., 86., P. 59.
5. T.I. Mel'nikova, G.M. Kuz'micheva, N.B. Bolotina et al., *Proc. of the 2nd Conference-Workshop for Young Scientists [in Russian]*, Chernogolovka, 2010, 1.
6. M. Dusek, V. Petricek, M. Wunschel et al., *J. Appl. Crystallogr.*, 2001, 34, P. 398.
7. G.M. Sheldrick, *Acta Crystallogr.*, 2008, A64, P. 112.
8. T.I. Mel'nikova, G.M. Kuz'micheva, V.B. Rybakov et al., *Kristallografiya*, 2010, 55, N 2, p. 229.

Synthesis and structure determination of the high temperature form of La_2WO_6

M. ALLIX^A, M.H. CHAMBRIER^B, E. VÉRON^A, F. PORCHER^C, M. SUCHOMEL^D & F. GOUTENOIRE^B

A CEMHTI, Orleans, France

B LdOF, Le Mans, France

C Laboratoire Léon Brillouin, CEA-CNRS, CEA Saclay, 91191 Gif-sur-Yvette, France

D APS, Argonne, USA

mathieu.allix@cnrs-orleans.fr

*This work, published as an article in *Crystal Growth and Design*[1], presents the synthesis, the structure determination and the structure analysis of the La_2WO_6 high temperature phase, namely $\alpha\text{-La}_2\text{WO}_6$. The structure has been determined ab initio from room temperature electron diffraction coupled to synchrotron and neutron powder diffraction refinements using the charge flipping algorithm. $\alpha\text{-La}_2\text{WO}_6$ crystallizes in the $Pm2_1n$ ($n^\circ 31$) orthorhombic space group, with $Z = 6$, and has the following cell parameters: $a = 16.5513(1)\text{Å}$, $b = 5.52003(3)\text{Å}$, $c = 8.88326(3)\text{Å}$. The structure, which consists of regular paving between six $[\text{WO}_6]$ octahedra alternating with twelve isolated lanthanum atoms, has been compared to the $\beta\text{-La}_2\text{WO}_6$ [2] low temperature polymorph.*

Oxides from the $\text{Ln}_2\text{O}_3\text{-MO}_3$ ($M = \text{Mo}$ and W) systems are currently studied for their laser host application, ionic conduction, catalytic and ferroelectric properties. In situ high-temperature laboratory XRD study was performed up to 1600°C (Fig. 1)

The first diffraction peaks of the alpha polymorph appeared at 1490°C , in good agreement with the DSC measurements. Both forms then coexist up to 1540°C . At this temperature, the reflections attributed to the $\beta\text{-La}_2\text{WO}_6$ completely disappeared, indicating that the phase transition was complete. In order to determine the structure of the high temperature form, we have then attempted to stabilize the $\alpha\text{-La}_2\text{WO}_6$ form at room temperature by quenching the sample from high temperature.

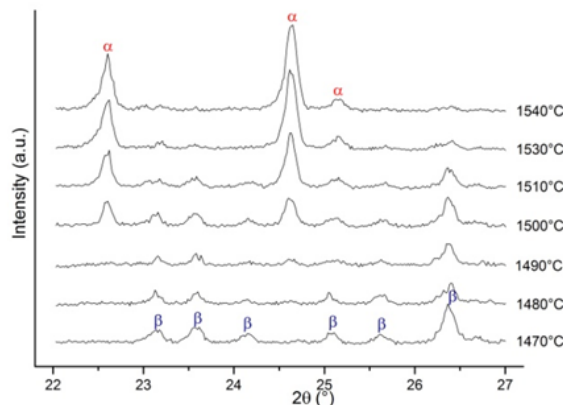


Figure 1 : In-situ X-ray diffractograms recorded versus temperature starting from the $\beta\text{-La}_2\text{WO}_6$. The α polymorph appears at 1490°C and the β phase remains up to 1540°C .

A small amount of the $\beta\text{-La}_2\text{WO}_6$ phase was then heated up to 1600°C for 15 minutes in a large plati-

num crucible allowing to have only a thin layer of sample covering its bottom. The crucible was next rapidly quenched in water. X-ray diffraction of the obtained sample showed pure $\alpha\text{-La}_2\text{WO}_6$ phase. Cell indexation has been performed by electron diffraction analysis (Fig. 2) on several crystallites resulting

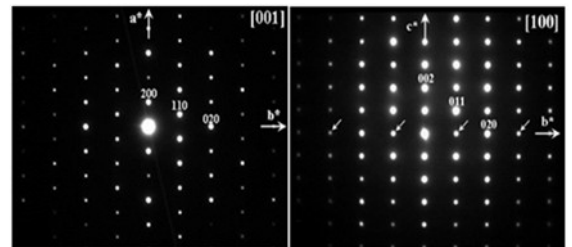


Figure 2 : Electron diffraction patterns of $\alpha\text{-La}_2\text{WO}_6$ phase recorded along the $[001]$ and $[100]$ directions.

from the quenched sample.

The reconstruction of the reciprocal space evidences an orthorhombic cell with $a \approx 17 \text{Å}$; $b \approx 5.6 \text{Å}$ and $c \approx 9 \text{Å}$. No condition limiting the general hkl reflections was observed during the reciprocal lattice reconstruction, leading to the assignment of a primitive lattice. The only extra condition $hk0: h+k=2n$ due to the presence of a n glide along c restricts the choice to one of the 3 following space groups: $Pmmn$; $P2_1mn$ and $Pm2_1n$. The synchrotron data, the cell parameters and the different space groups have been introduced in the Jana software[3] equipped with the Superflip program[4]. The charge flipping algorithm found easily a solution and led us to close cationic models for the three possible space groups. Six cationic positions were indeed identified, three of them on a $2a$ Wyckoff site and the other three on $4b$ sites. At this stage, their assignation remained rather difficult without having pushed forward the elucidation.

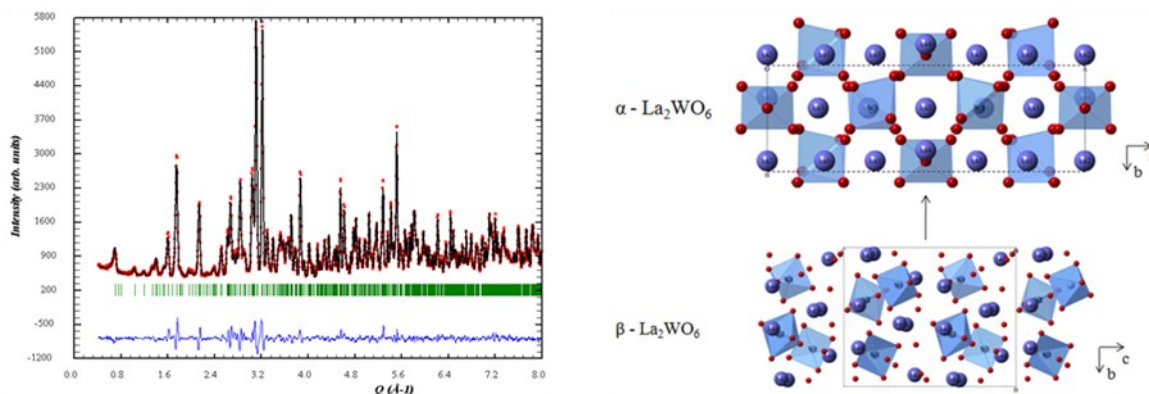
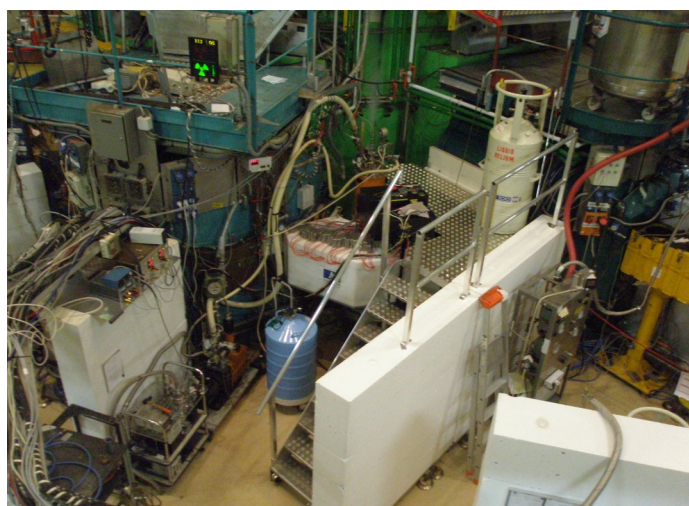


Figure 3 : (Left) refined diffraction patterns from neutron data (3T2 diffractometer, LLB). (Right) Crystal structures of the β and α - La_2WO_6 polymorphs.

However, the most symmetric $Pmmn$ space group turned out to be unable to model any distortion, resulting in huge thermal factors, especially along b when using anisotropic factors. On the other hand, the $Pm2_1n$ model could fit easily the structure and especially these distortions, with correct reliability factors and acceptable thermal parameters. Once the cations were positioned within the cell, some of the most obvious oxygen positions were then localized thanks to Fourier difference maps. At this point, the assignation of La and W species to the cationic positions became feasible thanks to the differentiation between the La-O and W-O bond length values, respectively typically within the 2.4-2.6Å and 1.7-2.0Å ranges. In order to complete this model with the missing oxygen positions and to obtain more reliable thermal parameters, we have then recorded neutron powder diffraction data. The incomplete structural model determined previously by powder synchrotron data refinement was used as a starting model. The remaining oxygen positions appeared then clearly using Fourier difference maps. Finally, a mixed refinement has equally been undertaken from both synchrotron and neutron diffraction patterns using absorption correction.

Both tungsten atomic positions present usual distorted octahedral environment. The whole structure can thus be described as six $[\text{WO}_6]$ octahedra units

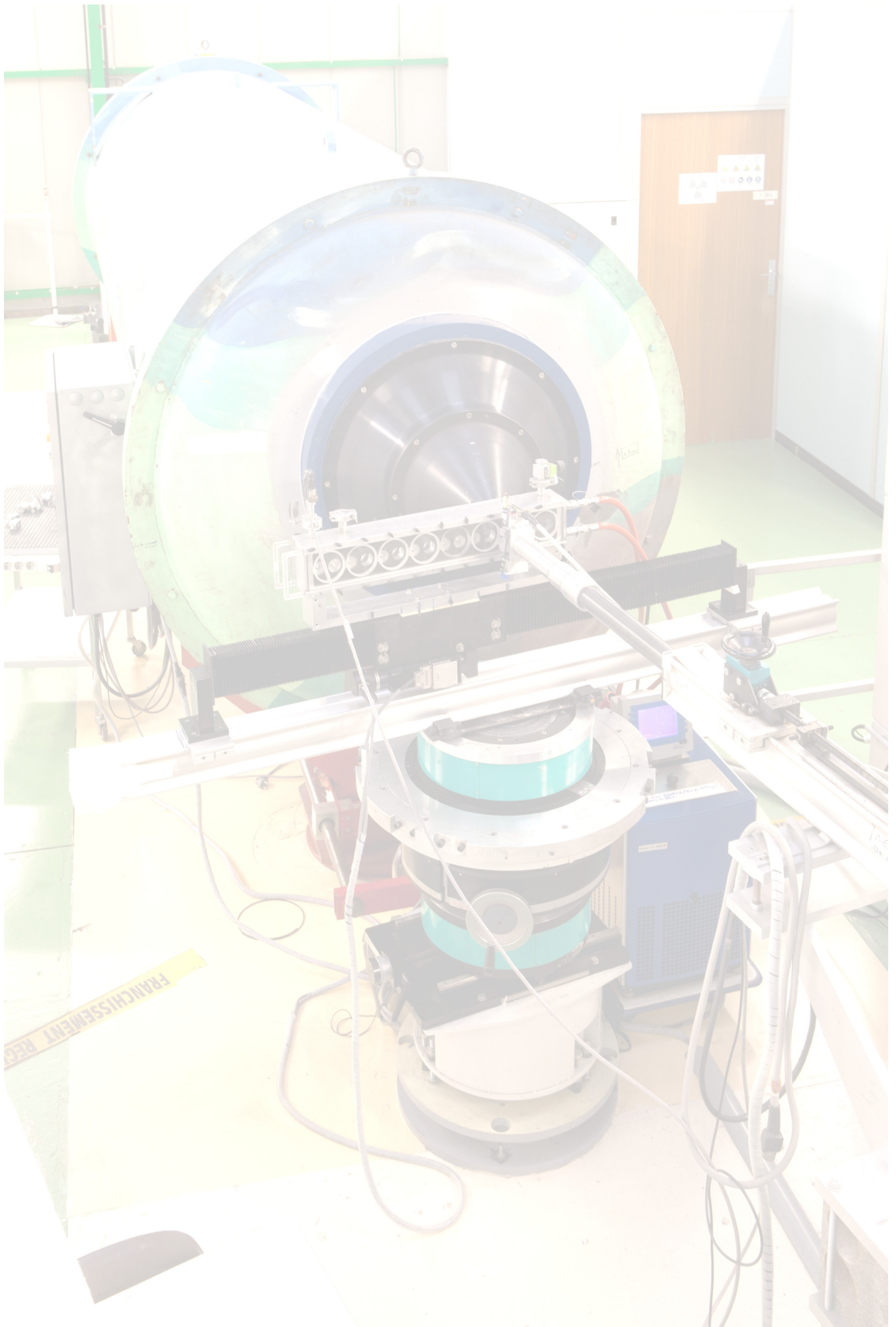
alternating with 12 isolated lanthanum atoms. These lanthanum atoms are surrounded by 7 to 9 oxygen atoms, forming large polyhedra. The A_2BX_6 structure could be described as an ordered Fluorine structure: $3x\text{CaF}_2 = A_2BX_6$ entity. An ionic conductivity was performed by complex impedance spectroscopy. The Arrhenius plot of the α - La_2WO_6 exhibit a remarkable variation of the conductivity versus temperature. Between 480°C and 620°C, a linear evolution of the conductivity is observed. At 640°, the plot show a drastic decrease which can be linked to the $\alpha \rightarrow \beta$ La_2WO_6 phase transition. One can notice that α - La_2WO_6 is more conducting than β - La_2WO_6 within one order of magnitude and reach a conductivity value of 5.5×10^{-4} S/cm at 620°C.



The High-resolution thermal diffractometer 3T2

References

1. Allix, M.; Chambrier, M. H.; Veron, E.; Porcher, F.; Suchomel, M.; Goutenoire, F. *Crystal Growth & Design* 2011, 11, 5105.
2. Chambrier, M. H.; Kodjikian, S.; Ibberson, R. M.; Goutenoire, F. *Journal of Solid State Chemistry* 2009, 182, 209.
3. Petricek, V., Dusek, M. & Palatinus, L, 2006.
4. Palatinus, L.; Chapuis, G. J. *Appl. Crystallogr.* 2007, 40, 786.



AXE 3: SOFT MATTER AND BIOPHYSICS.

The third scientific axis concerns soft matter and biophysics. Flourishing of many new systems, combining different components, many involving nanoscales (1-100 nm) has become a major current trend in soft matter. At LLB, researchers have developed in similar directions keeping some of the historical specificities of the lab: involving polymers is one of the components illustrating the advantages of neutron scattering, *i.e.* labelling and contrast matching, while we often marry the reciprocal space (SANS but also SAXS) with other techniques, in real space or at macroscopic scales. The following topics are investigated: nanoparticles and hybrid systems; organic systems and self-organization; polymer dynamics; electrostatics complexes. The research at the interface of physics and biology is based on three main topics: 1) Proteins in complex media viewed as model systems for living environments. Experiments are concerned with macro- or supra-molecular scales and their analysis is strongly influenced by our background in polymer physics, statistical physics and phase transition physics; 2) Local dynamics of proteins and hydration water in relation with the dynamical transition of proteins and their enzymatic activity. Neutron scattering techniques, that are very sensitive to protons, are particularly suitable for these studies; 3) Water and its specific properties are fundamentally related to life and to the very peculiar properties of some biological molecules like proteins. Here, water properties are studied in relation with the dynamics of hydrogen bonds network, the notions of hydrophobicity and confinement.

- 1) **FOAM LASTING FOREVER AND COLLAPSE AT WILL!**
F. Cousin, J.-P. Douliez, A.-L. Fameau
- 2) **PACKING OF SYNTHETIC POLYELECTROLYTES IN VIRAL CAPSIDS**
Tatoua, M.; Le Coeura,b, C., Tresseta,*, G., Zeghala, M.
- 3) **DOXORUBICIN LOADED MAGNETIC POLYMERSOMES: THERANOSTIC NANOCARRIERS FOR MR IMAGING AND MAGNETO-CHEMOTHERAPY**
C. Sanson, O. Diou, J. Thévenot, E. Ibarboure, A. Soum, A. Brûlet, S. Miraux, E. Thiaudière, S. Tan, A. Brisson, V. Dupuis, O. Sandre & S. Lecommandoux
- 4) **SUPRAMOLECULAR ASSEMBLIES OF PLURONICS AND β -CYCLODEXTRINS: FROM MICELLES TO SELF-ASSEMBLED CRYSTALLINE NANO-PLATELETS**
G. Schlatter, C. Perry, P. Hébraud, P. Lindner, A. Lapp
- 5) **INVESTIGATION OF POLYMER HYDROGELS WITH MEMORY EFFECT, FOR CEFAZOLINE IMMOBILIZATION, BY SMALL-ANGLE NEUTRON SCATTERING**
Y.U.V. Kulvelis, V.T Lebedev, V.A. Trunov, S.S. Ivanchev, O.N. Primachenko, S.Y.A. Khaikin, V.N. Pavlyuchenko, J. Teixeira, S. Combet
- 6) **WALL THICKNESS DETERMINATION OF HYDROPHOBICALLY FUNCTIONALIZED MCM-41 MATERIALS**
M. Schoeffel, N. Brodie-Linder, F. Audonnet, C. Alba-Simionesco

Foam lasting forever and collapse at will!

E. COUSIN^A, J.-P. DOULIEZ^B & A.-L. FAMEAU^A

A Laboratoire Léon Brillouin,
CEA-CNRS, CEA Saclay,
91191 Gif-sur-Yvette, France

B INRA/Biopolymères Interactions Assemblages (BIA)/
Interfaces et systèmes dispersés (ISD) Angers-Nantes, BP
71627, 44316 Nantes

fabrice.cousin@cea.fr

*Soapy solutions that foam, this is not extraordinary; a soap foam stable for several months even at 60 ° C, it is more, and especially if the foam is produced by "green chemistry" from a natural substance. Finally, the foam can be destroyed quickly by simply changing its temperature and this, reversibly. In summary, it is the work carried out by teams from INRA, CNRS and CEA, which opens up new applications of interest to manufacturers of cosmetics or detergents. The results of this research are published in the journal *Angewandte Chemie*, 29 August.*

Because of their particular texture and their constituent molecules, foams often have detergent properties. The molecules that are essential to disperse in water to make foam are called "surfactants". They migrate spontaneously at the water-air interface, which helps stabilize the thin water films around air bubbles in the foam, according to a specific architecture. Because of their properties, foams have many applications in areas such as cleaning, decontamination, cosmetics, fight against pollution and fires, food, or extraction of natural resources.

Researchers at INRA, CEA and CNRS have studied here a special surfactant molecule, the 12-hydroxy stearic fatty acid extracted from castor oil. To disperse the molecule initially insoluble in water, they have added salt. They then demonstrated the

very advantageous properties of the surfactant: even in small amounts, it produces abundant foam and above all stable for more than 6 months (Fig. 1), unlike conventional surfactants that stabilize foam a few hours only. The researchers observed and explained this phenomenon using microscopy and neutron scattering, to monitor *in situ* the evolution of the structure at the nanoscale.

Thus, they showed that in a range of temperatures between 20 and 60 ° C, the 12-hydroxy stearic acid fatty acid, mixed with the "good" salt is dispersed in water in the form of tubes of a few microns. These tubes then form a perfectly stable and rigid structure in thin films of water placed between the air bubbles which explains the stability of the foam.

Beyond 60 ° C, the tubes are divided into spherical assemblies thousand times smaller (few nanometers), called "micelles". The previously stable foam then collapses because the rigid structure disappears. Researchers have shown that this transition from an assembly of tubes in an assembly of micelles is "reversible." Indeed, if one increases the temperature of a foam, its volume will decrease due the formation of micelles, and if one lowers the temperature between 20 and 60 ° C, the tubes re-form and the foam is stabilized again (to recover the initial volume of foam, one would still have to inject air, see Fig. 2.

The formation of stable foam with a surfactant molecule as simple and natural is a first. The transition temperature between the state where the foam contains tubes, and the state "micelles", depends on the salt chosen to disperse the molecule into the water, increasing its potential use.

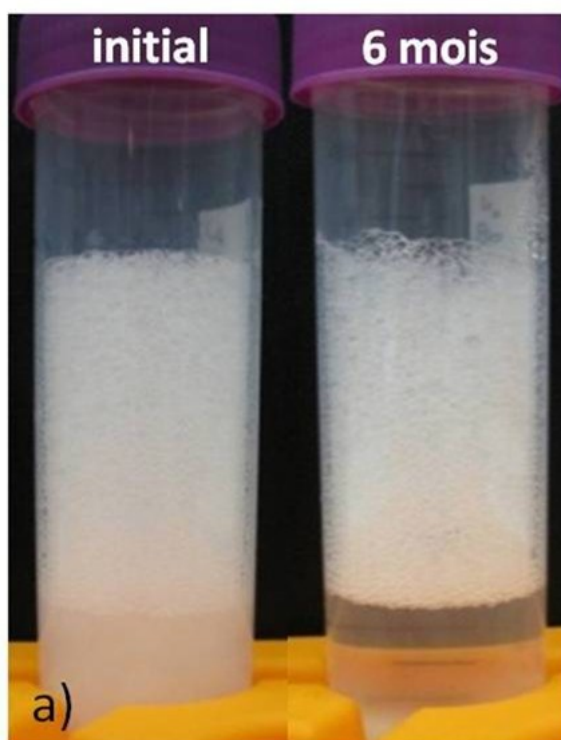
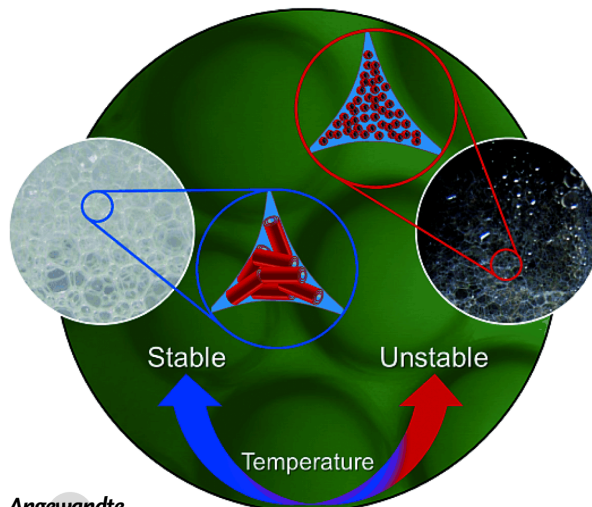
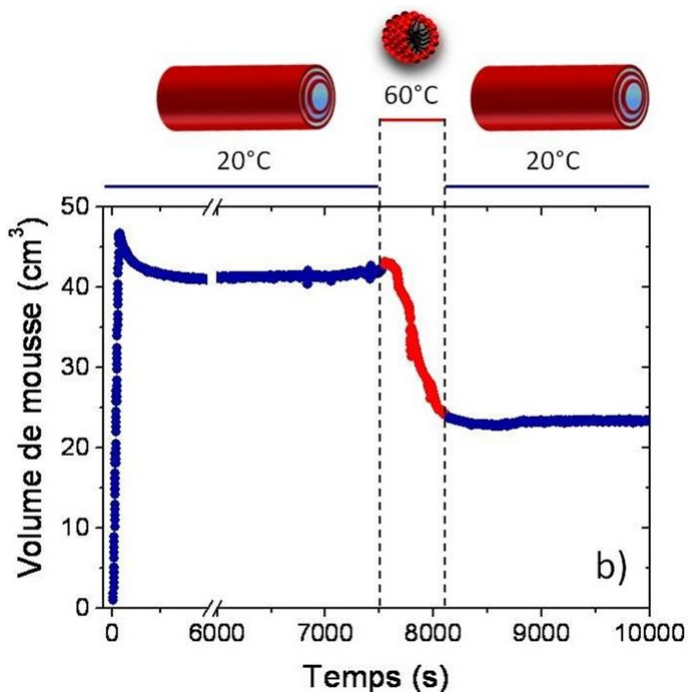


Figure 1: A stable foam over 6 months! (at room temperature)

This green chemistry, since it comes from a bio-molecule, opens up interesting prospects for foams widely used in industry. It would be possible to produce such detergents or shampoos which can control the amount of foam by simple effect of temperature and thus facilitate their evacuation.

Some cosmetics require many elements to obtain stable foam, the use of the 12-hydroxy stearic fatty acid would limit the amount of synthetic elements while retaining the properties "foaming" longer.



Angewandte

Figure 3 : Structure locales des formes superstables et instables des mousses.

Figure 2 : Time evolution of foam volume, combined with a temporary rise in



The Small-Angle spectrometer PAXY

References

1. A.-L. Fameau, A. Saint-Jalmes, F. Cousin, B.Houinsou-Houssou, B. Novales, L. Navailles, F. Nallet, C. Gaillard, F. Boué, J.-P. Douliéz*, *Angewandte Chemie* 123(36) (2011) 8414.

Packing of synthetic polyelectrolytes in viral capsids

TATOU^A, M.; LE COEUR^{A,B}, C., TRESSET^{A*}, G., ZEGHAL^A, M.

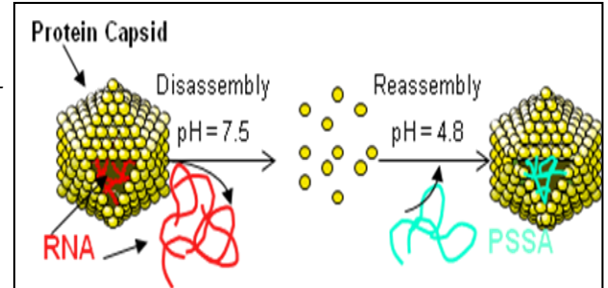
a Laboratoire de Physique des Solides, Orsay, France

b Institut de Chimie et des Matériaux Paris-Est, Thiais, France

*guillaume.tresset@u-psud.fr

Viruses are natural examples of “nanomachines” combining remarkable structural and functional properties which should inspire the design of artificial systems. Virus-based nanotechnology takes advantage of the natural circulatory and targeting properties of viruses in order to design therapeutics and vaccines that specially target tissues of interest in vivo. Viruses can act as nanocontainers and encapsulate synthetic materials for delivery applications. The conformation of encapsulated genome, the self-assembly mechanisms of protein capsid and the interactions between capsid and packed polyelectrolyte are

still unclear. The aim of our project is to identify parameters governing the encapsulation and control them. To do so, we study the packing of synthetic polyelectrolytes into viral capsids devoid of genome.



The mechanisms of genome packing, the interactions between capsid proteins and nucleic acids, and the conditions to obtain properly formed objects are still largely unknown and debated. The aim of this work is to study the conformational changes of a synthetic polyelectrolyte with different masses upon encapsulation into a viral shell. We used the capsid proteins of cowpea chlorotic mottle virus (CCMV), a self-assembled icosahedral virus, which has a multipartite genome consisting of four genes spread out over three different RNA molecules. The RNAs are packaged in identical $T = 3$ capsids of 180 proteins, capable of encapsulating poly(styrene sulfonic acid) (PSSA) [1].

To compare the behavior of PSSA to that of RNA, we measured first at the Institut Laue Langevin (D22 beamline), the scattering pattern of RNA and capsid together in a buffer containing 100% D_2O . Small angle neutron scattering provides us with information about shape and size, as well as the internal structure of the assembly, *i.e.* the space occupied by the RNA and the thickness of the protein capsid. The intensity curve shown in Fig. 1 can be fitted by a multi core shell model. Fitting parameters obtained from SansView with a model of two shells are: hollow core radius = 60 Å, thickness of RNA = 42 Å, thickness of proteins = 35 Å with a polydispersity of 10%. This model revealed the existence of a hollow core in the virus.

After verification by transmission electron microscopy (TEM) of the encapsulation of the PSSA into CCMV capsid (devoid of genome), we studied size changes of CCMV capsids induced by the presence of PSSA of different masses. Using small angle neutron scattering at LLB (PACE beamline) and contrast variation method, we matched the signal of deuterated PSSA with a solvent containing 100% D_2O , and we measured only the contribution of the capsid protein. In Fig. 2 we compare the scattering intensity curves of an empty capsid and capsids encapsulating PSSA (600 kDa and 8 kDa), with a ratio of protein/PSS= 2/1.

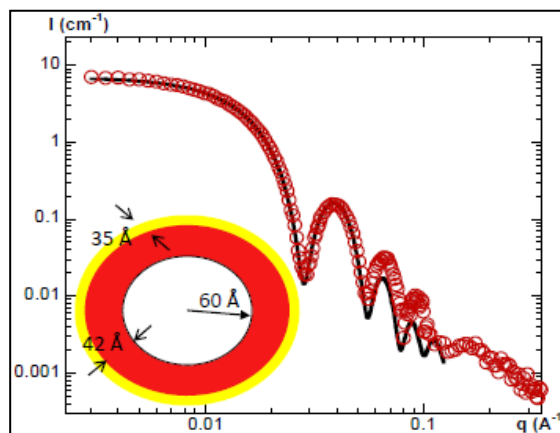


Fig. 1: SANS scattering curves of native CCMV virus. Buffer solution is 100% D_2O and 1M NaCl. The black line represents the fit of a multi core shell model.

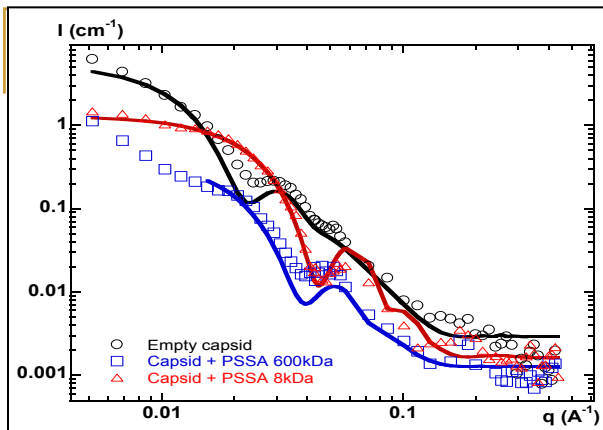


Figure 2: PSSA-D is matched with 100% D₂O, the scattered intensities arise solely from protein capsids. pD = 4.8 and 1M NaCl.

We observe that the first oscillations from the curves of filled capsids are shifted to the large angles compared to empty capsid. Curves were fitted by a core shell model. The thickness of the shell was fixed to 35 Å, namely the thickness of the virus shell. Fitting parameters are in Table 1.

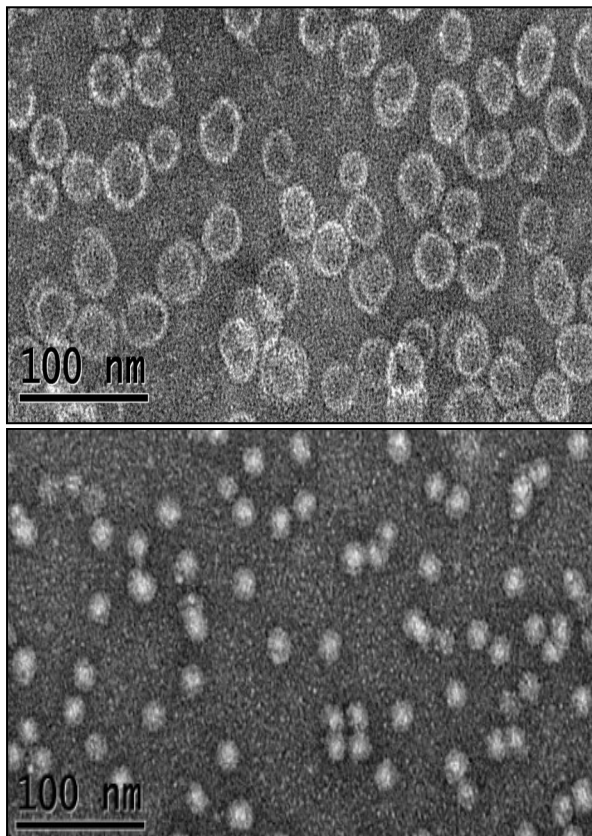


Figure 2: TEM image obtained with negative staining of empty capsids in the top and 8kDa PS

Table.1

	Core radius (Å)	Polydispersity
Capsid	110	23%
Capsid + PSSA (600 kDa)	56	25%
Capsid + PSSA (8 kDa)	49	15%

The capsids are flexible: they adjust their size and become smaller when containing PSSA. The results show that the core radius increases slightly with PSSA mass. The size shrinking of filled capsids was confirmed by TEM observations (see Fig.3).

To verify if the amount of filled PSSA may have an influence on the structure of capsids, we varied the ratio of protein/PSSA in the assembly. We compared assemblies involving 8kDa PSSA at ratio of 2/1 and 4/1. The results are shown in the Fig. 4. The first oscillation is in the same position for both curves. Fitting parameters for 4/1 ratio are: core radius = 46 Å with polydispersity of 23%.

They are very close to fitting parameters arising from the ratio 2/1. A ratio of 9/1 was studied by TEM and showed a similar diameter. Those results show that up to a ratio of 2/1, capsids keep the same diameter..

This work is completed by time-resolved X-ray experiment at the ESRF (ID02 beamline) which allowed us to elucidate the kinetics of self-assembling capsid proteins either alone or with a core material [2].

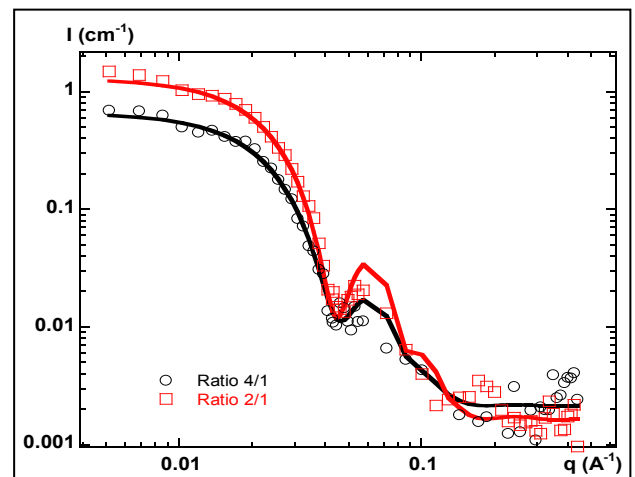


Figure 4: Scattered intensities from assemblies of protein/PSSA ratio of 2/1 and 4/1, PSSA-D is matched with 100% D₂O.

References

- 1.1 Hu, Y. and al, *Biophys. J.* 94 (2008), 1428
- 2.2 Tatou, M. et al, in preparation (2012)

Doxorubicin Loaded Magnetic Polymersomes: Theranostic Nanocarriers for MR Imaging and Magneto-Chemotherapy

C. SANSON^A, O. DIOU^A, J. THÉVENOT^A, E. IBARBOURE^A, A. SOUM^A, A. BRÛLET^B, S. MIRAUX^C, E. THIAUDIÈRE^C, S. TAN^D, A. BRISSON^D, V. DUPUIS^E, O. SANDRE^A & S. LECOMMANDOUX^A

A LCPO UMR5629 Univ Bordeaux / CNRS / IPB,

B RMSB UMR5536 Univ Bordeaux / CNRS,

C Laboratoire Léon Brillouin, CEA-CNRS, CEA Saclay, 91191 Gif-sur-Yvette, France,

D CBMN UMR5248 Univ Bordeaux / CNRS / IPB

E PECSA UMR7195 UPMC Paris 6 / CNRS

olivier.sandre@ipb.fr

lecommandoux@enscbp.fr

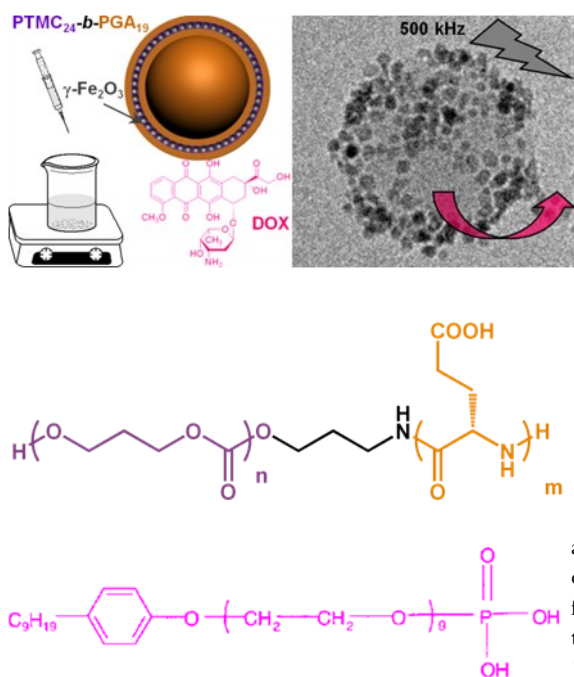


Figure 1: Dually-loaded vesicles prepared by addition at controlled speed of an aqueous buffer into a mixture in DMSO of PTMC-b-PGA ($m=19$ and $n=24$), doxorubicin and magnetic nanoparticles coated by the BEY surfactant of given formula (bottom sketch). The cryo-TEM image (top right panel) shows a vesicle wrapped by a mantle of MNPs, which excitation by a RF magnetic field heats up the membrane locally and accelerates the DOX release.

Hydrophobically modified magnetic nanoparticles (MNPs) were encapsulated within the membrane of poly(trimethylene carbonate)-*b*-poly(L-glutamic acid) (PTMC-*b*-PGA) block copolymer vesicles using a nanoprecipitation process. This formulation method provides a high loading of MNPs (up to 70 wt %) together with a good control over the sizes of the vesicles (100 – 400 nm). The deformation of the vesicle membrane under an applied magnetic field was evidenced by anisotropic SANS. These hybrid objects display con-

trast enhancement properties in Magnetic Resonance Imaging, a diagnostic method routinely used for three-dimensional and non-invasive scans of the human body.[1] They can also be guided in a magnetic field gradient. The feasibility of drug release triggered by magnetic induction was evidenced using the anticancer drug doxorubicin (DOX), which is co-encapsulated in the membrane. Magnetic polymersomes are thus proposed as multimodal drug nanocarriers for bio-imaging and magneto-chemotherapy.

In the new field of nanomedicine, a great variety of polymeric drug delivery nanocarriers have shown efficient entrapment and controlled release of drugs *in vitro*. However, evaluating the fate of the carrier after injection *in vivo* is a delicate task: as a consequence, an imaging probe is usually co-encapsulated with the drugs in the polymer nanoparticles. Such multifunctional nanocarriers

for cancer diagnostics and treatment open the field of “theranostics”, *i.e.* combination of imaging and therapeutic functions in “all-in-one” nanoparticles.[2] Among the different nanoparticles used in biotechnological applications, superparamagnetic nanocrystals made of $\gamma\text{-Fe}_2\text{O}_3$ around 10 nm in size are of particular interest since they are biocompatible and offer contrast enhancement in MRI. In addition, MNPs can also be implemented to induce cancer cells apoptosis. Local heating is obtained by exposure to radio-frequency magnetic fields in the frequency range 100 kHz – 1MHz, due to thermal dissipation by the magnetic moments forced to oscillate at the frequency of the applied magnetic field. Hyperthermia therapy (*i.e.* treating by heat) has been recognized as a promising form of cancer therapy, particularly in synergy with chemo- or radio-therapy.[3] For a solid tumor located not

too deep under the skin (such as melanoma), a conventional hyperthermia treatment is applied, the cancer cells being destroyed by the heat shock. We proposed a totally different strategy with a polymer vesicle delivering a drug through the temperature increase induced by radiofrequency magnetic fields not macroscopically but locally, at the scale of the membrane: the MNPs being confined inside the polymer block, the heat dissipates in the vicinity of the polymer membrane, which strongly impacts its permeability. Therefore we called this strategy “magneto-chemotherapy” as depicted on Fig. 1.[4]

In this highlight paper, we describe a convenient way to prepare fully biodegradable polymersomes featuring a dual magnetic and thermo-responsive membrane. The hydrophobic core of membranes is made of the PTMC semi-crystalline blocks and the hydrophilic leaflets arise from the PGA polypeptide blocks of the copolymer. One pot nanoprecipitation (Fig. 1) leads to dual-loaded vesicles with iron oxide MNPs of appropriate size and coating (BEY) embedded within the membranes together with the antitumor drug doxorubicin. The amphiphilic diblock copolymer was synthesized by ring-opening polymerization of γ -benzyl-L-glutamate *N*-carboxyanhydride initiated by amino functionalized PTMC macroinitiator upon a previously published method.[5] PTMC₂₄-*b*-PGA₁₉ presents a hydrophilic weight fraction of 50 wt % for an overall molar mass $M_n = 4900$ g/mol with a dispersity index 1.15. On the other hand, magnetic iron oxides MNPs were synthesized in water by alkaline co-precipitation of ferrous and ferric salts followed by coating with a surfactant called Beycostat (bottom sketch on Fig. 1). The gyration and hydrodynamic radii of these MNPs were respectively $R_G^{\text{MNP}} = 3.05 \pm 0.06$

nm and $R_H^{\text{MNP}} = 4.70 \pm 0.07$ nm as measured by SANS and DLS.

Table 1 : Characteristics of nanoprecipitations

Addition time	MNP LC	DOX LC	R_H (nm)	PDI	ζ (mV)
15 min	35 %	0 %	152	0.15	-39.6
		12 %	124	0.23	-39.3
10 sec	50 %	0 %	56.5	0.22	-40.8
		9 %	61	0.15	-42.0

Nanoprecipitation allowed reaching quantitative loading contents (LC) with controlled final sizes and low polydispersity indexes, as reported on this table for two durations of the buffer addition (PBS pH = 7.4), with and without DOX.

The two-dimensional confinement of the MNPs inside the vesicular membranes was evidenced by small angle neutron and light scattering techniques and observed by transmission electron microscopy. The magnetic membranes exhibited a reversible deformation under a permanent magnetic field of moderate intensity (0.1 Tesla) as seen on Fig. 2.

deformation of the vesicle into an elongated ellipsoid. The apparent increase of thickness near the equator and concomitant decrease near the magnetic poles ($\delta^\perp = 18$ nm, $\delta^\parallel = 8$ nm at $B = 0.6$ T) indicates that MNPs move away from the poles where dipolar repulsions are strong and accumulate in the other portions of membrane where dipolar interactions are expected to be attractive

Finally, the release of the anticancer drug was assayed under several heating conditions. A global heating at 37°C (melting temperature of PTMC⁶) caused a significantly higher release than the one observed at 23°C , as explained by a more permeable membrane. But the application of an oscillating magnetic field at 23°C induced hyperthermia at a local (nanometric) scale only in the vicinity of the membrane

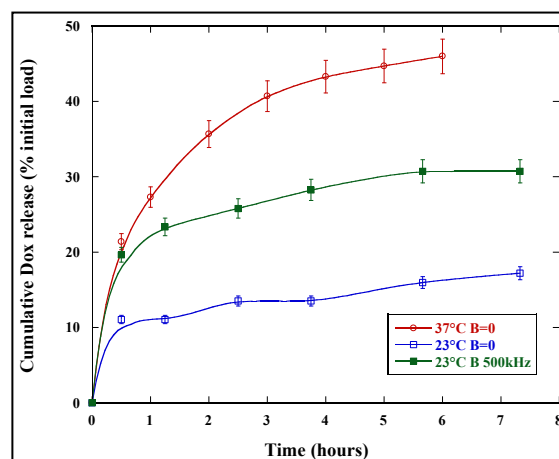


Fig. 3: In vitro release assays of doxorubicin at two temperatures (23 or 37°C) and with or without an applied radio-frequency magnetic field $B=2.65$ mT at 500 kHz.

that provoked an increase in DOX release (by 2 times), thereby evidencing the validity of the concept of magneto-chemotherapy with those magnetic polymersomes.

Funding

Financial support was provided by the European Commission (FP7 CP-IP 213631-2 NANOTHER)

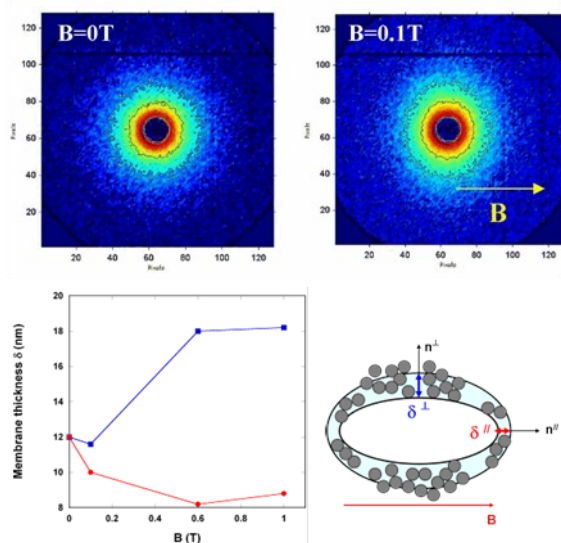


Fig. 2 Top: SANS patterns of magnetic vesicles loaded at 50 wt. % MNPs in H_2O in the q range $3 \times 10^{-3} - 3 \times 10^{-2} \text{ \AA}^{-1}$ at zero field and under $B=0.1$ Tesla. Colors correspond to iso-intensity ranges. Patterns were averaged in angular sectors (-30° 30°) along the field direction or (-15° 15°) around the perpendicular direction. Bottom: Kratky-Porod fits $\text{Ln}[q^2 I(q)] \sim -q^2 \delta^2 / 12$ in the low q regime lead to membrane thicknesses in the two directions d^\parallel and d^\perp and to a scheme of the overall deformation..

With pure H_2O as solvent, the nuclear scattering of the inorganic component of membranes was much greater than that of the polymer leaflets. Thus a variation in intensity in both directions can be ascribed to a reorganization of the

MNPs within the membrane. The variation of δ^\parallel and δ^\perp as a function of the field intensity is interpreted by the stretching of the membrane near the magnetic poles due to an overall

References

1. S. Laurent, D. Forge, M. Port, A. Roch, C. Robic, L. Vander Elst, R. N. Muller, *Chem. Rev.* **2008**, *108*, 2064.
2. Z-R. Lu, F. Ye, A. Vaidya, J. Contr. Rel. **2007**, *122*, 269; P. Kyeongsoon et al., *Adv. Func. Mat.* **2009**, *19*, 1553.
3. S. E. Barry, *Int. J. Hyperthermia* **2008**, *24*, 45.
4. C. Sanson, O. Diou, J. Thévenot, E. Ibarboure, A. Soum, A. Brûlet, S. Miraux, E. Thiaudière, S. Tan, A. Brisson, V. Dupuis, O. Sandre, S. Lecommandoux, *ACS Nano* **2011**, *5*, 1122.
5. C. Sanson, C. Schatz, J-F. Le Meins, A. Brûlet, A. Soum, S. Lecommandoux, *Langmuir* **2010**, *26*, 2751.
6. C. Sanson, J-F. Le Meins, C. Schatz, A. Soum, S. Lecommandoux, *Soft Matter* **2010**, *6*, 1722.

Supramolecular assemblies of pluronics and β -cyclodextrins: from micelles to self-assembled crystalline nano-platelets

G. SCHLATTER^A, C. PERRY^A, P. HÉBRAUD^B, P. LINDNER^C & A. LAPP^D

A LiPHT, EA4379
Ecole Européenne de Chimie,
Polymères et Matériaux,
Université de Strasbourg,
67087 Strasbourg Cedex 2,
France.

B IPCMS, CNRS - UMR 7504,
Université de Strasbourg,
67034 Strasbourg Cedex 2,
France.

C ILL, CEA Grenoble,
38042 Grenoble Cedex 9, France.

D Laboratoire Léon Brillouin,
CEA-CNRS, CEA Saclay,
91191 Gif-sur-Yvette, France.

Guy.Schlatter@unistra.fr

The design of self-assembled supramolecular structures has become of great interest over the recent years because of their ability to form or to deform under appropriate conditions. Among these supramolecular assemblies, pseudo-polyrotaxanes (pPRs) are inclusion complexes (ICs) in the form of necklaces elaborated thanks to host-guest interactions allowing the threading of ring-like molecules onto a polymer chain.

Triblock copolymers of polyethylene oxide (PEO)-b-polypropylene oxide (PPO)-b-polyethylene oxide (PEO) (also known as pluronics®) and β -CDs are known to form ICs. Indeed, while α -CD is known for its selective stable inclusion of the EO units only, [2,3] β -CD exhibits steric compatibility that enables it to fit both EO and PO units, with a higher affinity toward PO units.

In this work,[4] we used an aqueous solution of native β -CD in addition to an aqueous dilute solution of pluronic F-68 (EO76-PO29-EO76, average number molecular weight of ~ 8400 kg.mol⁻¹). Temperature lowering was used to break the micelles and allow inclusion to happen. The initial mixture was transparent. Due to the poor solubility of β -CD and pluronic ICs, it becomes opalescent

Cyclodextrins (CDs) build a family of cyclic oligosaccharides with 6, 7, or 8 repeating glucose units (α -, β -, and γ -CD respectively). Their hollow truncated conic conformation, with a more hydrophobic internal cavity and a more hydrophilic external surface, enables them to build pPRs with many polymer chains under favourable conditions.[1]

within a few minutes and eventually precipitates into a swollen membrane after several days. Small angle neutron scattering (SANS) experiments and atomic force microscopy (AFM) follow-ups evidenced the formation of large-scale structures with time.

Fig. 1 presents the scattering data of the three main consecutive states of the mixture obtained during each step of the procedure, and shows its general evolution. It confirms the existence of a steady state at 70°C. The observed hump in the low q range is most likely characteristic of the presence of well-known micellar structures of pluronics. Upon cooling to 40°C, the intensity of the signal dramatically decreased, which suggests the disruption of these objects and a homogenisation of the mixture. Then the signal evolved with time as inclusion complexation took place. The progressive appearance of a steep hump at lower q -values can be attributed to the formation of larger-scale structures due to self-organization of ICs. A final steady state is reached after several hours.

Complementary SANS measurements of isolated molecules demonstrate that during the first step at 70°C, the mixture is in a steady state, where native β -CDs do not disrupt the pluronic micelles but participate in their structure as being part of the core.

When the mixture is quenched down to 40°C, in the very first moments, SANS data show the contribution of isolated pluronics Gaussian chains and β -CD molecules. Then, during solution ageing, we evidenced the formation of β -CD/pluronic pPRs which self-organize in the form of thin nano-platelets (17 nm thick and planar dimensions of about 4 μ m). The entire data were modelled by a linear combination of two fits used for both low and high q ranges.

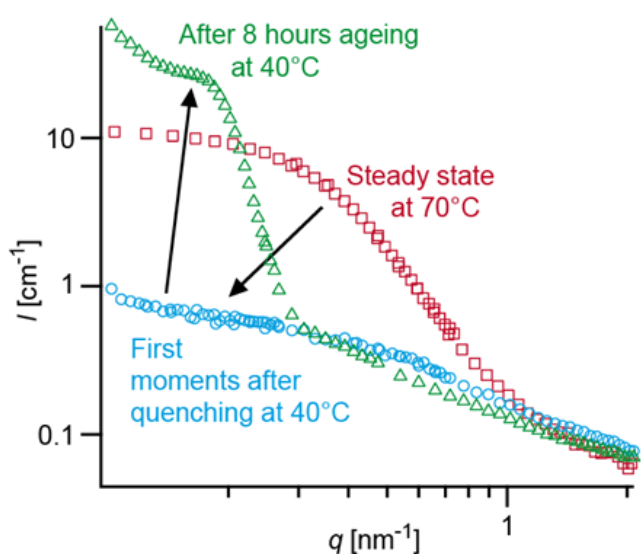


Figure 1: An overview of the SANS evolution in the mixture: the initial steady state at 70°C (\square), the intermediary state just after mixing and thermal quenching at 40°C (\circ), and the state after 8 hours ageing at 40°C (Δ).

At low q , a rigid parallelepipedic platelets form factor is considered whereas at high q range, the contribution of cylindrical assemblies must be taken into account.

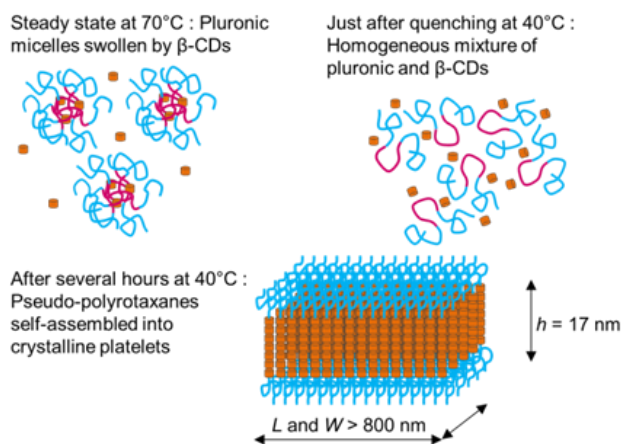


Figure 2: The obtained structures at initial steady state at 70°C, at intermediary state just after mixing and thermal quenching at 40°C and the state after 8 hours ageing at 40°C.

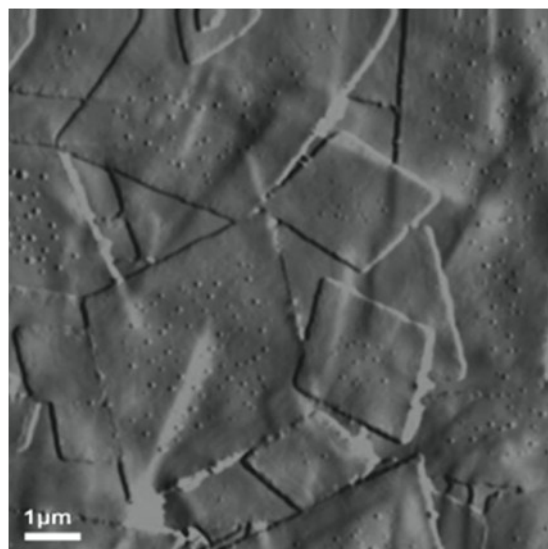
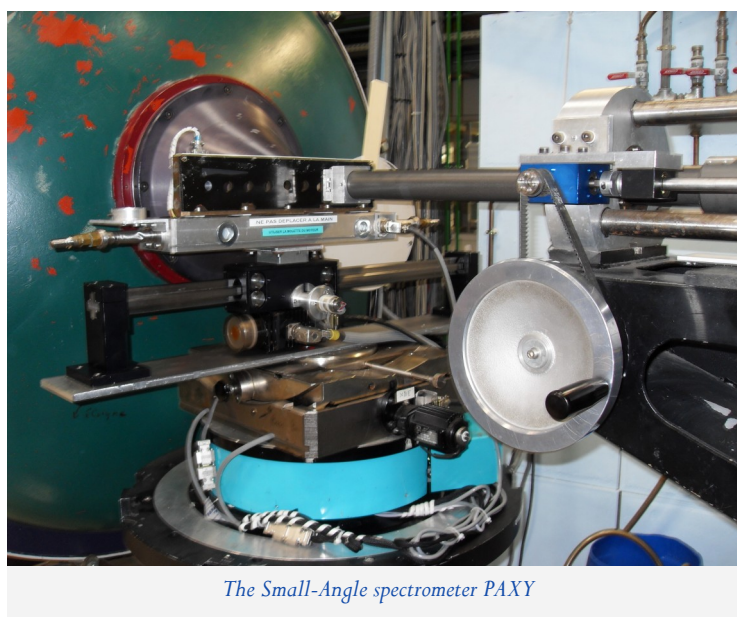


Figure 3: Tapping mode AFM phase imaging on deposited films from the mixture of F-68 and β -CD after quenching to 40°C and 3 weeks ageing. The scale bar is 1 μ m long.

Thus, the platelets are themselves composed of an association of cylinders with length equal to the platelet thickness corresponding in one monolayer of pPRs. Moreover, the shape of scattered intensity at high q values implies that these platelets are made of the association of pPR bundles. Their diameter

being 4.8 nm and that of β -CD 1.54 nm, the model suggests that ~ 7 pPRs self-assemble to form these cylindrical bundles. Furthermore, AFM shows a crystallographic angle of 105.4°.



The Small-Angle spectrometer PAXY

References

1. G. Wenz, B.-H. Han and A. Müller, *Chemical Reviews*, 2010, 43, 1915-1921.
2. C. Travelet, G. Schlatter, P. Hébraud, C. Brochon, A. Lapp, G. Hadziioannou, *Langmuir*, 2009, 25, 8723-8734.
3. C. Travelet, P. Hébraud, C. Perry, C. Brochon, G. Hadziioannou, A. Lapp, G. Schlatter, *Macromolecules*, 2006, 106, 782-817.
4. C. Perry, P. Hébraud, V. Gernigon, C. Brochon, A. Lapp, P. Lindner, G. Schlatter, *Soft Matter*, 2011, 7, 3502-3512.

Investigation of polymer hydrogels with memory effect for cefazoline immobilization, by small-angle neutron scattering

Y.U.V. KULVELIS^A, V.T. LEBEDEV^A, V.A. TRUNOV^A, S.S. IVANCHEV^B, O.N. PRIMACHENKO^B, S.Y.A. KHAIKIN^B, V.N. PAVLYUCHENKO^B, J. TEIXEIRA^C & S. COMBET^C

A B.P. Konstantinov Petersburg Nuclear Physics Institute, Gatchina, Russia

B G.K. Boreskov Institute of Catalysis, St Petersburg branch, Saint Petersburg, Russia

C Laboratoire Léon Brillouin, CEA-CNRS, CEA Saclay, 91191 Gif-sur-Yvette, France

kulvelis@pnpi.spb.ru

Hydrogels synthesized on the base of cross-linked Saclay, France). Differences in structure of anionic copolymers of 2-hydroxyethylmethacrylate and acrylic acid or dimethylaminoethylmethacrylate) with a memory effect to absorbance ability in absence or in presence of target medicine – cefazoline – were studied by small-angle neutron scattering at PAXE (LLB,

Polymer hydrogels are typical materials for soft contact lenses (SCL), as medicine carriers in treating ophthalmologic diseases. To increase the medicine content in hydrogel, it can be synthesized in presence of the medicine as a template and extracted after the synthesis, thus obtaining an “imprinted” polymer hydrogel with a memory effect to the medicine due to formation of specific nanoporous structure [1–6]. The preliminary tests on hydrogels, saturated with H₂O, were published in [7].

We studied the structure of new polymer hydrogels with memory effect, based on 2-hydroxyethylmethacrylate (HEMA), cross-linking monomer methylenebisacrylamide and functional monomers – acrylic acid (AA, anionic groups) and dimethylaminoethyl methacrylate (DMAEMA, cationic groups). The template medicine was cefazoline, an antibiotic widely used to treat and prevent infectious ophthalmologic diseases.

Small-angle scattering was measured at PAXE in the range of $q = 0,004-0,3 \text{ \AA}^{-1}$ and $\lambda = 4-12 \text{ \AA}$.

3 types of samples – anionic (1), cationic (2) and amphiphilic (3) were both in simple state and imprinted (synthesized at the presence of cefazoline) and measured in 4 series each:

D – saturated with D₂O,

C – saturated with cefazoline solution 9,5% in D₂O,

H – saturated with H₂O,

dry – dried on the air.

Typical curves are shown at Fig. 1 for sample “1 simple state” in different conditions.

All scattering curves are well described by a model (1):

$$\frac{d\Sigma}{d\Omega} = C_1 e^{-\frac{(R_g q)^2}{3}} + \frac{C_2}{1+(R_{g2}q)^2} + \frac{C_3}{(1+(R_{g3}q)^2)^2} + B \quad (1)$$

where first term is Guinier function with radius

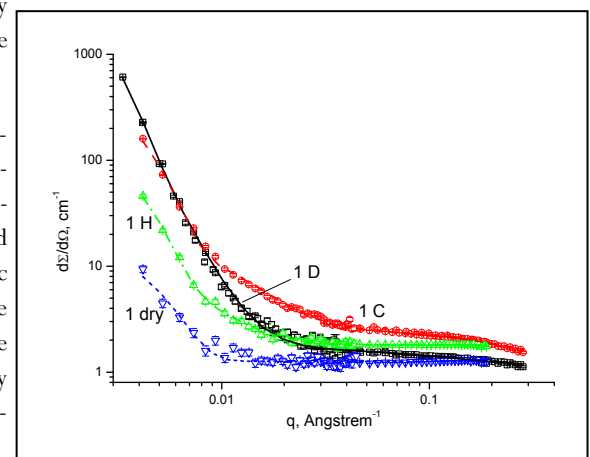


Figure 1 : Scattering curves on sample “1 simple state” in different conditions

of gyration R_{g1} , and describes the most small-angle range, then – Lorentz function describing loose objects (density fluctuations) with correlation length R_{g2} , then – squared Lorentz function describing dense objects (sharp globules) with correlation length R_{g3} , and incoherent background B .

Fitting with the use of model (1) showed that samples “2 simple state” and “2 imprinted” (cationic) in saturated state (H, D and C conditions) are the less dense to be compared with anionic and amphiphilic samples.

Anionic samples “1” at the presence of cefazoline show decreasing the number of dense objects that

leads to more uniform distribution of water in sample volume.

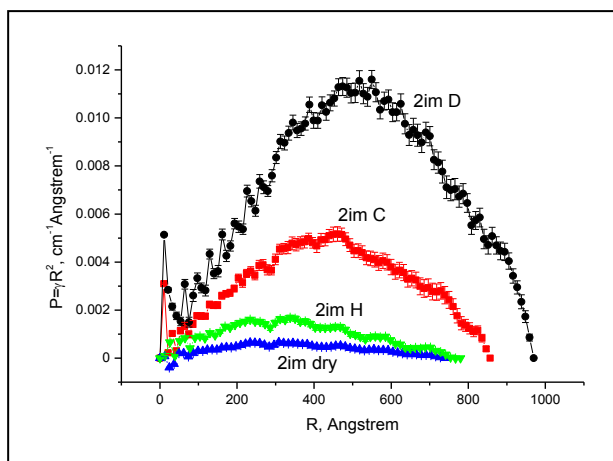


Figure 2 : Correlation functions of sample "2 imprinted" in different conditions

Scattering curves allowed us to reconstruct the correlation functions in direct space in spherical representation $gR^2(R)$. Fig. 2. shows examples of correlation functions for sample "2 imprinted" in different conditions. The curves have narrow peaks at low R, as also in samples "2 simple state", "3 simple state" and "3 imprinted". Anionic samples ("1 simple state" and "1 imprinted") have too much intensity at large R and the peak at small R is not visible. Cefazoline makes the correlation intensity for sample "2 imprinted" much lower and de-

creases the average distances from 500-600 Å to 400-500 Å (curves 2im D and 2im C in Fig. 2). As their swelling degrees are similar, it means that cefazoline solution distributes in polymer volume more uniformly, than D₂O without cefazoline, which can form larger objects.

Among other results we notice the following:

1. Presence of cefazoline in hydrogel increases its swelling degree. This effect increases even more for imprinted samples to be compared with normal ones.
2. Hydrogels structure is characterised by small objects, below 10 Å, and larger entities up to 1000 Å. Small objects can be hardly observed in anionic samples, as large objects in their structure are dominating. Cationic hydrogels are more loose in saturated states than anionic and amphiphilic (there is a larger number of loose objects and a smaller amount of dense objects).
3. Synthesis of imprinted hydrogels (in presence of cefazoline) leads to additional ordering in internal structure of anionic and cationic hydrogels, and increasing the number of large objects in structure of saturated samples. Amphiphilic imprinted hydrogel shows more uniform internal structure, with smaller number of large objects as compared to normal amphiphilic sample. These facts can be important for the practical purposes.



The Small-Angle spectrometer PAXE

References

1. Cunliffe D., Kirby A., Alexander C., *Adv. Drug Del. Rev.*, 2005, 57, 1836.
2. Alvarez-Lorenzo C., Concheiro A., *J. Chromatography B*, 2004, 804, 231.
3. Ali M., Horikawa S., Venkatesh S. et al., *J. Control. Release*, 2007, 124, 154.
4. Alonso M.J., Sánchez A., *J. Pharm. Pharmacol.*, 2003, 55, 1451.
5. Hiratani H., Fujiwara A., Tamiya Y. et al., *Biomaterials*, 2005, 26, 1293.
6. Pavlyuchenko V.N., Ivanchev S.S., Primachenko O.N. et al., *Polymer Science A*, 2011, 53, 323.
7. Kulvelis Yu.V., Lebedev V.T., Trunov V.A. et al., *Crystallography Reports*, 2011, 56, 30.

Wall thickness determination of hydrophobically functionalized MCM-41 materials

M. SCHOEFFEL^A, N. BRODIE-LINDER^B, F. AUDONNET^C & C. ALBA-SIMIONESCO^D

A Laboratoire d'Optique et Biosciences, CNRS UMR 7645 – Inserm U 696, Ecole Polytechnique, 91128 Palaiseau, France

B Laboratoire de Synthèse Organique Sélective et de Chimie Bioorganique, Université de Cergy–Pontoise, 95031 Cergy–Pontoise, France

C Institut Pascal, axe GePEB, CNRS UMR 6602, Université Blaise Pascal, 63177 Aubière Cedex, France

D Laboratoire Léon Brillouin, CEA-CNRS, CEA Saclay, 91191 Gif-sur-Yvette, France

nancy.brodie-linder@u-cergy.fr

nancy.linder@cea.fr

We have developed a new protocol for simple and convenient synthesis of MCM-41 porous material. Post-synthetic grafting of $-\text{Si}(\text{CH}_3)_2\text{R}$ groups, where R stands for methyl (called OSiMe_3), phenyl (called OSiMe_2Ph), or hexyl (called OSiMe_2Hex), respectively, yielded hydrophobic porous material by addition of an organic layer to the surface silanols. Modified materials and the hydrophilic precursor were characterized by a combination of nitrogen adsorption and small angle neutron scattering. We found that pore

Much attention has been paid to porous materials due to their versatility. Among these materials, the class of MCM-41 [2] stands out due to its highly unusual pore texture resulting from long-range ordering and extremely high surface areas in the order of $1000 \text{ m}^2 \text{ g}^{-1}$. The MCM-41 structure on the nm scale is reported as a hexagonal stacking of porous tubes of uniform diameter. MCM-41 is therefore the material of choice for studies of thermophysical properties of liquids in confinement.³ However, despite the huge amount of research devoted to MCM-41 materials, only a small number deal with hydrophobic variants of this material. Studies concerning the characterization of the surface properties of these materials deal, in most cases, with the interaction between the hydrophobic surface and an adsorbed species. To some lesser extent, mechanistic and kinetic parameters of the modification reaction, surface coverage rates depending on steric bulk of the grafted groups and reactivity and silanization efficiency have been studied but not the conformational properties of the modification layer itself. Characterization of mesoporous materials is usually achieved by nitrogen adsorption. Analysis of the results according to the theory of Brunauer, Emmett and Teller yields the fluid/wall affinity, the specific surface, the pore volume and the hydraulic pore radius. The pore size distribution can also be obtained with the Kruk–Jaroniec–Sayari model, KJS. However, adsorption measurements cannot reveal comprehensive information about the material in the case of an organic moiety grafted to the surface. In this case, an additional recourse to scattering techniques, SAXS or SANS, is necessary in order to charac-

terize the periodically ordered materials. sizes calculated from the nitrogen adsorption data depend strongly on the chosen model, as expected. Pore sizes from neutron scattering data do not demand simplifying model assumptions and were therefore used in order to calculate the thickness of the grafted organic layer. Comparison of the experimentally measured thickness with the theoretical lengths of the grafted groups allowed us to deduce the conformation of the organic moiety.

size the periodically ordered materials.

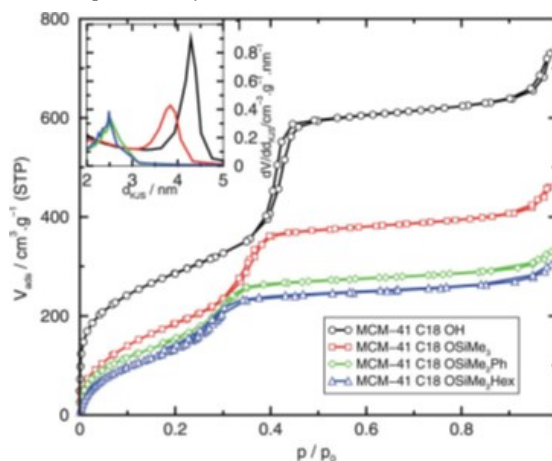


Figure 1 : Comparison between nitrogen adsorption in mesoporous materials with different surface-grafted groups. The inset shows the mesoporous size distribution.

Nitrogen adsorption isotherms are shown in Fig. 1. As the precursor material was the same for all grafting reactions, a difference in the adsorption properties of the modified material means that gas adsorption measurements enable the detection of the different space requirements of single grafted groups in the pores. As the space requirement of a methyl group is without a doubt smaller than that of either phenyl or hexyl groups, we would expect that the adsorbable gas volume is larger in the case of the trimethyl silyl modification compared to the other silanizations. This expectation is very well confirmed as we can see from the high relative pressure plateau of the adsorption isotherms. Taking into account only the adsorption results, we can conclude that the hexyl chains are in a conformation that has a

slightly larger space requirement than the phenyl rings.

Neutron scattering was performed at the SANS instrument PAXE at the Laboratoire Léon Brillouin. The fitting of the scattering intensities $I(q)$, after assumptions, was done using the following equation,

$$I(q) = C_1 + C_2 q^{-a} + C_3 q^{-4} \cdot \exp\left[-\frac{(q - q_{10})^2}{2s^2}\right] \quad (1)$$

where C_1 is a constant taking in account a isotropic background, C_2 is a constant, a is comprise between 3 and 4 and leads to a surface dimensionality definition of $D = 6 - a$, C_3 accounts for all parameters which cannot be extracted individually due to the limited resolution, q_{10} is the first Bragg peak reflection and s is the characteristic half-width. Data and fits are shown on Fig. 2.

It is possible to combine nitrogen adsorption isotherms and SANS to obtain a pore size. For uniform cylindrical pores in a hexagonal pattern, one obtains:

$$d_{SANS} = c d_{10} \sqrt{\frac{\rho V_p}{1 + \rho V_p}} \quad (2)$$

where $c = 1.213$, d_{10} calculated from the q_{10} value is the lattice plane spacing, r is the SiO_2 wall density (2.2 g.cm^{-3}) and V_p is the pore volume. If we compare the pore sizes for non-modified and modified samples determined by SANS with those from the gas adsorption measurements, we find that neutron scattering always yields higher values. A possible explanation for this phenomenon is that neutrons are scattered in the surface layer by the nuclei of the silanol or grafted groups whereas gas adsorption relies on the interaction of this layer with gas molecules adsorbed onto the surface. Therefore, neutrons measure a real repetition length in the material but gas adsorption can only determine the space accessible in the pore probed by a molecule of finite size. From these results it is then possible to evaluate the thickness of the grafted organic layer, using the data of the center-to-center distance of the hexagonal pore arrangement in MCM-41 and d_{SANS} . For the non surface modified sample, we calculated the thickness of the wall of 0.76 nm. This is in good agreement with literature data (0.8-1.2 nm). A major result is obtained from the comparison of the measured thickness of the modification layer e_{ol} and the theoretical length of a fully elongated conformation ϵ_{geom} of the corresponding group. It follows that in the case of the trimethyl silyl modification, the measured and theoretical values correspond within an error

of 0.1 nm. This difference can be attributed to inaccuracies in the measurement process because the methyl groups have only one possible conformation. It is immediately evident in doing so that the hexyl group cannot be in an elongated conformation perpendicular to the surface and that the phenyl rings are not oriented straight towards the middle of the pore but are in an inclined conformation. We conclude that a conformation of phenyl rings or hexyl groups lying flat on the surface is unlikely as this would lead to a value of e_{ol} in the range of that for the trimethyl silyl modification.

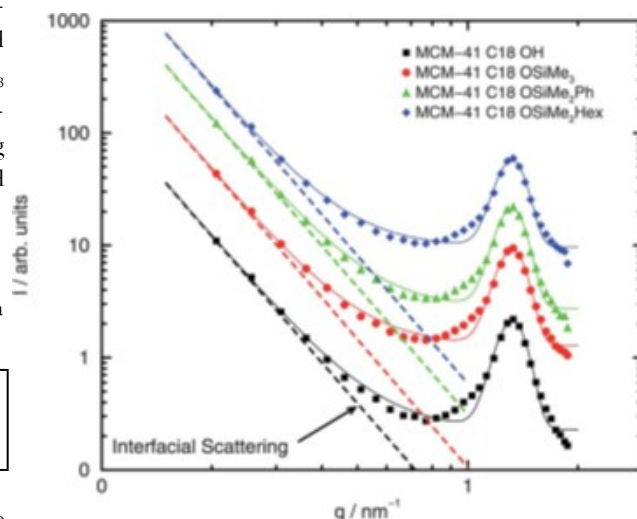


Figure 2 : Fits of the (10) Bragg peak in MCM-41 with different surface modifications. The solid lines indicate the fit of the data according eqn (1). Data of the modified samples were multiplied by a factor as following for better visualization: 2.5 (OSiMe₃), 5 (OSi-Me₂Ph), 15 (OSiMe₂Hex).

We can also calculate the thickness of the organic layer exclusively from nitrogen adsorption data. Comparing the pore sizes from SANS to those calculated with the KJS model, we find only small differences for KJS pore sizes bigger than 3 nm but the discrepancy is quite big for those smaller than 3 nm. Summarizing these findings, we can conclude that for pore sizes smaller than about 3 nm only scattering data can provide more consistent results.

References

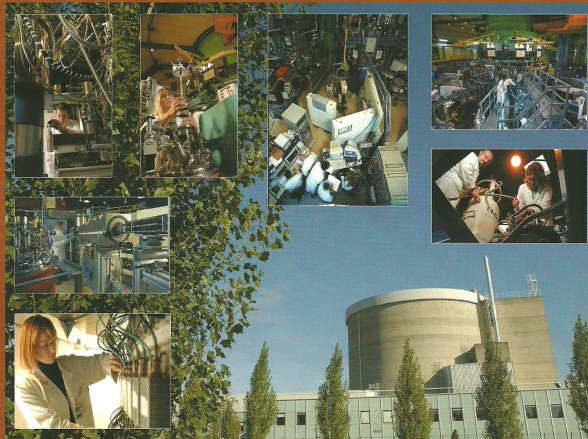
1. M. Schoeffel, N. Brodie-Linder, F. Audonnet and C. Alba-Simionesco, *J. Mater. Chem.*, 2012, 22, 557-567.
2. C. Alba-Simionesco, B. Coasne, G. Dosseh, G. Dudziak, K. Gubbins, R. Radhakrishnan and M. Sliwinska-Bartkowiak, *J. Phys.: Condens. Matter*, 2006, 18, R15-R68.
3. C. Kresge, M. Leonowicz, W. Roth, J. Vartuli and J. Beck, *Nature*, 1992, 359, 710-712.

Neutron News

 Taylor & Francis
Taylor & Francis Group

FEATURING:
The Laboratoire Léon Brillouin

Volume 22, Issue 4
October/November/December 2011



IN THIS ISSUE

The Laboratoire Léon Brillouin and the Orphee Reactor:
The French National Neutron Facility

LLB Instrumentation Program CAP 2015

Puzzling Multiferroics

Present and Future of the Quasi-elastic Neutron Spectroscopy at LLB.
More than Simply Samples: Devices

Neutron Scattering on Magnetic Thin Films

Special issue of "Neutron News" dedicated to LLB (October 2011)

PUBLICATIONS

2011

- 1 *Depletion induced vesicle-to-micelle transition from self-assembled rod-coil diblock copolymers with spherical magnetic nanoparticles.* Agut W; Taton D; Brulet A; Sandre O; Lecommandoux S. **Soft Matter**, Vol. 7(20), pp 9744-9750, (2011)
- 2 *Synthesis and Structure Determination of the High Temperature Form of La(2)WO(6).* Allix M; Chambrier M.H; Veron E; Porcher F; Suchomel M. and Goutenoire F. **Crystal Growth & Design**, vol. 11(11), pp. 5105-5112, (2011)
- 3 *Signatures of spin-glass behavior in the induced magnetic moment system PrRuSi(3).* Anand V. K., Adroja D. T., Hillier A. D., Taylor J. and Andre G. **Physical Review B**, vol. 84(6), pp., (2011)
- 4 *Temperature dependence of low-energy phonons in magnetic nonsuperconducting TbNi(2)B(2)C.* Anissimova S., Kreyssig A., Stockert O., Loewenhaupt M. and Reznik D. **Physical Review B**, vol. 84(10), pp., (2011)
- 5 *Kam Tori And Absence Of Diffusion Of A Wave-Packet In The 1d Random DNLS Model.* Aubry S. **International Journal of Bifurcation and Chaos**, vol. 21(8), pp. 2125-2145, (2011)
- 6 *Evidence for competing magnetic instabilities in underdoped YBa(2)Cu(3)O(6+x).* Baledent V., Haug D., Sidis Y., Hinkov V., Lin C. T. and Bourges P. **Physical Review B**, vol. 83(10), pp., (2011)
- 7 *Small angle neutron scattering as fingerprinting of ancient potteries from Sicily (Southern Italy).* Barone G., Crupi V., Majolino D., Mazzoleni P., Teixeira J., Venuti V. and Scandurra A. **Applied Clay Science**, vol. 54(1), pp. 40-46, (2011)
- 8 *Osmotically induced deformation of capsid-like icosahedral vesicles.* Bealle G., Jestin J. and Carriere D. **Soft Matter**, vol. 7(3), pp. 1084-1089, (2011)
- 9 *Systematical, experimental investigations on LiMgZ (Z = P, As, Sb) wide band gap semiconductors.* Beleanu A., Mondeshki M., Juan Q., Casper F., Felser C. and Porcher F. **Journal of Physics D-Applied Physics**, vol. 44(47), pp., (2011)
- 10 *Study of Inconel 718 weldability using MIG CMT process.* Benoit A., Jobez S., Paillard P., Klosek V. and Baudin T. **Science and Technology of Welding and Joining**, vol. 16(6), pp. 477-482, (2011)
- 11 *Effect of electron doping on the magnetic correlations in the bilayered brownmillerite compound Ca(2.5-x)La(x)Sr(0.5)GaMn(2)O(8): a neutron diffraction study.* Bera A. K., Yusuf S. M. and Mirebeau I. **Journal of Physics-Condensed Matter**, vol. 23(42), pp., (2011)
- 12 *Functionalized nanoporous track-etched beta-PVDF membrane electrodes for lead(II) determination by square wave anodic stripping voltammetry.* Bessbousse H., Nandhakumar I., Decker M., Barsbay M., Cuscito O., Lairez D., Clochard M. C. and Wade T. L. **Analytical Methods**, vol. 3(6), pp. 1351-1359, (2011)
- 13 *Tetragonal distortion yielding a two-singlet spin liquid in pyrochlore Tb(2)Ti(2)O(7).* Bonville P., Mirebeau I., Gukasov A., Petit S. and Robert J. **Physical Review B**, vol. 84(18), pp., (2011)
- 14 *pH-triggered reversible sol-gel transition in aqueous solutions of amphiphilic gradient copolymers.* Borisova O., Billon L., Zaremski M., Grassl B., Bakaeva Z., Lapp A., Stepanek P. and Borisov O. **Soft Matter**, vol. 7(22), pp. 10824-10833, (2011)
- 15 *Local magnetic moments in a dinuclear Co(2+) complex as seen by polarized neutron diffraction: Beyond the effective spin-1/2 model.* Borta A., Gillon B., Gukasov A., Cousson A., Luneau D., Jeanneau E., Ciunacov I., Sakiyama H., Tone K. and Mikuriya M. **Physical Review B**, vol. 83(18), pp., (2011)
- 16 *Novel magnetic order in the pseudogap state of high-T(c) copper oxides superconductors.* Bourges P. and Sidis Y. **Comptes Rendus Physique**, vol. 12(5-6), pp. 461-479, (2011)
- 17 *Third harmonics nonlinear susceptibility in supercooled liquids: A comparison to the box model.* Brun C., Crauste-Thibierge C., Ladieu F. and L'Hote D. **Journal of Chemical Physics**, vol. 134(19), pp., (2011)
- 18 *Formation mechanism, structure and adsorption characteristics of microporous nanocrystalline thin-film (V,Ti)-N-He composites.* Bryk V. V., Vasilenko R. L., Goncharov A. V., Grogorova T. K., Guglya A. G., Kolo-brodov V. G., Litvinenko M. L., Marchenko I. G., Mel'nikova E. S., Sassa I. V., Nikitenko Y. V., Khaidukov Y. N., Volkov V. V. and Chaboussant G. **Journal of Surface Investigation-X-Ray Synchrotron and Neutron Techniques**, vol. 5(3), pp. 566-574, (2011)
- 19 *The non-Gaussian dynamics of glycerol.* Busselez R., Lefort R., Ghoufi A., Beuneu B., Frick B., Affouard F. and Morineau D. **Journal of Physics-Condensed Matter**, vol. 23(50), pp., (2011)
- 20 *Coloured Semi-reflective Thin Films for Biomass-hydrolyzing Enzyme Detection.* Cerclier C., Guyomard-Lack A., Moreau C., Cousin F., Beury N., Bonnin E., Jean B. and Cathala B. **Advanced Materials**, vol. 23(33), pp. 3791+, (2011)
- 21 *Dynamic and sub-ambient thermal transition relationships in water-sucrose solutions.* Champion D., Loupiac C., Russo D., Simatos D. and Zanotti J. **Journal of Thermal Analysis and Calorimetry**, vol. 104(1), pp. 365-374, (2011)

- 22 *Helical magnetic state in the distorted triangular lattice of alpha-CaCr(2)O(4)*. Chapon L. C., Manuel P., Damay F., Toledano P., Hardy V. and Martin C. **Physical Review B**, vol. 83(2), pp., (2011)
- 23 *Polymer-Grafted-Nanoparticles Nanocomposites: Dispersion, Grafted Chain Conformation, and Rheological Behavior*. Chevigny C., Dalmás F., Di Cola E., Gignes D., Bertin D., Boue F. and Jestin J. **Macromolecules**, vol. 44(1), pp. 122-133, (2011)
- 24 *Controlled grafting of polystyrene on silica nanoparticles using NMP: a new route without free initiator to tune the grafted chain length*. Chevigny C., Gignes D., Bertin D., Schweins R., Jestin J. and Boue F. **Polymer Chemistry**, vol. 2(3), pp. 567-571, (2011)
- 25 *Tuning the Mechanical Properties in Model Nanocomposites: Influence of the Polymer-Filler Interfacial Interactions*. Chevigny C., Jouault N., Dalmás F., Boue F. and Jestin J. **Journal of Polymer Science Part B-Polymer Physics**, vol. 49(11), pp. 781-791, (2011)
- 26 *Adsorption, structure and dynamics of benzene in ordered and disordered porous carbons*. Coasne B., Alba-Simionesco C., Audonnet F., Dossè G. and Gubbins K. E. **Physical Chemistry Chemical Physics**, vol. 13(9), pp. 3748-3757, (2011)
- 27 *Structure of Polyelectrolytes with Mixed Monovalent and Divalent Counterions: SAXS Measurements and Poisson-Boltzmann Analysis*. Combet J., Rawiso M., Rochas C., Hoffmann S. and Boue F. **Macromolecules**, vol. 44(8), pp. 3039-3052, (2011)
- 28 *Temperature- and hydration-dependent internal dynamics of stripped human erythrocyte vesicles studied by incoherent neutron scattering*. Combet S., Zanotti J. M. and Bellissent-Funel M. C. **Biochimica Et Biophysica Acta-General Subjects**, vol. 1810(2), pp. 202-210, (2011)
- 29 *Antiferromagnetic order in tetragonal bismuth ferrite-lead titanate*. Comyn T. P., Stevenson T., Al-Jawad M., Andre G., Bell A. J. and Cywinski R. **Journal of Magnetism and Magnetic Materials**, vol. 323(21), pp. 2533-2535, (2011)
- 30 *Influence of chain interdiffusion between immiscible polymers on dewetting dynamics*. Coppee S., Gabriele S., Jonas A. M., Jestin J. and Daman P. **Soft Matter**, vol. 7(21), pp. 9951-9955, (2011)
- 31 *Structural changes between soda-lime silicate glass and melt*. Cormier L., Calas G. and Beuneu B. **Journal of Non-Crystalline Solids**, vol. 357(3), pp. 926-931, (2011)
- 32 *Structural and dynamic properties of confined ethane in AlPO(4)-5 model microporous aluminophosphate: Does the predicted quasi-(1D) phase transition exist?* Coulomb J. P., Floquet N. and Andre G. **Microporous and Mesoporous Materials**, vol. 141(1-3), pp. 43-48, (2011)
- 33 *The model Lysozyme-PSSNa system for electrostatic complexation: Similarities and differences with complex coacervation*. Cousin F., Gummel J., Combet S. and Boue F. **Advances in Colloid and Interface Science**, vol. 167(1-2), pp. 71-84, (2011)
- 34 *EROS II: A boosted time-of-flight reflectometer for multi-purposes applications at the Laboratoire Leon Brillouin*. Cousin F., Ott F., Gibert F. and Menelle A. **European Physical Journal Plus**, vol. 126(11), pp., (2011)
- 35 *Magnetoelastic coupling and unconventional magnetic ordering in the multiferroic triangular lattice AgCrS(2)*. Damay F., Martin C., Hardy V., Andre G., Petit S. and Maignan A. **Physical Review B**, vol. 83(18), pp., (2011)
- 36 *Quantum gapped spin excitations in the S=3/2 zigzag ladder compound beta-CaCr(2)O(4)*. Damay F., Martin C., Hardy V., Maignan A., Stock C. and Petit S. **Physical Review B**, vol. 84(2), pp., (2011)
- 37 *BaCoO(3) (n) BaCo(8)O(11) Modular Intergrowths: Singularity of the n=2 Term*. David R., Pautrat A., Kabbour H., Sturza M., Curelea S., Andre G., Pelloquin D. and Mentre O. **Chemistry of Materials**, vol. 23(23), pp. 5191-5199, (2011)
- 38 *Nanocavities trapped along fibrin fibers allow the diffusion of thrombolytic drugs*. De Spirito M., Missori M., Maulucci G., Teixeira J. and Papi M. **Applied Physics Letters**, vol. 99(22), pp., (2011)
- 39 *"Click" Conjugation of Peptide on the Surface of Polymeric Nanoparticles for Targeting Tumor Angiogenesis*. Deshayes S., Maurizot V., Clochard M. C., Baudin C., Berthelot T., Esnouf S., Lairez D., Moenner M. and Deleris G. **Pharmaceutical Research**, vol. 28(7), pp. 1631-1642, (2011)
- 40 *Determination Of The Diffusive Motion Of Water Molecules In Hydrated Cement Paste By Quasielastic Neutron Scattering*. Dragolici C. A., Kahn R. and Dragolici F. **Romanian Reports in Physics**, vol. 63(2), pp. 465-470, (2011)
- 41 *Weak Temperature Dependence of Structure in Hydrophobic Polyelectrolyte Aqueous Solution (PSSNa): Correlation between Scattering and Viscosity*. Essafi W., Haboubi N., Williams C. and Boue F. **Journal of Physical Chemistry B**, vol. 115(29), pp. 8951-8960, (2011)
- 42 *Insight into Asphaltene Nanoaggregate Structure Inferred by Small Angle Neutron and X-ray Scattering*. Eyssautier J., Levitz P., Espinat D., Jestin J., Gummel J., Grillo I. and Barre L. **Journal of Physical Chemistry B**, vol. 115(21), pp. 6827-6837, (2011)
- 43 *Frustration-driven magnetic order in hexagonal InMnO(3)*. Fabreges X., Mirebeau I., Petit S., Bonville P. and Belik A. A. **Physical Review B**, vol. 84(5), pp., (2011)
- 44 *Multiscale Structural Characterizations of Fatty Acid Multilayered Tubes with a Temperature-Tunable Diameter*. Fameau A. L., Cousin F., Navailles L., Nallet F., Boue F. and Douliez J. P. **Journal of Physical Chemistry B**, vol. 115(29), pp. 9033-9039, (2011)
- 45 *Adsorption of multilamellar tubes with a temperature tunable diameter at the air/water interface*. Fameau A. L., Douliez J. P., Boue F., Ott F. and Cousin F. **Journal of Colloid and Interface Science**, vol. 362(2), pp. 397-405, (2011)
- 46 *Smart Foams: Switching Reversibly between Ultrastable and Unstable Foams*. Fameau A. L., Saint-Jalmes A., Cousin F., Houssou B. H., Novales B., Navailles L., Nallet F., Gaillard C., Boue F. and Douliez J. P. **Angewandte Chemie-International Edition**, vol. 50(36), pp. 8264-8269, (2011)
- 47 *Self-Assembly, Foaming, and Emulsifying Properties of Sodium Alkyl Carboxylate/Guanidine Hydrochloride Aqueous Mixtures*. Fameau A. L. F. A. L., Houinsou-Houssou B., Ventureira J. L., Navailles L., Nallet F., Novales B. and Douliez J. P. **Langmuir**, vol. 27(8), pp. 4505-4513, (2011)
- 48 *Enhancing the Superconducting Transition Temperature of BaSi(2) by Structural Tuning*. Flores-Livas J. A., Debord R., Botti S., San Miguel A., Marques M. A. L. and Pailhes S. **Physical Review Letters**, vol. 106(8), pp., (2011)
- 49 *Superconductivity in layered binary silicides: A density functional theory study*. Flores-Livas J. A., Debord R., Botti S., San Miguel A., Pailhes

- S. and Marques M. A. L. **Physical Review B**, vol. 84(18), pp., (2011)
- 50 *Progress in neutron reflectometry instrumentation*. Fragneto G. and Menelle A. **European Physical Journal Plus**, vol. 126(11), pp., (2011)
- 51 *Local structure of polymeric ferrogels*. Galicia J. A., Cousin F., Dubois E., Sandre O., Cabuil V. and Perzynski R. **Journal of Magnetism and Magnetic Materials**, vol. 323(10), pp. 1211-1215, (2011)
- 52 *The effects of cholesterol and beta-sitosterol on the structure of saturated diacylphosphatidylcholine bilayers*. Gallova J., Uhrikova D., Kucerka N., Doktorovova S., Funari S. S., Teixeira J. and Balgavy P. **European Biophysics Journal with Biophysics Letters**, vol. 40(2), pp. 153-163, (2011)
- 53 *Vesicles in Ionic Liquids*. Gayet F., Marty J. D., Brulet A. and Lauthde Viguerie N. **Langmuir**, vol. 27(16), pp. 9706-9710, (2011)
- 54 *Conformational transition of DNA bound to Hfq probed by infrared spectroscopy*. Geinguenaud F., Calandrini V., Teixeira J., Mayer C., Liquier J., Lavelle C. and Arluison V. **Physical Chemistry Chemical Physics**, vol. 13(3), pp. 1222-1229, (2011)
- 55 *Dielectric relaxation in Li-doped KTaO(3) studied by kinetic Monte Carlo*. Geneste G., Kiat J. M., Yokota H. and Uesu Y. **Physical Review B**, vol. 83(18), pp., (2011)
- 56 *Structural Investigation on Thermoresponsive PVA/Poly(methacrylate-co-N-isopropylacrylamide) Microgels across the Volume Phase Transition*. Ghugare S. V., Chiessi E., Fink R., Gerelli Y., Scotti A., Deriu A., Carrot G. and Paradossi G. **Macromolecules**, vol. 44(11), pp. 4470-4478, (2011)
- 57 *Temperature evolution of copper oxide nanoparticles in porous glasses*. Golosovsky I. V., Naberezhnov A. A., Kurdyukov D. A., Mirebeau I. and Andre G. **Crystallography Reports**, vol. 56(1), pp. 164-168, (2011)
- 58 *Chiral criticality in the doped helimagnets Mn(1-y)Fe(y)Si*. Grigoriev S. V., Moskvina E. V., Dyadkin V. A., Lamago D., Wolf T., Eckerlebe H. and Maleyev S. V. **Physical Review B**, vol. 83(22), pp., (2011)
- 59 *Magnetic Blue Phase in the Chiral Itinerant Magnet MnSi*. Hamann A., Lamago D., Wolf T., von Lohneysen H. and Reznik D. **Physical Review Letters**, vol. 107(3), pp., (2011)
- 60 *Growth of quantum paraelectric La(1/2)Na(1/2)TiO(3) single crystals using optical floating zone technique*. Haumont R., Saint-Martin R., Chaigneau J., Devant M., Hermet J., Sekhar B. N., Uesu Y., Itoh M. and Kiat J. M. **Journal of Crystal Growth**, vol. 321(1), pp. 36-39, (2011)
- 61 *Structural changes in liquid crystal polymer vesicles induced by temperature variation and magnetic fields*. Hocine S., Brulet A., Jia L., Yang J., Di Cicco A., Bouteiller L. and Li M. H. **Soft Matter**, vol. 7(6), pp. 2613-2623, (2011)
- 62 *Confined linear molecules inside an aperiodic supramolecular crystal: The sequence of superspace phases in n-hexadecane/urea*. Huard M., Toudic B., Rabiller P., Ecolivet C., Guerin L., Bourges P., Breczewski T. and Hollingsworth M. D. **Journal of Chemical Physics**, vol. 135(20), pp., (2011)
- 63 *Symmetry and structure of multiferroic Ba(2)CoGe(2)O(7)*. Hutano V., Sazonov A., Murakawa H., Tokura Y., Nafradi B. and Chernyshov D. **Physical Review B**, vol. 84(21), pp., (2011)
- 64 *Dynamic competition of DsrA and rpoS fragments for the proximal binding site of Hfq as a means for efficient annealing*. Hwang W., Arluison V. and Hohng S. **Nucleic Acids Research**, vol. 39(12), pp. 5131-5139, (2011)
- 65 *Origin of Absorption Changes Associated with Photoprotective Energy Dissipation in the Absence of Zeaxanthin*. Ilioaia C., Johnson M. P., Duffy C. D. P., Pascal A. A., van Grondelle R., Robert B. and Ruban A. V. **Journal of Biological Chemistry**, vol. 286(1), pp. 91-98, (2011)
- 66 *Dispersion and damping of zone-boundary magnons in the noncentrosymmetric superconductor CePt(3)Si*. Inosov D. S., Bourges P., Ivanov A., Prokofiev A., Bauer E. and Keimer B. **Journal of Physics-Condensed Matter**, vol. 23(45), pp., (2011)
- 67 *Short-Range Spin Order and Frustrated Magnetism in Mn(2)InSbO(6) and Mn(2)ScSbO(6)*. Ivanov S., Nordblad P., Mathieu R., Tellgren R., Politova E. and Andre G. **European Journal of Inorganic Chemistry**, vol. (30), pp. 4691-4699, (2011)
- 68 *Evidence of a framework induced cation redistribution upon water adsorption in cobalt exchanged X faujasite zeolite: A joint experimental and simulation study*. Jeffroy M., Borissenko E., Boutin A., Di Lella A., Porcher F., Souhassou M., Lecomte C. and Fuchs A. H. **Microporous and Mesoporous Materials**, vol. 138(1-3), pp. 45-50, (2011)
- 69 *Structural studies of water in hydrophilic and hydrophobic mesoporous silicas: An x-ray and neutron diffraction study at 297 K*. Jelassi J., Grosz T., Bako I., Bellissent-Funel M. C., Dore J. C., Castricum H. L. and Sridi-Dorbez R. **Journal of Chemical Physics**, vol. 134(6), pp., (2011)
- 70 *Influence of rare-earth ions on SiO(2)-Na(2)O-RE(2)O(3) glass structure*. Johnson J. A., Benmore C. J., Holland D., Du J., Beuneu B. and Mekki A. **Journal of Physics-Condensed Matter**, vol. 23(6), pp., (2011)
- 71 *Structural study of AsS(2)-Ag glasses over a wide concentration range*. Kaban I., Jovari P., Wagner T., Bartos M., Frumar M., Beuneu B., Hoyer W., Mattern N. and Eckert J. **Journal of Non-Crystalline Solids**, vol. 357(19-20), pp. 3430-3434, (2011)
- 72 *The effect of aliphatic alcohols on fluid bilayers in unilamellar DOPC vesicles - A small-angle neutron scattering and molecular dynamics study*. Klacsova M., Bulacu M., Kucerka N., Uhrikova D., Teixeira J., Marrink S. J. and Balgavy P. **Biochimica Et Biophysica Acta-Biomembranes**, vol. 1808(9), pp. 2136-2146, (2011)
- 73 *Antiferromagnetic order and consequences on the transport properties of Ba(4)Ru(3)O(10)*. Klein Y., Rouse G., Damay F., Porcher F., Andre G. and Terasaki I. **Physical Review B**, vol. 84(5), pp., (2011)
- 74 *Magnetic order, transport and infrared optical properties in the ACrO(3) system (A = Ca, Sr, and Pb)*. Komarek A. C., Moller T., Isobe M., Drees Y., Ullbrich H., Azuma M., Fernandez-Diaz M. T., Senyshyn A., Hoelzel M., Andre G., Ueda Y., Gruninger M. and Braden M. **Physical Review B**, vol. 84(12), pp., (2011)
- 75 *Magnetic layered structure for the production of polarized neutron microbeams*. Kozhevnikov S. V., Ruhm A., Ott F., Pleshanov N. K. and Major J. **Physica B-Condensed Matter**, vol. 406(12), pp. 2463-2466, (2011)

- 76 *Palladium urchin-like nanostructures and their H(2) sorption properties*. Ksar F., Sharma G. K., Audonnet F., Beauvier P. and Remita H. **Nanotechnology**, vol. 22(30), pp., (2011)
- 77 *Ordered interfaces for dual easy axes in liquid crystals*. Lacaze E., Apicella A., De Santo M. P., Coursault D., Alba M., Goldmann M. and Barberi R. **Soft Matter**, vol. 7(3), pp. 1078-1083, (2011)
- 78 *Search for an effect of superconductivity on the phonons in Ba(Fe(1-x)Co(x))(2)As(2)*. Lamago D., Pintschovius L., Reznik D., Heid R., Wolf T., Mittal R. and Chaplot S. L. **Physica C-Superconductivity and Its Applications**, vol. 471(23-24), pp. 1595-1597, (2011)
- 79 *Evidence of Deep Water Penetration in Silica during Stress Corrosion Fracture*. Lechenault F., Rountree C. L., Cousin F., Bouchaud J. P., Ponson L. and Bouchaud E. **Physical Review Letters**, vol. 106(16), pp., (2011)
- 80 *Magnetic order in the pseudogap phase of HgBa(2)CuO(4+delta) studied by spin-polarized neutron diffraction*. Li Y., Baledent V., Barisic N., Cho Y. C., Sidis Y., Yu G., Zhao X., Bourges P. and Grenven M. **Physical Review B**, vol. 84(22), pp., (2011)
- 81 *Rheology and SANS on PET-b-PLAc-b-P(DMAEMA)q Triblock Copolymers: Impact of the PET and Polyelectrolyte Chain Length*. Lienafa L., Oberdisse J., Mora S., Monge S. and Robin J. J. **Macromolecules**, vol. 44(13), pp. 5326-5335, (2011)
- 82 *Synthesis, Magnetic Properties, and Magnetic Structure of a Natrochalcite Structural Variant, KM(2)(II)D(3)O(2)(MoO(4))(2) (M = Mn, Fe, or Co)*. Maalej W., Vilminot S., Andre G., Damay F., Elaoud Z., Mhiri T. and Kurmoo M. **Inorganic Chemistry**, vol. 50(8), pp. 3286-3294, (2011)
- 83 *Existence of Two Concomitant Magnetic Structures Below T(Neel) for the Natrochalcite, NaFe(2)(II)(H(3)O(2))(MoO(4))(2)*. Maalej W., Vilminot S., Andre G., Elaoud Z., Mhiri T. and Kurmoo M. **Inorganic Chemistry**, vol. 50(18), pp. 9191-9199, (2011)
- 84 *Pressure-induced change in the magnetic ordering of TbMnO(3)*. Makarova O. L., Mirebeau I., Kichanov S. E., Rodriguez-Carvajal J. and Forget A. **Physical Review B**, vol. 84(2), pp., (2011)
- 85 *Molecular clusters in aqueous solutions of pyridine and its methyl derivatives*. Marczak W. M. W., Czech B., Almasy L. and Lairez D. **Physical Chemistry Chemical Physics**, vol. 13(13), pp. 6260-6269, (2011)
- 86 *Water Dynamics in Hectorite Clays: Influence of Temperature Studied by Coupling Neutron Spin Echo and Molecular Dynamics*. Marry V. M. V., Dubois E., Malikova N., Durand-Vidal S., Longeville S. and Breu J. **Environmental Science & Technology**, vol. 45(7), pp. 2850-2855, (2011)
- 87 *Larmor diffraction measurement of the temperature dependence of lattice constants in CuGeO(3)*. Martin N., Regnault L. P., Klimko S., Lorenzo J. E. and Gahler R. **Physica B-Condensed Matter**, vol. 406(12), pp. 2333-2336, (2011)
- 88 *A Study of Nuclear of Interest Martensitic Steels and FeCr ODS alloys using small angle neutron scattering*. Mathon M. H., de Carlan Y., Zhong S. Y., Henry J., Olivier P., Klosek V. and Ji V. **Advanced Material Science and Technology, Pts 1 and 2**, vol. 675-677, pp. 815-818, (2011)
- 89 *Dipolar interactions in magnetic nanowire aggregates*. Maurer T., Zighem F., Fang W. Q., Ott F., Chaboussant G., Soumare Y., Atmane K. A., Piquemal J. Y. and Viau G. **Journal of Applied Physics**, vol. 110(12), pp., (2011)
- 90 *Composition And Structure Of Solid Solutions In The Bi(2)O(3)-Sio(2)-Vo(2)(5+)O(5) System With The Structure Sillenite*. Mel'nikova T. I., Kuz'micheva G. M., Rybakov V. B., Bolotina N. B., Dubovskii A. B. and Cousson A. **Journal of Structural Chemistry**, vol. 52(3), pp. 510-516, (2011)
- 91 *Structural and magnetic properties of Ru/Ni multilayers*. Mergia K., Tomou A., Panagiotopoulos I. and Ott F. **Journal of Physics D-Applied Physics**, vol. 44(7), pp., (2011)
- 92 *Rodlike Complexes of a Polyelectrolyte (Hyaluronan) and a Protein (Lysozyme) Observed by SANS*. Morfin I. M. I., Buhler E., Cousin F., Grillo I. and Boue F. **Biomacromolecules**, vol. 12(4), pp. 859-870, (2011)
- 93 *SANS Measurements of Semiflexible Xyloglucan Polysaccharide Chains in Water Reveal Their Self-Avoiding Statistics*. Muller F., Manet S., Jean B., Chambat G., Boue F., Heux L. and Cousin F. **Biomacromolecules**, vol. 12(9), pp. 3330-3336, (2011)
- 94 *Salt-Induced Behavior of Internally Self-Assembled Nanodrops: Understanding Stabilization by Charged Colloids*. Muller F., Salonen A., Dulle M. and Glatter O., Trends in Colloid and Interface Science Xxiv. Starov, V. and Prochazka, K. 138: pp. 27-31, (2011)
- 95 *Identification of finite shear-elasticity in the liquid state of molecular and polymeric glass-formers*. Noirez L. N. L., Mendil-Jakani H. and Baroni P. **Philosophical Magazine**, vol. 91(13-15), pp. 1977-1986, (2011)
- 96 *The Use of Highly Ordered Vesicle Gels as Template for the Formation of Silica Gels*. Ooppel C., Prevost S., Noirez L. and Gradzielski M. **Langmuir**, vol. 27(14), pp. 8885-8897, (2011)
- 97 *Preferential solvation of lysozyme in water/ethanol mixtures*. Ortore M. G., Mariani P., Carsughi F., Cinelli S., Onori G., Teixeira J. and Spinozzi F. **Journal of Chemical Physics**, vol. 135(24), pp., (2011)
- 98 *Off-specular data representations in neutron reflectivity*. Ott F. and Kozhevnikov S. **Journal of Applied Crystallography**, vol. 44, pp. 359-369, (2011)
- 99 *Effects of nonmagnetic La impurities on the spin resonance of Ce(1-x)La(x)CoIn(5) single crystals as seen via inelastic neutron scattering*. Panarin J., Raymond S., Lapertot G., Flouquet J. and Mignot J. M. **Physical Review B**, vol. 84(5), pp., (2011)
- 100 *Polymeric Nanoparticles Stabilized by Surfactants Investigated by Light Scattering, Small-Angle Neutron Scattering, and Cryo-TEM Methods*. Panek J., Filippov S. K., Konak C., Nallet F., Noirez L., Karlsson G. and Stepanek P. **Journal of Dispersion Science and Technology**, vol. 32(6), pp. 888-897, (2011)
- 101 *Effects of charge inhomogeneities on elementary excitations in La(2-x)Sr(x)CuO(4)*. Park S. R., Hamann A., Pintschovius L., Lamago D., Khaliullin G., Fujita M., Yamada K., Gu G. D., Tranquada J. M. and Reznik D. **Physical Review B**, vol. 84(21), pp., (2011)
- 102 *Structural and magnetic properties of RMn(2-x)Fe(x)D(6) compounds (R=Y, Er; x <= 0.2) synthesized under high deuterium pressure*.

- Paul-Boncour V., Filipek S. M., Sato R., Wierzbicki R., Andre G., Porcher F., Reissner M. and Wiesinger G. **Journal of Solid State Chemistry**, vol. 184(2), pp. 463-469, (2011)
- 103 *Pluronic and beta-cyclodextrin in water: from swollen micelles to self-assembled crystalline platelets*. Perry C., Hebraud P., Gernigon V., Brochon C., Lapp A., Lindner P. and Schlatter G. **Soft Matter**, vol. 7(7), pp. 3502-3512, (2011)
- 104 *Substitution Effect on the Interplane Coupling in Crednerite: the Cu(1.04)Mn(0.96)O(2) Case*. Poienar M., Vecchini C., Andre G., Daoud-Aladine A., Margiolaki I., Maignan A., Lappas A., Chapon L., Hervieu M., Damay F. and Martin C. **Chemistry of Materials**, vol. 23(1), pp. 85-94, (2011)
- 105 *Magnetization distribution in the tetragonal Ba(Fe(1-x)Co(x))(2)As(2), x=0.066 probed by polarized neutron diffraction*. Prokes K., Gukasov A., Argyriou D. N., Bud'ko S. L., Canfield P. C., Kreyssig A. and Goldman A. I. **Epl**, vol. 93(3), pp., (2011)
- 106 *The Sm-like RNA chaperone Hfq mediates transcription antitermination at Rho-dependent terminators*. Rabhi M., Espeli O., Schwartz A., Cayrol B., Rahmouni A. R., Arluisson V. and Boudvillain M. **Embo Journal**, vol. 30(14), pp. 2805-2816, (2011)
- 107 *Highly Anisotropic Anomaly in the Dispersion of the Copper-Oxygen Bond-Bending Phonon in Superconducting YBa(2)Cu(3)O(7) from Inelastic Neutron Scattering*. Raichle M., Reznik D., Lamago D., Heid R., Li Y., Bakr M., Ullrich C., Hinkov V., Hradil K., Lin C. T. and Keimer B. **Physical Review Letters**, vol. 107(17), pp., (2011)
- 108 *The Cu and Te coordination environments in Cu-doped Ge-Te glasses*. Ratkai L., Goncalves A. P., Delaizir G., Godart C., Kaban I., Beuneu B. and Jovari P. **Solid State Communications**, vol. 151(21), pp. 1524-1527, (2011)
- 109 *Microscopic origin of demixing in Ge(20)Se(x)Te(80-x) alloys*. Ratkai L. R. L., Conseil C., Nazabal V., Bureau B., Kaban I., Bednarcik J., Beuneu B. and Jovari P. **Journal of Alloys and Compounds**, vol. 509(17), pp. 5190-5194, (2011)
- 110 *Solubility and Self-Assembly of Amphiphilic Gradient and Block Copolymers in Supercritical CO(2)*. Ribaut T., Oberdisse J., Annighofer B., Fournel B., Sarrade S., Haller H. and Lacroix-Desmazes P. **Journal of Physical Chemistry B**, vol. 115(5), pp. 836-843, (2011)
- 111 *Nanocomposite Materials with Controlled Anisotropic Reinforcement Triggered by Magnetic Self-Assembly*. Robbes A. S., Cousin F., Meneau F., Dalmas F., Boue F. and Jestin J. **Macromolecules**, vol. 44(22), pp. 8858-8865, (2011)
- 112 *Direct evidence for inelastic neutron "acceleration" by (177)Lu(m)*. Roig O., Meot V., Rosse B., Belier G., Daugas J. M., Letourneau A., Menelle A. and Morel P. **Physical Review C**, vol. 83(6), pp., (2011)
- 113 *Influence of Surfactants on Hydrophobically End-Capped Poly(ethylene oxide) Self-Assembled Aggregates Studied by SANS*. Rufier C., Collet A., Viguier M., Oberdisse J. and Mora S. **Macromolecules**, vol. 44(18), pp. 7451-7459, (2011)
- 114 *In situ molecular dynamics analysis of the water hydrogen bond at biomolecular sites: Hydrophobicity enhances dynamics heterogeneity*. Russo D., Pellegrini E., Gonzalez M. A., Perticaroli S. and Teixeira J. **Chemical Physics Letters**, vol. 517(1-3), pp. 80-85, (2011)
- 115 *Vibrational Density of States of Hydration Water at Biomolecular Sites: Hydrophobicity Promotes Low Density Amorphous Ice Behavior*. Russo D. R. D., Teixeira J., Kneller L., Copley J. R. D., Ollivier J., Perticaroli S., Pellegrini E. and Gonzalez M. A. **Journal of the American Chemical Society**, vol. 133(13), pp. 4882-4888, (2011)
- 116 *Interparticle distance in monolayers controlled by soft spacers*. Said-Mohamed C., Niskanen J., Karesoja M., Pulkkinen P., Tenhu H., Daoud M. and Lee L. T. **Soft Matter**, vol. 7(15), pp. 7112-7122, (2011)
- 117 *Doxorubicin Loaded Magnetic Polymersomes: Theranostic Nanocarriers for MR Imaging and Magneto-Chemotherapy*. Sanson C., Diou O., Thevenot J., Ibarboure E., Soum A., Brulet A., Miraux S., Thiaudiere E., Tan S., Brisson A., Dupuis V., Sandre O. and Lecommandoux S. **Acs Nano**, vol. 5(2), pp. 1122-1140, (2011)
- 118 *Two-dimensional electron gas with universal subbands at the surface of SrTiO(3)*. Santander-Syro A. F., Copie O., Kondo T., Fortuna F., Pailhes S., Weht R., Qiu X. G., Bertran F., Nicolaou A., Taleb-Ibrahimi A., Le Fevre P., Herranz G., Bibes M., Reyren N., Apertret Y., Lecoecur P., Barthelemy A. and Rozenberg M. J. **Nature**, vol. 469(7329), pp. 189-193, (2011)
- 119 *The spin ice Ho(2)Ti(2)O(7) versus the spin liquid Tb(2)Ti(2)O(7): field-induced magnetic structures*. Sazonov A. P., Gukasov A. and Mirebeau I. **Journal of Physics-Condensed Matter**, vol. 23(16), pp., (2011)
- 120 *Relation between crystallinity and chemical nature of surface on wettability: A study on pulsed laser deposited TiO(2) thin films*. Shirolkar M. M., Phase D., Sathe V., Rodriguez-Carvajal J., Choudhary R. J. and Kulkarni S. K. **Journal of Applied Physics**, vol. 109(12), pp., (2011)
- 121 *Absence of ferromagnetism in Mn-doped tetragonal zirconia*. Srivastava S. K., Lejay P., Barbara B., Boisron O., Pailhes S. and Bouzerar G. **Journal of Applied Physics**, vol. 110(4), pp., (2011)
- 122 *Non-magnetic impurity induced magnetism in rutile TiO(2):K compounds*. Srivastava S. K., Lejay P., Barbara B., Boisron O., Pailhes S. and Bouzerar G. **Journal of Physics-Condensed Matter**, vol. 23(44), pp., (2011)
- 123 *Investigation of Confined Ionic Liquid in Nanostructured Materials by a Combination of SANS, Contrast-Matching SANS, and Nitrogen Adsorption*. Stefanopoulos K. L., Romanos G. E., Vangeli O. C., Mergia K., Kanellopoulos N. K., Koutsioubas A. and Lairez D. **Langmuir**, vol. 27(13), pp. 7980-7985, (2011)
- 124 *Magnetic excitations in the metallic single-layer ruthenates Ca(2-x)Sr(x)RuO(4) studied by inelastic neutron scattering*. Steffens P., Friedt O., Sidis Y., Link P., Kulda J., Schmalzl K., Nakatsuji S. and Braden M. **Physical Review B**, vol. 83(5), pp., (2011)
- 125 *Anisotropic Critical Magnetic Fluctuations in the Ferromagnetic Superconductor UCoGe*. Stock C., Sokolov D. A., Bourges P., Tobash P. H., Gofryk K., Ronning F., Bauer E. D., Rule K. C. and Huxley A. D. **Physical Review Letters**, vol. 107(18), pp., (2011)
- 126 *Unprecedented Robust Antiferromagnetism in Fluorinated Hexagonal Perovskites*. Sturza M., Kabbour H., Daviero-Minaud S., Filimonov D., Pokholok K., Tiercelin N., Porcher F., Aldon L. and Mentre O.

- Journal of the American Chemical Society**, vol. 133(28), pp. 10901-10909, (2011)
- 127 *DNA-Polymer Micelles as Nanoparticles with Recognition Ability*. Talom R. M., Fuks G., Kaps L., Oberdisse J., Cerclier C., Gaillard C., Mingotaud C. and Gauffre F. **Chemistry-a European Journal**, vol. 17(48), pp. 13495-13501, (2011)
- 128 *Reinforcement and Polymer Mobility in Silica-Latex Nanocomposites with Controlled Aggregation*. Tatou M., Genix A. C., Imaz A., Forcada J., Banc A., Schweins R., Grillo I. and Oberdisse J. **Macromolecules**, vol. 44(22), pp. 9029-9039, (2011)
- 129 *Probing magnetic domain wall profiles by neutron spin precession*. Thibaudeau P., Ott F., Thiaville A., Dubuget V. and Duverger F. **Epl**, vol. 93(3), pp., (2011)
- 130 *Mixed Acoustic Phonons and Phase Modes in an Aperiodic Composite Crystal*. Toudic B., Lefort R., Ecolivet C., Guerin L., Currat R., Bourges P. and Brezczewski T. **Physical Review Letters**, vol. 107(20), pp., (2011)
- 131 *Temperature-pressure phase diagram of an aperiodic host guest compound*. Toudic B., Rabiller P., Bourgeois L., Huard M., Ecolivet C., McIntyre G. J., Bourges P., Brezczewski T. and Janssen T. **Epl**, vol. 93(1), pp., (2011)
- 132 *Spin-wave excitations in the ferromagnetic metallic and in the charge-, orbital-, and spin-ordered states in $Nd(1-x)Sr(x)MnO(3)$ with x approximate to 0.5*. Ulbrich H., Kruger F., Nugroho A. A., Lamago D., Sidis Y. and Braden M. **Physical Review B**, vol. 84(9), pp., (2011)
- 133 *Evidence for Charge Orbital and Spin Stripe Order in an Overdoped Manganite*. Ulbrich H. U. H., Senff D., Steffens P., Schumann O. J., Sidis Y., Reutler P., Revcolevschi A. and Braden M. **Physical Review Letters**, vol. 106(15), pp., (2011)
- 134 *A SANS investigation of micelles in mixtures of cetyltrimethylammonium bromide (CTAB)/octyl-beta-D-glucopyranoside (C(8)G(1)) in water/glycerol solvent*. Valiente M., Cortes A. B., Gradzielski M., Noirez L. and Schweins R. **Colloids and Surfaces a-Physicochemical and Engineering Aspects**, vol. 375(1-3), pp. 117-123, (2011)
- 135 *On the origin of the stability of foams made from cationic surfactant mixtures*. Varade D., Carriere D., Arriaga L. R., Fameau A. L., Rio E., Langevin D. and Drenckhan W. **Soft Matter**, vol. 7(14), pp. 6557-6570, (2011)
- 136 *On the role of lattice dynamics on low-temperature oxygen mobility in solid oxides: a neutron diffraction and first-principles investigation of $La(2)CuO(4+\delta)$* . Villesuzanne A., Paulus W., Cousson A., Hosoya S., Le Dreau L., Hernandez O., Prestipino C., Houchati M. I. and Schefer J. **Journal of Solid State Electrochemistry**, vol. 15(2), pp. 357-366, (2011)
- 137 *Tracing nucleation pathways in protein aggregation by using small angle scattering methods*. Vogt K., Javid N., Alvarez E., Sefcik J. and Bellissent-Funel M. C. **Soft Matter**, vol. 7(8), pp. 3906-3914, (2011)
- 138 *The DFPase from *Loligo vulgaris* in sugar surfactant-based bicontinuous microemulsions: structure, dynamics, and enzyme activity*. Wellert S., Tiersch B., Koetz J., Richardt A., Lapp A., Holderer O., Gab J., Blum M. M., Schulreich C., Stehle R. and Hellweg T. **European Biophysics Journal with Biophysics Letters**, vol. 40(6), pp. 761-774, (2011)
- 139 *Structure, Properties, and Theoretical Electronic Structure of $UCuOP$ and $NpCuOP$* . Wells D. M., Ringe E., Kaczorowski D., Gnida D., Andre G., Haire R. G., Ellis D. E. and Ibers J. A. **Inorganic Chemistry**, vol. 50(2), pp. 576-589, (2011)
- 140 *Influence of deuteration on lithium acetate dihydrate studied by inelastic X-ray scattering, density functional theory, thermal expansion, elastic and thermodynamic measurements*. Winkler B., Haussuhl E., Bauer J. D., Schroder F., Refson K., Milman V., Hennion B., Bossak A. and Krisch M. **Dalton Transactions**, vol. 40(8), pp. 1737-1742, (2011)
- 141 *Self-ordered arrays of linear defects and virtual singularities in thin smectic-A films*. Zappone B., Lacaze E., Hayeb H., Goldmann M., Boudet N., Barois P. and Alba M. **Soft Matter**, vol. 7(3), pp. 1161-1167, (2011)
- 142 *Dipolar interactions in arrays of ferromagnetic nanowires: A micro-magnetic study*. Zighem F., Maurer T., Ott F. and Chaboussant G. **Journal of Applied Physics**, vol. 109(1), pp., (2011)
- 143 *Role of Antisymmetric Exchange in Selecting Magnetic Chirality in $Ba(3)NbFe(3)Si(2)O(14)$* . Zorko A., Pregelj M., Potocnik A., van Tol J., Ozarowski A., Simonet V., Lejay P., Petit S. and Ballou R. **Physical Review Letters**, vol. 107(25), pp., (2011)

Teaching & Education

LLB (neutron source) and SOLEIL (synchrotron) COMMON PHD PROGRAM :

New program starting in 2012

SOLEIL and LLB are two large scale structures at the service of scientific communities both located on the Saclay plateau. They offer a range of instruments at the highest international standard for conducting experiments using synchrotron radiation and neutron scattering.



To meet jointly to their national missions and strengthen collaboration between the two facilities and all the French academic and industrial laboratories, the directions of the two infrastructures decided to launch each year a call for proposals.

Co-funding of PHD theses are proposed for particularly innovative subjects using complementarities of synchrotron and neutron techniques.

The objective is to stimulate original subjects using the synchrotron-neutron complementary and the original and complementary expertise at any level whatsoever (synthesis, simulation and theory, NMR ...) of the selected laboratory.

These theses will involve a co-direction with a scientific leader of one of two facilities (SOLEIL or LLB), a correspondent of the other facility and a scientific responsible of the partner laboratory. For the realization, as part of the thesis, of experiments on SOLEIL or LLB, the corresponding time requests will be supported by the direction of the LLB and will form part

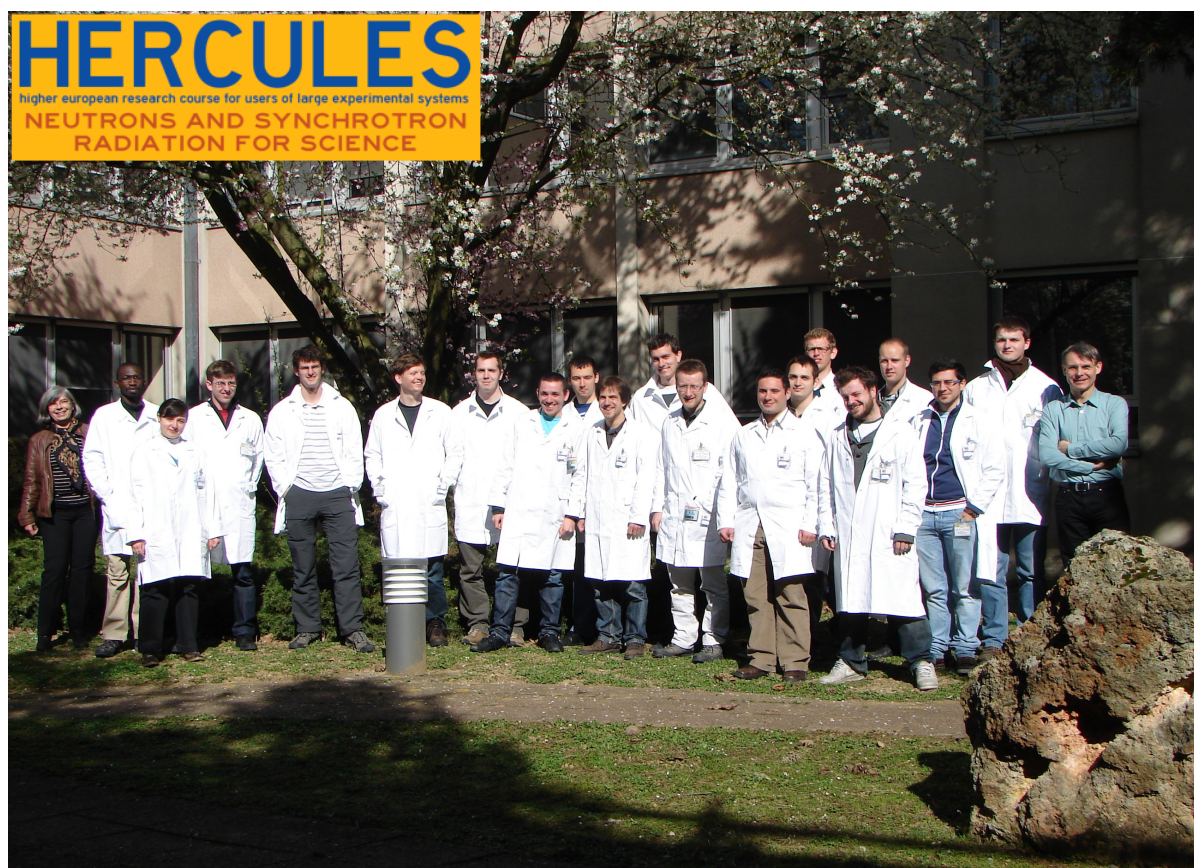


The subject should be multidisciplinary and all fields of science are concerned. The proposed theme is about: surfaces, interfaces, functionalizations, with keywords such as: biomimetics, micro-nano fluidics, magnetics, materials for energy ...

These keywords are indicative and any multidisciplinary subject will be considered.

Prior experience in the use of very large facilities is not a prerequisite for the teams, training can be provided by the centers.

TRAINING AND EDUCATION...



HERCULES COURSES (21-25 MARCH 2011)

Hercules, the European graduate school for the large scale facilities users, gathers annually about 75 participants over several weeks for lectures tutorials, and practical sessions on the applications of X-Rays and neutron scattering. The last ten days of this 4-weeks formation takes place in the Paris area, at the SOLEIL synchrotron or at the LLB for those participants interested in a reinforced experimental neutron programme. At the LLB they had the opportunity to exercise on real spectrometers after a general presentation of the installation and a visit of the reactor hall.

<http://hercules.grenoble.cnrs.fr>

HABILITATIONS TO SUPERVIZE PhD STUDENTS (HdR)

: Neutrons et dynamique de spin

Sylvain Petit (04/03/2011)

“Topologies magnétiques triangulaires et propriétés physiques « exotiques”

Françoise Damay-Rowe (02/05/2011)

“Confinement nanométrique de fluides moléculaires : des interactions de surface aux propriétés de transport à une dimension“

Jean-Marc Zanotti (25/11/2011)

FAN DU LLB (5-8 DECEMBER 2011)

FAN du LLB is an annual school delivered in French and offering young French-speaking researchers a first contact with real experimental neutron scattering. The school is aimed at students and post-docs working in all scientific areas where neutrons can provide valuable insights, although priority is given to those having never had any contact with neutrons scattering. After an introduction to neutron sources and neutron scattering, ten different thematic subjects based on different scientific problems that can be addressed by neutron scattering, are proposed to the students. In groups of four to five, the students are then introduced to two different neutrons scattering technique, during three days devoted to experiments and data analysis. One of the distinguishing features of our school is that the students often come with their own samples, which are tested during the training together with our demonstration samples. This ensures a good and efficient participation of the students. In 2011, the number of participants was 31.

Website: <http://www-llb.cea.fr/fan>



JDN 19 (6-10 JUNE, 2011)



Every year, the French Neutron Society (SFN), with the help of LLB and ILL centers and Grenoble UJF University, organizes the "Journées de la Neutronique", that gathers the national neutrons community. Exceptionnally, there were no thematic school in the 19th edition, but the duration of Rosat-Mignod meeting was lengthened in order to present the state of the art and the new scientific and technological perspectives of Neutron scattering.



NEW PHD STUDENTS IN 2011



GENEVAZ Nicolas – BDI-2011-2014

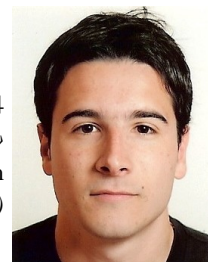
« *Nanocomposites polymères-particules greffées : contribution de la dynamique des chaînes greffées et libres sur les mécanismes de dispersion et les propriétés mécaniques* »

Direction de thèse : D. Bertin & J. Jestin
(Matière Molle).

RIDIER Karl – BDI-2011-2014

« *Excitations magnétiques dans les composés photomagnétiques à transition de spins* »

Direction de thèse : G. Chaboussant & B. Gillon
(Matériaux et Interfaces & Diffraction sur monocristaux)



THESES DEFENDED IN 2011



TASSERIT Christophe – 15 March 2011

« *Transport d'ions et d'objets dans les nanopores* »

Direction de thèse : D. Lairez et M-C. Clochard
(Biologie et Systèmes désordonnés)

FAMEAU Anne-Laure – 20 Avril 2011

« *Assemblages d'acides gras : du volume aux interfaces* »

Direction de thèse : F. Boué, J-P. Douliez, F. Cousin
(Matière Molle)



BHOWMIK Debsindhu - 30 Septembre 2011

« *Etude de la dynamique d'ions hydrophobes en solutions aqueuses par diffusion de neutrons et par simulation numérique* »

Direction de thèse : P. Turq, N. Malikova
(Biologie et Systèmes désordonnés)

ROBBES Anne Sophie - 14 Octobre 2011

« *Nanocomposites à base de particules magnétiques : synthèse et contribution de la dispersion des charges et de la conformation des chaînes sur les propriétés de renforcement* »

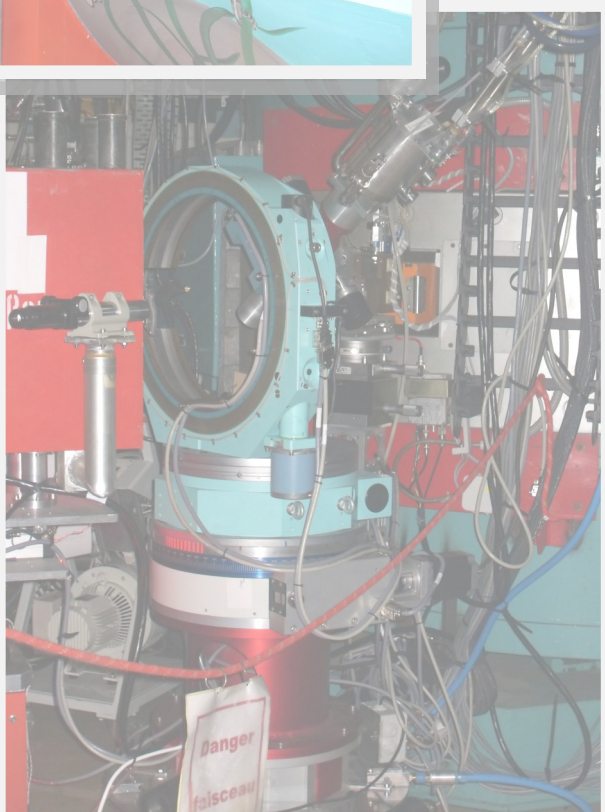
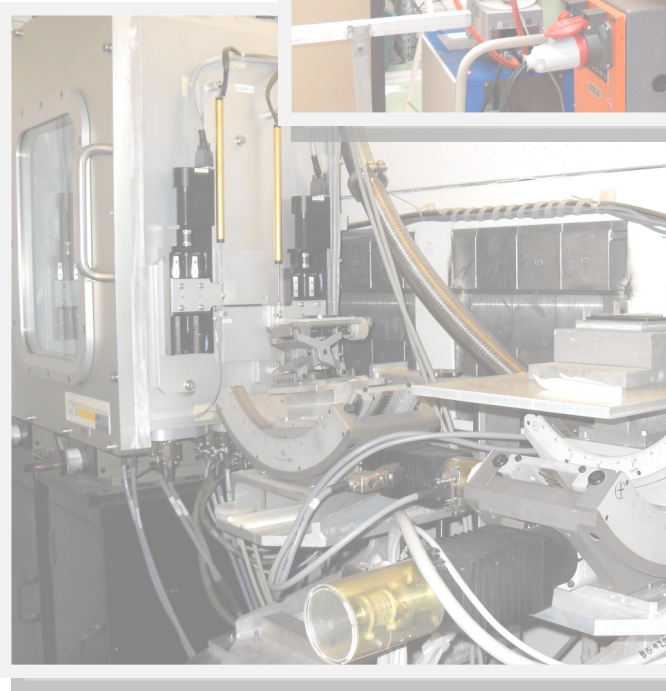
Direction de thèse : F. Boué, J. Jestin, F. Cousin
(Matière Molle)



SAID MOHAMED Cynthia – 14 Novembre 2011

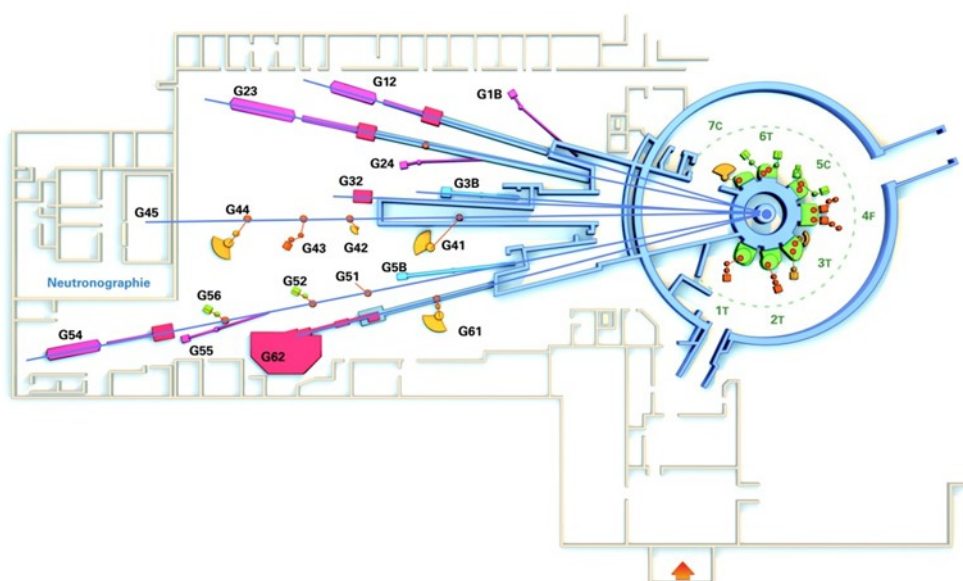
« *Propriétés optiques des nanoparticules d'or greffées de polymères thermosensibles* »

Direction de thèse : L. Lee
(Matériaux et interfaces)



Beamtime Access

GENERAL LAYOUT OF THE SPECTROMETERS



SPECTROMETERS OPEN TO USERS		CONTACTS
Powder diffractometers		
3T2	Florence Porcher	florence.porcher@cea.fr
G4.1	Gilles André	gilles.andre@cea.fr
G6.1	Isabelle Mirebeau	isabelle.mirebeau@cea.fr
Single crystal diffractometers		
5C1	Béatrice Gillon	beatrice.gillon@cea.fr
5C1	Alain Cousson	alain-f.cousson@cea.fr
6T2	Arsen Goukassov	arsen.goukassov@cea.fr
Diffuse scattering instrument		
7C2	Brigitte Beuneu	brigitte.beuneu@cea.fr
Small-angle scattering instruments		
G1.2	Didier Lairez	didier.lairez@cea.fr
G2.3	Alain Lapp	alain.lapp@cea.fr
G5.4	José Teixeira	jose.teixeira@cea.fr
G5bis	Sylvain Désert	sylvain.desert@cea.fr
Diffractometers for material science studies		
6T1	Marie-Hélène Mathon	marie-helene.mathon@cea.fr
G5.2	Vincent Klosek	vincent.klosek@cea.fr
Reflectometers		
G3bis	Fabrice Cousin	fabrice.cousin@cea.fr
G2.4	Frédéric Ott	frederic.ott@cea.fr
Triple-axis instruments		
1T	Daniel Lamago / Yvan Sidis (CRG Instrument Karlsruhe/LLB)	daniel.lamago@cea.fr / yvan.sidis@cea.fr
2T	Philippe Bourges	philippe.bourges@cea.fr
4F1	Sylvain Petit	sylvain.petit@cea.fr
4F2	Daniel Petitgrand	daniel.petitgrand@cea.fr
Quasi-elastic instruments		
G6.2	Jean-Marc Zanotti	jean-marc.zanotti@cea.fr
G1bis	Stéphane Longeville	stephane.longeville@cea.fr
Neutron radiography		
G4.5	Guy Bayon	guy.bayon@cea.fr

The LLB-Orphée neutron scattering and imaging instruments

Powder diffractometers

- 3T2** "Thermal neutrons" 2-axis (50 detectors) high resolution, mainly for nuclear structure determination.
- G4.1** "Cold neutrons" 2-axis (multidetector 800 cells) high flux, mainly for magnetic structure determination
- G6.1** "Cold neutrons" 2-axis (multidetector 400 cells) with long wavelength ($\sim 5\text{\AA}$) and high flux, for the study of very small powder samples ($< 1\text{mm}^3$). Very high pressure cell available (40 GPa).

Single crystal diffractometers

- 5C1** "Hot neutrons" 2-axis with lifting arm, polarized neutrons, magnetic field (8 Tesla) for spin-density maps determination
- 5C2** "Hot neutrons" 4-circle for nuclear structure determination.
- 6T2** "Thermal neutrons" 2-axis, lifting arm and 4-circle, mainly for magnetic structure determination. 12 Tesla magnetic field available, 2D detector.

Diffuse scattering instruments

- 7C2** "Hot neutrons" 2-axis (multidetector 640 cells) for local order studies in liquid or amorphous systems. Cryostat and furnace available (1.2K to 1300°C).

Small-angle scattering instruments

- G1.2** "Cold neutrons" (annular detector, 30 rings) for study of large scale structures in isotropic systems (mainly polymers and colloids).
- G2.3** "Cold neutrons" (X-Y detector, 128x128 cells) for study of large scale structures (10 to 500 Å) in anisotropic systems (polymers under stress, metallurgical samples, vortex in superconductors).
- G5.4** "Cold neutrons" (X-Y detector, 64x64 cells) for multipurpose studies of large scale structures.
- G5bis** Very Small Angle Neutrons Scattering spectrometer

Diffractometers for material science studies

- 6T1** "Thermal neutrons" 4-circle for texture determination.
- G5.2** "Cold neutrons" 2-axis for internal strain determination in bulk samples with spatial resolution $\sim 1\text{mm}^3$.

Reflectometers

- G3bis** "Cold neutrons" reflectometer operating in time-of-flight mode for multipurpose surface studies.
- G 2.4** "Cold neutrons" reflectometer with polarized neutrons and polarization analysis for the study of magnetic layers.

Triple-axis instruments

- 1T** "Thermal neutrons" high-flux 3-axis instrument with focussing monochromator and analyser, mainly devoted to phonon dispersion curves measurements. Very high pressure cell (100 Kbar) available.
CRG Instrument operated in collaboration between the INFP Karlsruhe and the L.L.B
- 2T** "Thermal neutrons" high-flux spectrometer with focussing monochromator and analyser, mainly devoted to spin-waves and magnetic excitations studies (1.5 to 80 meV).
- 4F1** "Cold neutrons" high flux 3-axis instruments with double monochromator and analyzer, mainly devoted to the study of low-energy
- 4F2** ($15\mu\text{eV}$ to 4meV) magnetic excitations. Polarized neutrons and polarization analysis option available.

Quasi-elastic instruments

- G62** "Cold neutrons" high resolution ($\sim 15\mu\text{eV}$ at 10\AA) time-of-flight instrument for the study of low energy excitations, mainly in disordered systems.
- G1bis** "Cold neutrons", high resolution and high flux spin-echo instrument. It can study, in a large Q range, slow dynamics of large molecules in biology or long relaxation times like in glassy transition (Fourier times $\sim 20\text{ns}$)

Neutron Radiography

- G4.5** Imaging technique : white beam facility for non-destructive control or dynamics imaging.

AUXILLIARY SERVICES AVAILABLE

Laboratories for sample preparation:

- Chemistry laboratory
- Biological laboratory

Technical help for:

- Vacuum/Cryogenics
- Cryostat, Furnace (0.1 – 2000 K)
- High pressures (up to 10 GPa)
- High magnetic fields (up to 10 T)
- Mechanics



LLB has been selected in the frame of the European Community – Access activities of the Neutron scattering and Muon spectroscopy Integrated Infrastructure Initiative (NMI3) which supports access to neutron



beams for the selected user teams, travel and subsistence fees of visiting scientists. The program is opened to E.C. users and to scientists of the associated states.

<http://idb.neutron-eu.net/facilities.php>

Beamtime access is free of charge for any experimentalist from the French Scientific community. LLB takes in charge the expenses (travel and stay) of 2 people during the experiment.

Beamtime on the 23 open-access spectrometers can be requested by submission of:

- **An experimental application to a Selection Committee (Normal Procedure)**
This procedure is open to any public/industrial researcher that is interested in using neutron scattering for his research. Results should be free to be totally or partially published in a Scientific Review.
DEADLINE FOR APPLICATION: May 1st and November 1st
<http://www-llb.cea.fr/en/fr-en/proposal.php>
- **An experimental application to the Directors (Exceptional)**
This special procedure should only be used exceptionally for hot topics, confidentiality reasons or if an anomaly in the review procedure is suspected. The delay between the acceptation decision and the realization of the experiment is shortened to the minimum.
No deadline applies for such propositions (Application all along the year).
<http://www-llb.cea.fr/en/fr-en/proposal.php>
- **A fast access application**
This procedure allows a rapid access (1 to 2 months delay) to the spectrometers in order to perform a short experiment (1 day max.). It can be used for feasibility tests, sample characterization, obtaining complementary results...
No deadline applies for such propositions (Application all along the year).
<http://www-llb.cea.fr/en/fr-en/prop-rap.php>

CONTACT AT LABORATOIRE LEON BRILLOUIN

Laboratoire Léon Brillouin

Scientific Office

CEA SACLAY

Bâtiment 563

F - 91191 Gif-sur-Yvette Cedex

Tel. : 33(0) 1 69 08 60 38 •

Fax : 33 (0) 1 69 08 82 61

e-mail : [experience-llb at cea.fr](mailto:experience-llb@cea.fr)

Internet : <http://www-llb.cea.fr>

Selection committees

Proposals are examined by 5 Selection Committees. Each is composed of 10 to 12 senior scientists that are nominated by the management of LLB for 3 years. At least half of them do not belong to the LLB and 2 or 3 are coming from foreign institutes.

For each spectrometer, LLB gives a beam-time available which is shared out by the committee; each proposal gets a grade A or B or C.

A : The experiment must be done and the committee allocates a beam-time

B : The experiment might be done if there is some extra beam-time,

C : The experiment is refused on scientific arguments.

Selection Committees are asked to take care of the educational duty of the LLB when proposal comes from new young searcher.

SELECTION COMMITTEES: SCIENTIFIC FOCUS AND SUB-FOCUS

Theme I Chemical physics, biological systems

- I.01 Polymers and Supramolecular Structures
- I.02 Water, aqueous solutions, polyelectrolytes, surfactants
- I.03 System of biological interest, Biophysics
- I.04 Colloids, nanostructures
- I.05 Gels, composite materials
- I.06 Other...

Theme II Crystallographic and magnetic structures

- II.01 Crystalline structures
- II.02 Phases transitions
- II.03 Magnetic Structures
- II.04 High pressures (on powders)
- II.05 Other...

Theme III Magnetism: Single-crystal systems and thin layers

- III.01 Magnetic thin layers
- III.02 Spin density
- III.03 Systems with strong quantum correlations
- III.04 Extreme conditions (strong fields, high pressures)
- III.05 Magnetic nanosystems
- III.06 Other...

Theme IV Disordered Systems, nanostructured materials and materials

- IV.01 Liquid and amorphous structures
- IV.02 Dynamics of disordered systems
- IV.03 Thin film materials
- IV.04 Nanostructured materials, precipitation, cavities,...
- IV.05 Crystallographic textures
- IV.06 Strains and residual stresses
- IV.07 Other...

Theme V Excitations

- V.01 Magnons
- V.02 Superconductivity
- V.03 Coupling spin-network
- V.04 Dynamics in frustrated systems
- V.05 Polarized neutrons with polarization analysis
- V.06 Phonons
- V.07 Other...

LLB 2011 Reviewing committees

LLB members	French users	European users
-------------	--------------	----------------

COLLEGE 1: Chemical physics, biological systems

Organisers: J. Jestin, G. Fadda

F. Cousin	C. Chassenieux [‡]	Université du Mans	F. Gabel [‡]	IBS, Grenoble
D. Lairez	S. Lyonnard	CEA, Grenoble	W. Hauessler [‡]	FRMII, TU München
	F. Nallet	CRPP, Bordeaux	R. V. Klitzing	TU, Berlin
	R Schweins	ILL, Grenoble	M. Sferrazza [pdt]	Université de Bruxelles
	Y. Tran	ESPCI, Paris		

COLLEGE 2: Crystallographic and magnetic structures

Organisers: F. Porcher, N. Rey

F. Damay	M. Josse	Université Bordeaux 1	J. A. Blanco	Université Oviedo, ES
	S. Ravy	Soleil, St Aubin	A. Daoud-Aladine	ISIS, UK
	P. Roussel	UCC, Villeneuve d'Ascq	G. Heger [‡] [pdt]	Université Aachen, D

COLLEGE 3: Magnetism: Single-crystal systems and thin layers

Organisers: A. Bataille, F. Ott

G André	T. Hauet	Université Nancy I	J. Campo [pdt]	Université Zaragoza, ES
	O. Mentré [‡]	Chimie du Solide, Lille	K. Temst	Université Louvin , B
	E. Ressouche	ILL, Grenoble		

COLLEGE 4: Disordered Systems, nanostructured materials and materials

Organisers: V. Klosek, M.H. Mathon

F. Audonnet	J.L. Bechade [‡]		M. Fitzpatrick	Milton Keynes, UK
	J. Henry*	CEA, Saclay [Pdt]		
	L. Cormier	Universités Paris 6 et 7	M. Gonzalez	ILL, Grenoble
	A. Deschamps [‡]	SIMaP Grenoble		

COLLEGE 5: Excitations

Organisers: D. Petitgrand, J. Robert

D. Lamago	M. Boehm [pdt]	ILL, Grenoble	J. Hlinka	ASCR, Prague
	P. Foury	LPS, Orsay	A. Huxley	Université Edinburg, UK
	L.-P. Regnault	CEA, Grenoble	B. Roessli	PSI, Villingen, CH

[‡] Only for spring session - * Only for autumn session



Laboratoire Léon Brillouin

CEA Saclay

Bâtiment 563

F-91191 Gif-sur-Yvette Cedex

+33 (0) 1 69 08 52 41

+33 (0) 1 69 08 82 61

<http://www-llb.cea.fr>